University of Alberta

Library Release Form

Name of Author: Hossain Ahmed

Title of Thesis: *In Situ* Light Jet Energy Calibration Using Semileptonic Top Quark Decay with the ATLAS Experiment

Degree: Doctor of Philosophy

Year this Degree Granted: 2009

Hossain Ahmed

Date: _____

University of Alberta

In Situ Light Jet Energy Calibration Using Semileptonic Top Quark Decay with the ATLAS Experiment

by

Hossain Ahmed

A thesis submitted to the Faculty of Graduate Studies and Research in partial fulfillment of the requirements for the degree of **Doctor of Philosophy**.

Department of Physics

Edmonton, Alberta
Spring 2009

University of Alberta

Faculty of Graduate Studies and Research

The undersigned certify that they have read, and recommend to the Faculty of Graduate Studies and Research for acceptance, a thesis entitled *In Situ* **Light Jet Energy Calibration Using Semileptonic Top Quark Decay with the ATLAS Experiment** submitted by Hossain Ahmed in partial fulfillment of the requirements for the degree of **Doctor of Philosophy**.

Dr. Douglas M. Gingrich (Supervisor)

Dr. Zisis Papandreou (External)

Dr. Roger W. Moore

Dr. Chow Kim

Dr. Moritz Heimpel

Dr. Rafiei Davood

Date: _____

To my family,
for always being with me.

Abstract

Many particle physics measurements depend on the accurate knowledge of the energies of jets resulting from the fragmentation of quarks and gluons in the hard scattering process. A precise knowledge of the absolute jet energy scale is therefore an important issue at the Large Hadron Collider. The more accurately the energy of the jet is known, the more precisely fundamental parameters of the Standard Model can be measured. Top quarks dominantly decay into W bosons and b-quark jets, and the W bosons often decay into jets. The *in situ* calibration on resonance decay ($W \rightarrow jj$) method is used to determine the light jet energy scale in the ATLAS experiment. The performance of different jet algorithms are also investigated and reported in this thesis.

Acknowledgements

I am very much delighted to express my gratitude and thank all people who have helped and inspired me during my doctoral study at the University of Alberta, Edmonton, CANADA.

I firstly want to thank my supervisor Prof. Douglas M. Gingrich, Director of Centre for Particle Physics (CPP), Department of Physics, University of Alberta. I liked his supervision, inspiration and great efforts to explain things clear and simple. I learned many positive things for last four years in touch with him, which I sure, will impact on my future life, e.g. the time frame, work individually and/or with collaboration and tidy up things in proper manner. He is always accessible (on/off line) and willing to discuss. I am very grateful to Prof. Roger Moore and Prof. James L. Pinfold for their valuable courses on particle physics.

I would like to thank Dr. Jiansel Lu, research associate of ATLAS experiment at the centre for particle physics for many discussions on ATLAS physics analysis, software, presenting results and personal lives. He always encourages me to do things in time and safe.

I am very grateful to Dr. Bryan Caron, research scientist at the centre for particle physics for many helps, discussions and guidance.

I am indebted to all centre for particle physics (CPP) at the University of Alberta members for their support, discussions and for providing a fun environment in working together. Special thanks to Dr. Kim Minsuk, Dr. Soni Nitesh and Dr. Seema Bahinipati for coffee breaks and lot of discussions. Since the ATLAS experiment is an international collaborative experiment credits

and thanks are also owed to the many peoples in this collaboration.

I wish to thank my entire family especially my parents (who raised me, supported me, taught me and loved me) and in-law parents, my brothers and in-law brothers, my sisters and in-law sisters for their love and believe on me even though I live very far from them.

I love my two little daughters more than anything in the world. They are Ispeeta Ahmed (4 years old) and Wafeeqa Ahmed (5 months old). They are the biggest part of my life, even though they measured by inches and weighted by ounces. Their lovely and cute faces are my inspiration for doing good.

Finally and most importantly, I would like to express my gratitude, thank and love to my best friend and wife Nafisa Tasneem, who is also a Ph.D. student in Electrical and Computer Engineering department at the University of Alberta, CANADA. She was always supported my works, scientific trips and times.

Contents

List of Tables

List of Figures

List of Symbols

Acronyms

ALICE	A Large Ion Collider Experiment
AOD	Analysis Object Data
ATLAS	A Toroidal LHC ApparatuS
BMU	Barrel Muon Detector
CERN	European Laboratory for Particle Physics
CDF	Collider Detector at Fermilab
CMU	Central Muon Detector
CMS	Compact Muon Solenoid
CSC	Cathode Strip Chambers
CPP	Centre for Particle Physics, University of Alberta
DC	Data Challenge
D0	D Zero Experiment at Fermilab
EF	Event Filter
EM	Electromagnetic
FCAL	Forward Calorimeter
HEC	Hadronic Endcap Calorimeter
IP	Interaction Point
LAr	Liquid Argon
LCG	LHC Computing Grid
LHC	Large Hadron Collider
LO	Leading Order
MDT	Muon Drift Tube
NLO	Next Leading Order
NNLO	Next to Next Leading Order

Acronyms

PDF	Parton Distribution Function
PS	Proton Synchrotron
SPS	Super Proton Synchrotron
QCD	Quantum Chromodynamics
QED	Quantum Electrodynamics
RMS	Root Mean Square
ROD	Read-Out Driver
ROI	Region Of Interest
RPC	Resistive Plate Chamber
SC	Super Conducting
SCT	Silicon Central Tracker
SUSY	Supersymmetry
TAG	Event tags, short event summaries for event selection
TGC	Thin Gap Chamber
TRT	Transition Radiation Tracker

Symbols

A	Amperes (unit of current)
Hz	Unit of frequency (cycles per second)
J	Joules
K	Kelvin
L	integrated Luminosity
LVL	Level
M	Invariant Mass
MB	MegaBytes
GB	GigaBytes
T	Tesla
Y	rapidity
barn	Unit of cross section equivalent to 10^{-24}cm^{-2}
eV	electron Volt
η	pseudo-rapidity
ϕ	azimuthal or acoplanarity angle
σ	cross section (or resolution)
$\sqrt{s}$	center of mass collision energy

Chapter 1

Introduction

Particle physics is the basic of basic sciences. Started on 10/09/08 (September 10, 2008), the Large Hadron Collider (LHC) initiated its journey to unveil the basic unsolved and unanswered questions in nature (see section 2.1.1). The LHC and its experiments are designed to operate for over 10 years. With the tremendous efforts of several thousand physicists around the globe, it is installed in the LEP (Large Electron-Positron Collider) tunnel at CERN[1], which is 100 m underground between the French and Switzerland border as shown in figure 1.1. The LHC is operational and is currently in the process of being prepared for the collision of two counter-rotating proton beams head-on with 14 TeV centre of mass energy. The first beams were circulated through the collider on September 10, 2008, and the first high-energy collisions are expected to take place in autumn 2009.

A Toroidal LHC ApparatuS (ATLAS), one of two general purpose detectors, is designed to exploit the physics potential of the LHC. More than 2,000 physicists from 160 institutes in 37 countries work on the ATLAS experiment. It will investigate a wide range of new physics and make precision measurements of the known Standard Model (SM) parameters. The first (clock-wise direction) and the second (counter clock-wise direction) beams were observed in the ATLAS detector, which are shown in figures 1.2 and 1.3, respectively. Once colliding beams have been established, there will be a period of measure-

[1]CERN is the European Organization for Nuclear Research.

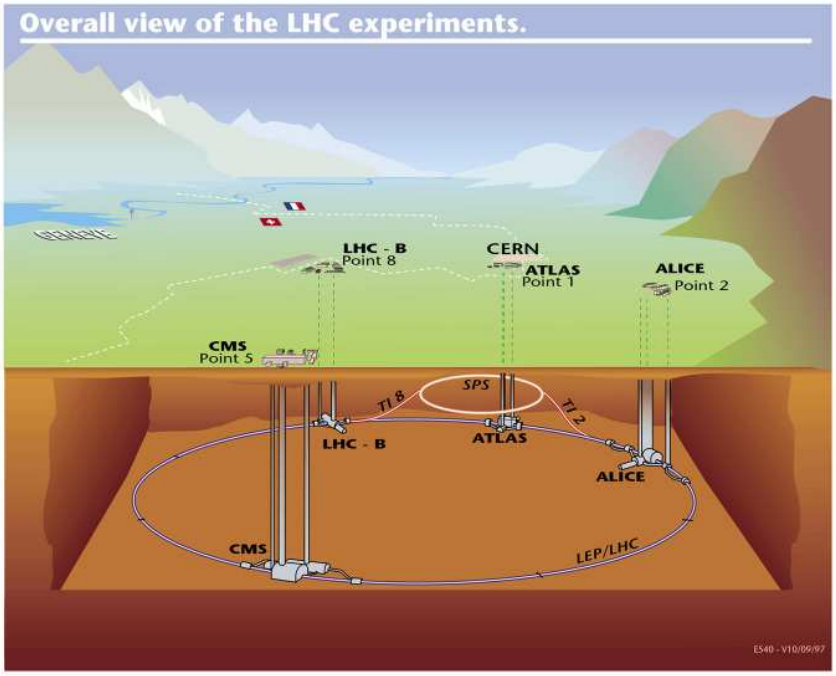

Figure 1.1: LHC main ring and four main experiments in its 27 km circumference [1].

ments and calibration for the ATLAS experiment.

Due to the huge centre of mass energy and high luminosity, the ATLAS detector will process an enormous amount of data that contains interesting and uninteresting events. Most of the interesting events will contain "jets"[2] in the final states. Therefore, a precise measurement of jet energies are very important for reconstructing the full event with high precision. Jets coming from well known resonances are also important to calibrate the detector. The LHC will be a top factory since at least one top-antitop event will be produced per second with 10^{33} cm^{-2}s^{-1} luminosity. According to the SM, the top quark will decay before forming any hadrons. At the early stage of the LHC, it is very important to commission and calibrate the detector *in situ* with real data. Top quark production is an ideal process for initial studies. In addition to an abundant production rate, the lepton plus jets channel (where at least one W

[2]Jets are defined in section 2.4.

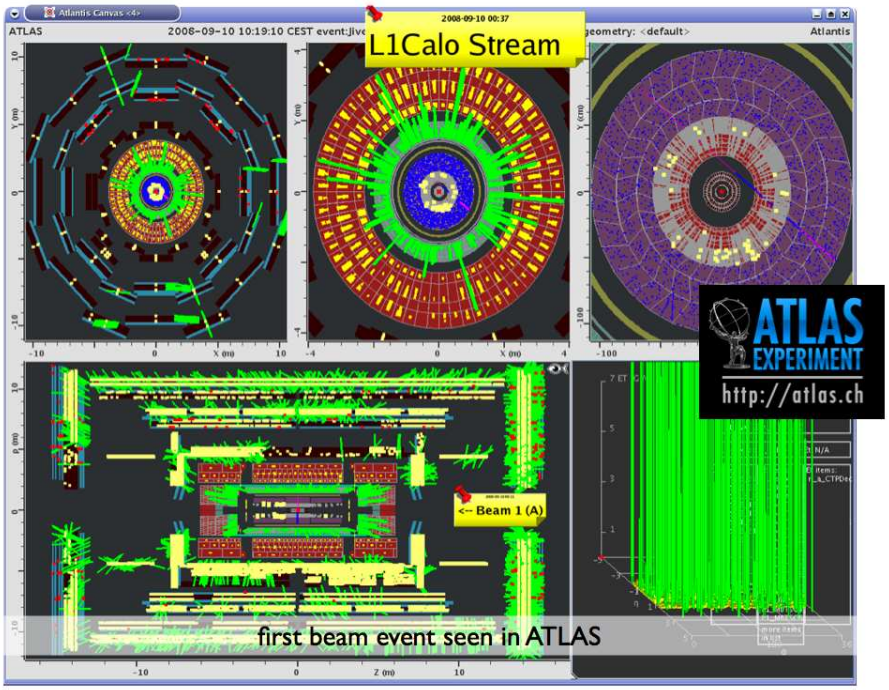

Figure 1.2: First beam event in the ATLAS detector.

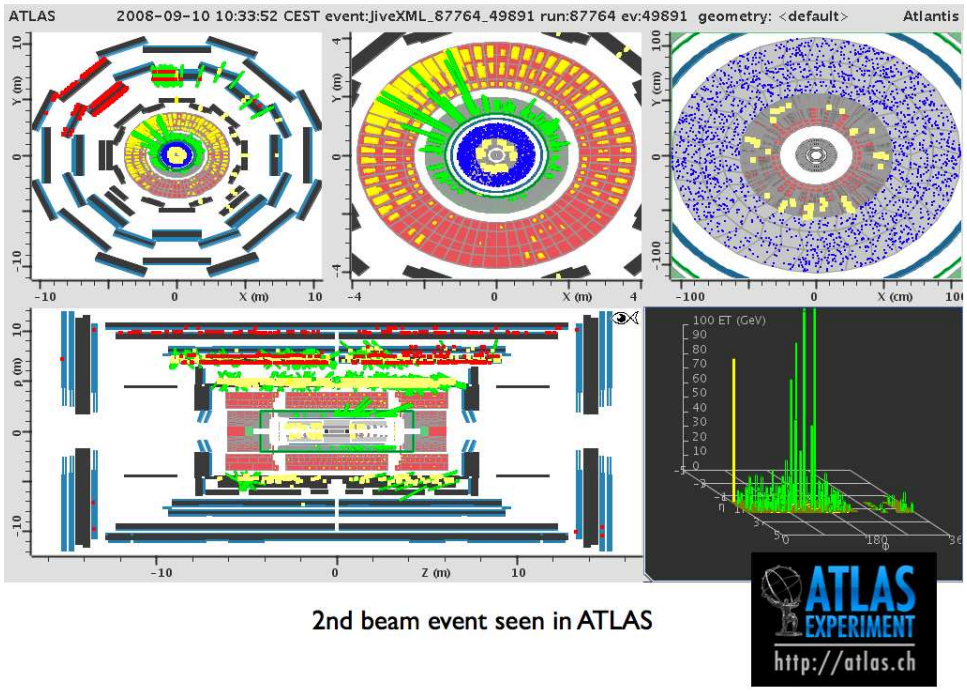

Figure 1.3: Second beam event in the ATLAS detector.

decays to a lepton) is easy to trigger on, and high purity samples of top quark events can be extracted with simple selection criteria. The initial accuracy of the jet energy is expected to be of the order of 10% [2]. The precision measurement of the top quark mass requires calibrating the jet energies to 1% or better. A light jet systematic bias in the light jet absolute energy scale induces a shift in the observed W invariant mass peak. This allows a determination of the correction factors E_{parton}/E_{jet} (where E_{parton} is the true quark energy and E_{jet} is the reconstructed jet energy corresponding to the quark energy) needed to properly calibrate the light jet scale, which has been done in this thesis.

All the analysis and results produced in this thesis are my own work but credits are also owed to the many people in the ATLAS collaboration e.g. the datasets I used are the ATLAS Monte Carlo data. I have written all the analysis code to produce results for the light jet energy scale from semileptonic top quark decay in $t\bar{t}$ events. Once again, credit goes to the collaboration since I used the analysis framework e.g. "Analysis Skeleton" supported by the collaboration. An ATLAS internal note has been produced based on an early version of this analysis [3]. Analysis results have been presented in different ATLAS collaboration workshops and phone conferences, e.g. ATLAS Physics Workshop of the Americas, ATLAS Canada Physics Workshop(s) and North South Americas (NSA) top meeting (phone conference) [4–9].

In addition, I did two days of shifts for "M7 friend of data", which is an exercise in looking at the M7 cosmics data offline on May 30-31, 2008 [10]. The goal of the LAr monitoring includes:

- monitor data integrity, e.g. readout driver (ROD) errors from the front end board header monitor (FEBMon),
- monitor detector coverage and the availability of calibrations ("conditions"),
- monitor known bad/noisy channels and look for new ones,

- check the timing of the cosmic ray signal.

Chapter 2

Theoretical Background

2.1 Introduction

It is more than a century since physicists have discovered the atom, which consists of electrons and a nucleus. The electron is still thought to be a structureless point particle and one of the fundamental building blocks of matter. During the 1970's physicists also discovered that the protons and neutrons ("nucleons"), which form nuclei, should no longer be regarded as elementary particles but are found to be made of quarks and gluons that are basic constituents of matter. Based on decreasing size, the current hierarchy of the structure of matter is in the sequence: atoms $\rightarrow$ nuclei $\rightarrow$ nucleons $\rightarrow$ quarks. Particles that contain quarks and gluons are called hadrons. These hadrons, like atoms, can be classified in groups with similar properties, e.g. baryons (three quark state) or mesons (two quark state). We know of six leptons and six quarks as well as their antiparticles, which are categorized into so-called three "generations" or "families" according to certain characteristics.

Together with our changing conception of elementary particles, our understanding of the basic forces of nature and thus of the fundamental interactions between elementary particles has evolved. This evolution started by the end of the 19th century, when electricity and magnetism were understood to be manifestations of the same phenomena: electromagnetism. When nuclear physics developed, two new short-ranged forces became apparent, e.g. the strong nu-

clear force, which acts between nucleons, and the weak nuclear force, which manifests itself in nuclear β-decay. The nuclear force is a result of the strong force binding quarks to form hadrons, which is analogous to the electric force between atoms in molecules. The currently known fundamental forces are the gravitational, electromagnetic, weak and strong forces.

The SM, resulting from an immense experimental and theoretical inspired effort over the last several decades, explains the elementary particles and the interactions among them except the gravitational interaction which has negligible effect on elementary particles at currently accessible scales. The theory of quantum electrodynamics (QED), which is formed by quantizing the theory of classical electrodynamics, is based on the electromagnetic interaction. The theory of weak interactions (sometimes called quantum flavour-dynamics) explains how the elementary particles are weakly interacting and the interactions are mediated by massive intermediate vector bosons. This is a unique interaction, where the particles are capable of changing their flavour and which violates some symmetries, e.g. parity and charge-parity. In the sixties, the electromagnetic and weak interactions were unified in a single electroweak theory by Glashow [11], Weinberg [12] and Salam [13], employing the Higgs mechanism of spontaneous symmetry breaking.

The theory of quantum chromodynamics (QCD) describes the interactions between quarks and gluons, which has two distinct features: asymptotic freedom and confinement. Confinement (often called colour confinement) is the physics phenomenon that colour charged particles (such as quarks and gluons) cannot be isolated, and therefore cannot be directly observed. Asymptotic freedom means that the strength of the interaction decreases with increasing energy. Tables 2.1 and 2.2 shows the three generations of fermions (leptons and quarks) and their physical properties. Leptons interact through the electromagnetic interaction (if they are charged) and the weak interaction, whereas quarks interact through the electromagnetic, weak and strong interactions. All fermions are spin-1/2 particles and have their own anti-fermions. The first

generation of quarks (up and down quarks) and leptons (electrons and electron neutrinos) are known to be the normal matter particles.

Table 2.1: Basic properties of leptons.

Name	Symbol	Generation	Charge (e)	Antiparticle
Electron	e^-	1	-1	e^+
Electron neutrino	ν_e	1	0	$\bar{\nu}_e$
Muon	μ^-	2	-1	μ^+
Muon neutrino	ν_μ	2	0	$\bar{\nu}_\mu$
Tau	τ^-	3	-1	τ^+
Tau neutrino	ν_τ	3	0	$\bar{\nu}_\tau$

Table 2.2: Basic properties of quarks.

Name	Symbol	Generation	Charge (e)	Antiparticle
Up	u	1	+2/3	$\bar{u}$
Down	d	1	-1/3	$\bar{d}$
Charm	c	2	+2/3	$\bar{c}$
Strange	s	2	-1/3	$\bar{s}$
Top	t	3	+2/3	$\bar{t}$
Bottom	b	3	-1/3	$\bar{b}$

Three of the four basic interactions in nature are mediated by the exchange of intermediate or short lived virtual particles. Photons (γ), which are chargeless, massless and stable with infinite life time, are the mediator of electromagnetic interaction. Gluons (g) mediate the strong nuclear force, or simply strong force. Three massive vector bosons $W^\pm$ (charged) and Z^0 (neutral) are responsible for mediating the weak interaction, whereas the graviton (proposed), a spin 2 particle, is the mediator of the gravitational interaction. Table 2.3 shows the mediators of the corresponding interactions and their properties.

Table 2.3: Basic properties of mediators.

Interaction	Name	Symbol	Spin	Mass (GeV/c^2)	Charge
Electromagnetic	photon	γ	1	0	0
Weak		$W^{\pm}$	1	80.417 ± 0.10	± 1
		Z^0	1	91.187 ± 0.007	0
Strong	gluon	g	1	0	0
Gravitational	graviton (proposed)	G	2	0	0

2.1.1 Challenges to the Standard Model

Although the SM has been successful in explaining experimental results, it has still a number of deficiencies and unexplained features, for example,

- One of the most important unanswered questions of the SM is the origin of mass of particles, which can be explained via the Higgs mechanism but the Higgs particle is yet to be discovered.
- The model has 19 free parameters, such as particle masses (plus neutrino masses) which cannot be independently calculated using the model itself.
- "Hierarchy problem", i.e. why the natural scale of gravity $\sim 10^{19}$ GeV is much larger than the electroweak scale $\sim 10^2$ GeV?
- In the SM, the strong and electroweak interactions are not unified.
- Are there any other generations of elementary particles?
- Astrophysical measurements of the rotations of galaxies indicate that normal baryonic matter makes up only about 4% of the total energy density of the Universe - what is the rest?
- Why is the world we observe made up almost entirely of matter, while it is expected that equal quantities of matter and antimatter were produced in the Big Bang?

- Are neutrinos Majorana or Dirac particles?

Most of these outstanding issues require a theory beyond the SM. More details on the SM can be found elsewhere since it is described in great detail in many textbooks [14–17].

2.2 Physics motivations of the LHC experiments

Due to its unprecedented centre of mass energy (14 TeV) the LHC will provide a wide range of opportunities for physics studies. Specifically, it is hoped to help solve some of the SM deficiencies and provide consistency checks of its measured parameters at a TeV energy scale. The principle goals of the ATLAS experiment are discussed below:

- Precision measurements of the SM parameters: In addition to the large discovery potential, the ATLAS experiment will also be able to perform precise measurements of many SM processes. Cross sections of various SM processes in pp collisions at the LHC and $p\bar{p}$ at the Tevatron (currently the highest energy particle accelerator in the world before the LHC) as a function of the energy are compared in figure 2.1. The huge cross-sections and the high collision energies will allow the exploration of less well tested areas of the SM and to improve significantly on the precision of many parameters. For instance, the production cross-sections for the heavy gauge bosons W and Z, and $t\bar{t}$ quark pairs are significantly larger at the LHC than at the Tevatron because of the higher energies [18]. Many SM physics processes contain one or more jets in their final states and therefore the precise jet energy scale measurement is very important, which is the goal of this thesis.

- Higgs: One single most important expectation from the ATLAS experiment is to find the Higgs boson if it exists in nature. The Higgs discovery

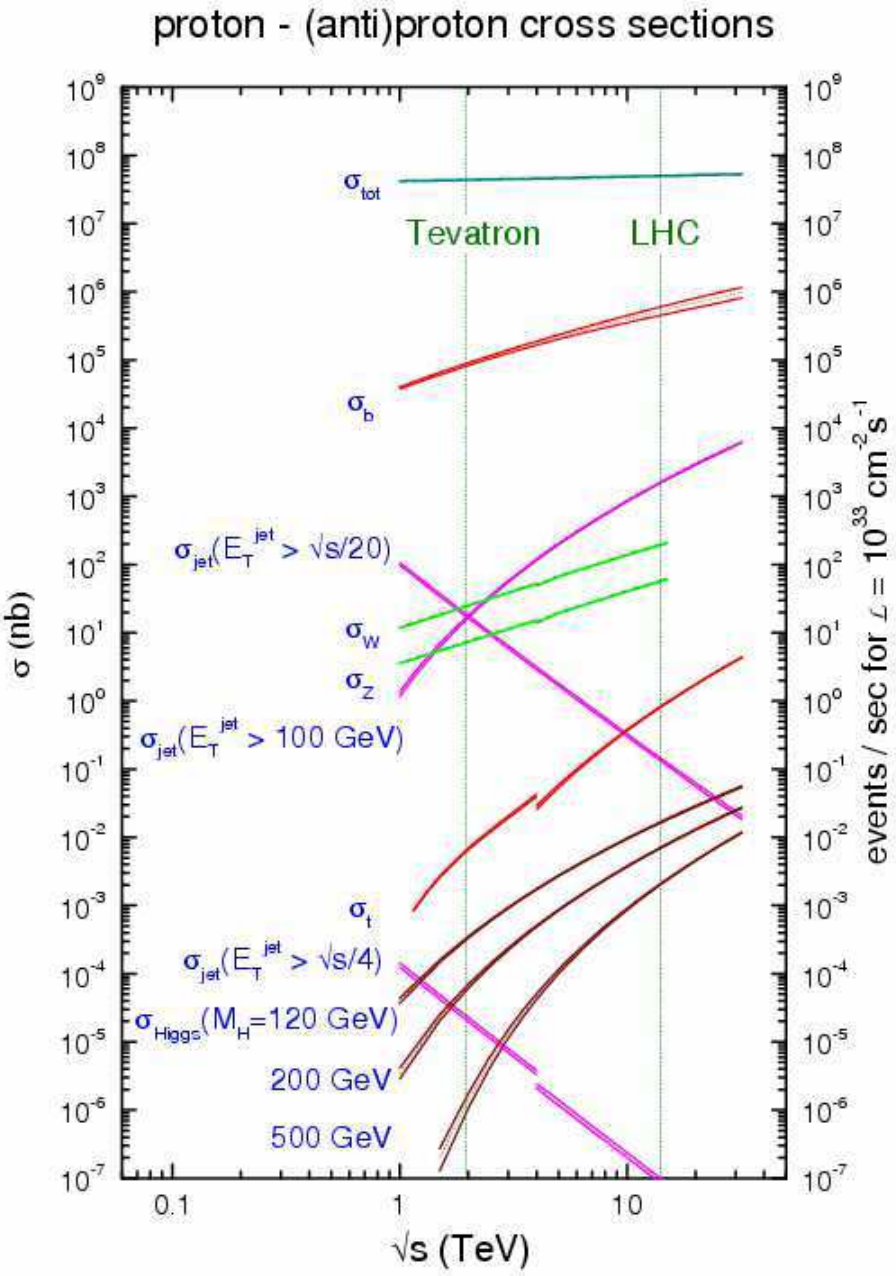

Figure 2.1: Cross-sections of various SM processes in (anti)proton-proton collision in the Tevatron and LHC energy ranges [2].

potential was one of the benchmarks for designing the ATLAS detector. According to the SM, elementary particles gain their masses via the Higgs mechanism. Since this predicted SM particle (Higgs boson) has not yet been found and depending on its mass, different decay channels become available for experimental observations. Figure 2.2 shows the decay channels of SM Higgs. Direct searches at the e^+e^- collider LEP have led to a lower bound on the Higgs boson mass of 114.4 GeV/c^2 [19]. An upper limit of about 1 TeV/c^2 [20] comes from theory (the Standard Model cannot be consistently formulated with a higher Higgs mass). Some of the best experimental signatures for observing the Higgs are expected to be:

- for $m_H < 120$ GeV/c^2
  $H \rightarrow \gamma\gamma$
  $H \rightarrow b\bar{b}$
- for $120 < m_H < 800$ GeV/c^2
  $H \rightarrow ZZ^{(*)} \rightarrow 4l$
  $H \rightarrow ZZ \rightarrow ll\nu\bar{\nu}$
- for $m_H \sim 1$ TeV/c^2
  $H \rightarrow WW \rightarrow l\nu jj$
  $H \rightarrow ZZ \rightarrow lljj$

- Supersymmetry (SUSY): Supersymmetry, is an extension of the SM, where every elementary particle has a supersymmetric partner, e.g. every fermion should have a "partner" boson (the fermion's superpartner), and vice versa. If SUSY exists, many of the supersymmetric particles like squarks and gluinos are expected to be produced at the LHC and be detected in the ATLAS detector.

- B-physics: Large amounts of b-quarks are expected at the LHC and will be used to study the flavour sector and constrain the Cabibbo-

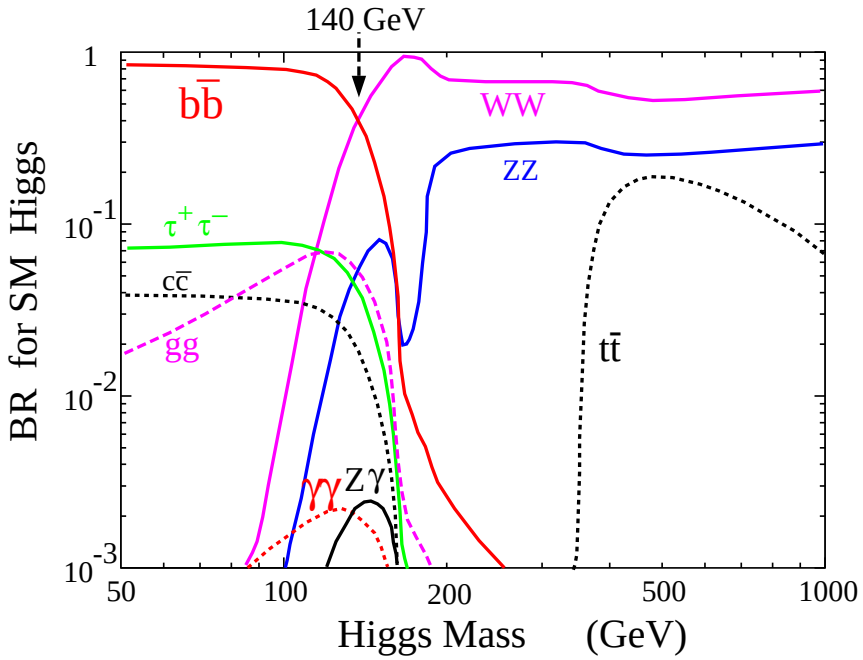

Figure 2.2: The branching ratios of the SM Higgs as a function of mass [21].

Kobayashi-Maskawa (CKM) mixing matrix [22]. One of the LHC experiments LHCb is specially dedicated to b-physics. The LHC will produce about 10^{12} $b\bar{b}$ pairs per year even with low luminosity (10^{33} cm^{-2}s^{-1}). This excellent statistics allow a wide programme of b-quark physics to be performed at the LHC, both with the LHCb and general purpose detectors (ATLAS and CMS).

2.3 Top quark physics at the LHC

The top quark was discovered at Fermilab in 1995 [23,24], which completes the three generation structure of the SM and opens up the new field of top-quark physics. The top quark, according to the SM, is a spin 1/2 and charged +2/3 particle, transforming as a colour triplet under the group SU(3) of the strong interactions and as the weak-isospin partner of the bottom quark. The top quark, the most massive quark, is comparable in mass to the Electroweak Symmetry Breaking (EWSB) scale [25] and therefore any new physics in con-

nection with EWSB would preferentially couple to the top quark. The top quark mass is a fundamental parameter of the SM. Due to its large mass, the only place to study top quarks today is at the Tevatron collider (before the LHC starts up), where the limited number of top quarks and substantial backgrounds make the measurement of its properties a challenging exercise. Ten years after its discovery, we still know little about the top quark and therefore the precision measurements of its properties are crucial in order to unveil the top quark's true nature. On the other hand, the top quark signal is the most important source of background to new physics signals and therefore a detailed understanding of the top quark production rates and decay properties will be necessary for new discoveries. According to the SM, the accuracy of the top quark mass (m_t) measurement ($\delta \mathrm{m}_t$) is required to be less than the width of the top quark. At the Tevatron Run-II, $\delta \mathrm{m}_t \sim 2$ - 3 GeV/c^2 and it is expected to be reduced to $\delta \mathrm{m}_t \sim 1.5$ GeV/c^2 at the LHC, which is the same as the top quark width Γ_t. At the LHC, the statistical precision on the top quark mass will not be as big a problem as the systematic error. For example, after one year of LHC data taking at low luminosity the statistical precision on the top quark mass measurement will be better than 100 MeV/c^2, whereas the systematic error will be of the order or bigger than 1 GeV/c^2 [26, 27]. Due to the increased centre of mass energy (14 TeV), the cross-sections are also increased at the LHC when compared to the Tevatron, as illustrated in figure 2.1. For example, the rate of the dominant process for the top quark production is about 100 times larger than at the Tevatron, leading to a factor of a thousand in top event production at the LHC for one year of data taking at a luminosity of 10^{33} cm^{-2}s^{-1}.

2.3.1 Top quark production at the LHC

According to the standard model, top quark pair production at the LHC shown in figure 2.3, proceeds via gluon fusion (90% of the total $t\bar{t}$ cross-section) and quark-antiquark annihilation (remaining 10% of the cross-section), whereas

at the Tevatron ($\sqrt{s}$ = 1.96 TeV) the numbers are 15% and 85%, respectively. The most recent cross-section prediction for top quarks at the LHC to next-to-next-to-leading order (NNLO) including soft-gluon corrections is $\sigma(t\bar{t}) = 873$ pb for $m_t = 175$ GeV/c^2 [28]. The corresponding value measured at the Tevatron is 6.77 ± 0.42 pb [29].

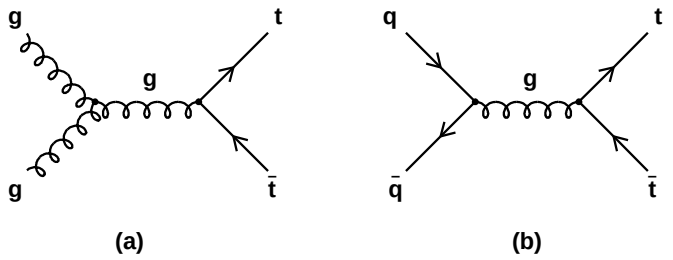

Figure 2.3: Top quark pair production at the LHC (a) gluon fusion process and (b) quark-antiquark annihilation.

Based on the large cross-section, the LHC will be a top quark factory as more than 8 million $t\bar{t}$ pairs will be produced per year at low luminosity (corresponding to an integrated luminosity of 10 fb^{-1}). This high statistics allows us to study the top quark properties with high precision. Top quark properties (e.g. m_t) can be measured based on distributions of top quark decay products. The decay modes of the top quark are discussed in section 2.4.

2.3.2 Single top quark production at the LHC

Another large source of top quarks at the LHC is single top quark production via Wg fusion, Wt and W^* processes, which are shown in figure 2.4. The top quark production cross-sections at the LHC are shown in table 2.4. These single top quarks are one of the possible backgrounds to the study presented in this thesis.

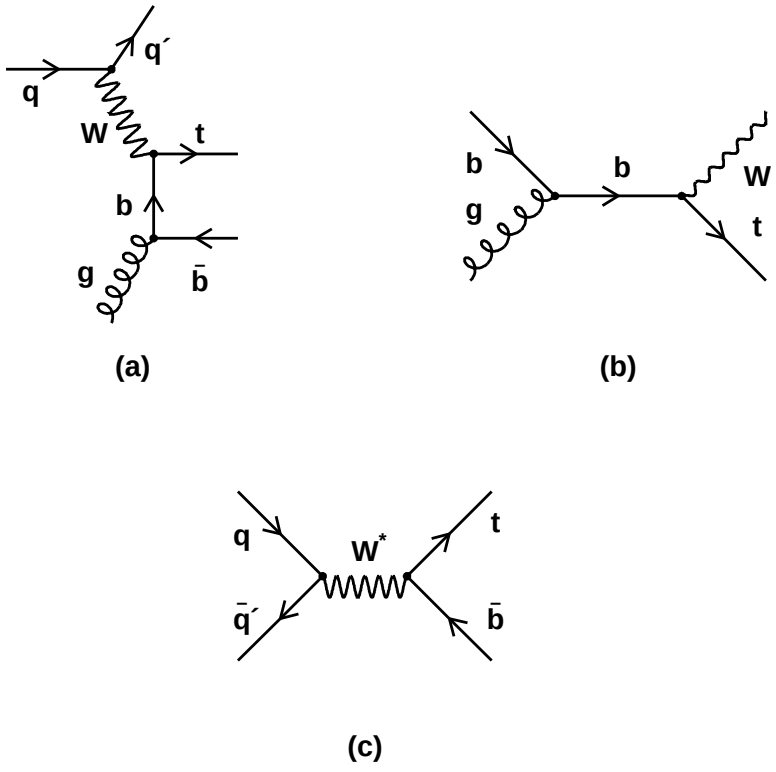

Figure 2.4: Single top quark production at the LHC (a) Wg fusion (b) Wt and (c) W^* processes.

Table 2.4: Cross-sections for top quark production processes at the LHC.

Process	Cross-section (pb)
$t\bar{t}$	873 [28]
Wg-fusion	244 [30]
Wt	60 [31]
W^*	10 [32]

2.4 Top quark decay

According to the SM, the top quark width Γ_t is approximately 1.4 GeV for a top quark mass of 175 GeV/c^2 [33], which leads to a prediction for the top quark lifetime of $\tau_t \cong \hbar/\Gamma_t \approx 5 \times 10^{-25}$ s. The top quark will decay like a bare quark (without first forming hadrons) since τ_t is less than the hadronization[1] time ($\sim 10^{-24}$ s). Because of the low values in CKM matrix for $|V_{td}|$, $|V_{ts}| \ll |V_{tb}| \approx 1$ [34], the top quark decays almost exclusively to a single mode $t \to Wb$. The bottom quark will hadronize forming a jet of hadronic particles. The final state topology of the $t\bar{t}$ event then fully depends on the decay modes of the W bosons, and thus $t\bar{t}$ events can be classified into three channels: the lepton plus jet channel, the dilepton channel and the all jets channel. The three channels are explained in the following sections.

Due to colour confinement, the constituents of hadronic particles (quarks and gluons), never appear directly; the closest one can get to their observation and study is through the jets. A jet is a narrow cone of hadrons produced by the hadronization of a quark or gluon. Jets are produced in QCD hard scattering processes, creating high transverse momentum quarks or gluons, or collectively called partons in the partonic picture. Jet objects can be distinguished in different categories, e.g. purely electromagnetic (e^+, e^-, γ) jets, b-jets and light (d, u, c, s quarks) jets.

[1]The process of the formation of hadrons out of quarks and gluons, which occurs after the hard scattering.

2.4.1 Multi-jet channel

In this mode, both W's in $t\bar{t}$ events decay into two light jets and the final state topology becomes $t\bar{t} \rightarrow W^+W^-b\bar{b} \rightarrow (jj)(jj)b\bar{b}$. The product of branching ratios of the W of $\frac{6}{9} \times \frac{6}{9} \approx 44.4\%$ [see appendix A] implies the production of 4 million[2] multi-jet events with an integrated luminosity of 10 fb^{-1}. One of the main difficulties of this mode is to extract the signal from the huge background of QCD multi-jet events. In addition, the all-jet final state poses difficulties for triggering. For example, the trigger examined so far by ATLAS [35] considers multi-jet trigger thresholds only up to four jets, for which a jet transverse energy (E_T) threshold of 55 GeV is applied at low luminosity. To determine the appropriate thresholds for a six-jet topology further studies are required. Another challenging point of this signature is the presence of a high combinatorial background when reconstructing the top quark invariant mass. We will not use this channel in this thesis for reconstructing the W mass.

2.4.2 Di-lepton channel

Di-lepton events, where each W decays leptonically, provide a particularly clean sample of $t\bar{t}$ events, although the product of branching ratios of the W is small, $\frac{2}{9} \times \frac{2}{9} \approx 4.9\%$ (only the e and μ are considered). With this branching ratio, one expects the production of over 400,000 di-lepton events for an integrated luminosity of 10 fb^{-1}. The main contributions to backgrounds come from Drell-Yan production, $W \rightarrow l\nu$ + jets events where a jet is misidentified as a lepton and diboson (WW, WZ and ZZ) production. In this thesis, we can not use this channel because there are no light jets in the final state of $t\bar{t} \rightarrow W^+W^-b\bar{b} \rightarrow (l\nu_l)(l\nu_l)b\bar{b}$. Moreover, this sample has limited use in probing the top reconstruction capability of the ATLAS experiment, due to the two neutrinos escaping detection.

[2]The LHC will produce 10^7 events at an integrated luminosity of 10 fb^{-1}.

2.4.3 Lepton plus jets channel

The single lepton plus jets topology, $t\bar{t} \rightarrow W^+W^-b\bar{b} \rightarrow (l\nu_l)(jj)b\bar{b}$ shown in figure 2.5, arises in $2 \times \frac{2}{9} \times \frac{6}{9} \approx 29.6\%$ (e/μ plus jets) of all $t\bar{t}$ events. One expects, therefore, production of almost 2.5 million single lepton plus jet events for an integrated luminosity of 10 fb^{-1}, corresponding to one year of LHC running at a luminosity of 10^{33} cm^{-2}s^{-1}. The presence of a high p_T (transverse momentum) isolated lepton provides an efficient trigger. The lepton and the high value of the missing E_T give a large suppression of backgrounds from QCD multi-jets and $b\bar{b}$ production. The single lepton plus jets sample, is known as the golden channel as it has a very characteristic experimental signature (as shown in fig. 2.5) that allows one to obtain a clean sample of top events. Due to a compromise between signal statistics and manageable backgrounds, the most precise measurements of top-quark properties are obtained from the lepton plus jets channels. Semi-leptonic top quark events include:

- an isolated high-momentum lepton (e or μ),
- missing transverse energy,
- four high-momentum jets, of which two jets originate from the decay of a W-boson and two jets that originate from b-quark fragmentation.

The most significant background contribution in the lepton plus jet channel is from W + jets events, multi-jet events with one jet misidentified as a lepton, diboson and single top quark production. W + jets (2, 3, 4 or 5 jets) are used in this thesis as background. Since the centre of mass energy is much higher than the W boson mass (m_W), there will be huge direct real W production at the LHC. QCD predicts that one or more partons can also be produced in the hard scatter in association with the W boson.

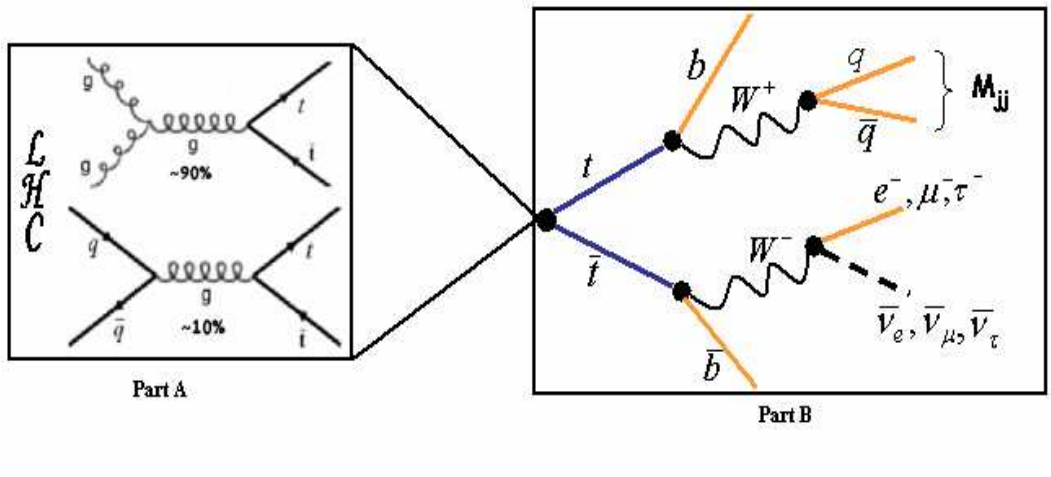

Figure 2.5: Final state topology in lepton plus jets in $t\bar{t}$ events. Part A shows the production of $t\bar{t}$ events in the LHC and part B shows the semileptonic top quark decay where one W decays to leptons (e, μ, τ) and the other W decays to two light jets (q, $\bar{q}$).

2.5 Hadronic top quark decay

The hadronic top quark decay (e.g. $t \rightarrow bW \rightarrow bjj$) contains a light jet pair (from the W resonance) and a b-jet in its final state, and therefore the precise measurement of the top quark properties are based on the absolute jet energy scale from the bottom and light quarks. The mass of the W is also a fundamental parameter of the SM. The LHC will be an extremely copious source of W bosons, thus allowing in principle for a statistically very precise measurement of its mass. It is expected that a precision better than $\delta m_W \sim 15$ MeV/c^2 could be attained at the LHC with low luminosity [36]. Precise top quark properties depend on the precise W measurement. The lepton plus jets channel is of particular interest since it contains two b-jets, two light jets, one lepton and one neutrino as shown in figure 2.5. It deals with many detector characteristics and performances issues related to lepton momentum and identification, jet reconstruction and calibration, missing en-

ergy and b-tagging. Top events will be very useful for providing feedback on detector performances and as a calibration tool [2]. The lepton plus jets channel, where at least one $W \rightarrow jj$, provides an excellent tool to determine the jet energy scale *in situ* since the mass (80.398 ± 0.025 GeV/c^2) and width (2.141 ± 0.041 GeV/c^2) of the W boson is known with high accuracy [37]. The overall energy scale for light jets can be determined by constraining the invariant mass of the two jets, assigned to the hadronic decays of the W, to the W mass [38].

Efficient b-tagging needs a precise alignment of the inner tracking detectors in ATLAS. It will take a long time to understand all systematic uncertainties in b-tagging (about one year to reach the nominal precision on the alignment). Light jet energy calibration can be done *in situ*, since a top quark signal can be extracted without b-tagging, which is important at the early stage of the LHC running. A detailed explanation of jet energy calibration can be found in chapter 5.

Chapter 3

The LHC and ATLAS

3.1 The LHC

The Large Hadron Collider [39], located at CERN, is built to collide two counter rotating beams (of energy 7 TeV each) of protons (hadrons) and/or heavy ions (also hadrons) head-on with a total collision energy (centre of mass energy) of 14 TeV. Higher energies are needed since we are trying to make the collision as short range as possible. The collision range can be made short by increasing the particle's momentum according to the following de Broglie wavelength:

$$\lambda = \frac{h}{p}, \tag{3.1}$$

where h is Plank's constant and p is the particle's momentum.

Two general purpose detectors ATLAS [40] and CMS [41] and two other specialized detectors LHCb [42] and ALICE [43] are available at the LHC. Figure 3.1 shows the accelerator facilities at CERN, where 50 MeV proton bunches (10^{11} protons/bunch) start off through the LINAC2. These bunches are then transferred to the PS Booster (PSB), where the energy is increased to 1.4 GeV. The energy is further increased to 26 GeV by the Proton Synchrotron (PS). The protons are then injected into the Super Proton Synchrotron (SPS) where they are accelerated to 450 GeV. Finally, the SPS injects the protons clockwise and counter-clockwise into the LHC ring, where they are accelerated

to their final energy of 7 TeV. More than 1,200 dipole magnets are installed along the LHC ring to keep the protons on track in the ring. The dipoles provide a magnetic field of up to 9 Tesla. The basic parameters of the LHC accelerator are given in table 3.1.

Table 3.1: Basic design parameters of the LHC.

Parameter	Value	Unit
Circumference	26,658.883	m
Injection energy	0.45	TeV
Proton energy	7	TeV
Collision Energy	14	TeV
Dipole field at 7 TeV	8.33	T
Bunch separation	25	ns
Luminosity	10^{34}	$\mathrm{cm}^{-2}\mathrm{s}^{-1}$
Luminosity lifetime	10	hours
Helium Temperature	1.9	K
Particles/bunch	10^{11}	
Collision points	4	
Number of main bends	1,232	

Like its centre of mass energy, the luminosity of the LHC is also unprecedented for a proton collider. The specific luminosity is defined as the number of protons that pass by per unit area per unit time, mathematically:

$$L = \frac{1}{4\pi}\frac{N^2 f}{\sigma_x \sigma_y t}, \tag{3.2}$$

where N is the number of protons per bunch (10^{11}), f is the fraction of bunch positions containing protons (0.8), σ_x and σ_y are the transverse dimensions of the gaussian beam profiles (horizontal and vertical, 14.4 μm each) and t is the time between bunches (25 ns). The higher the luminosity, the more proton-proton interactions per second will occur. The production rate of particles can be calculated by

$$R = \sigma L, \tag{3.3}$$

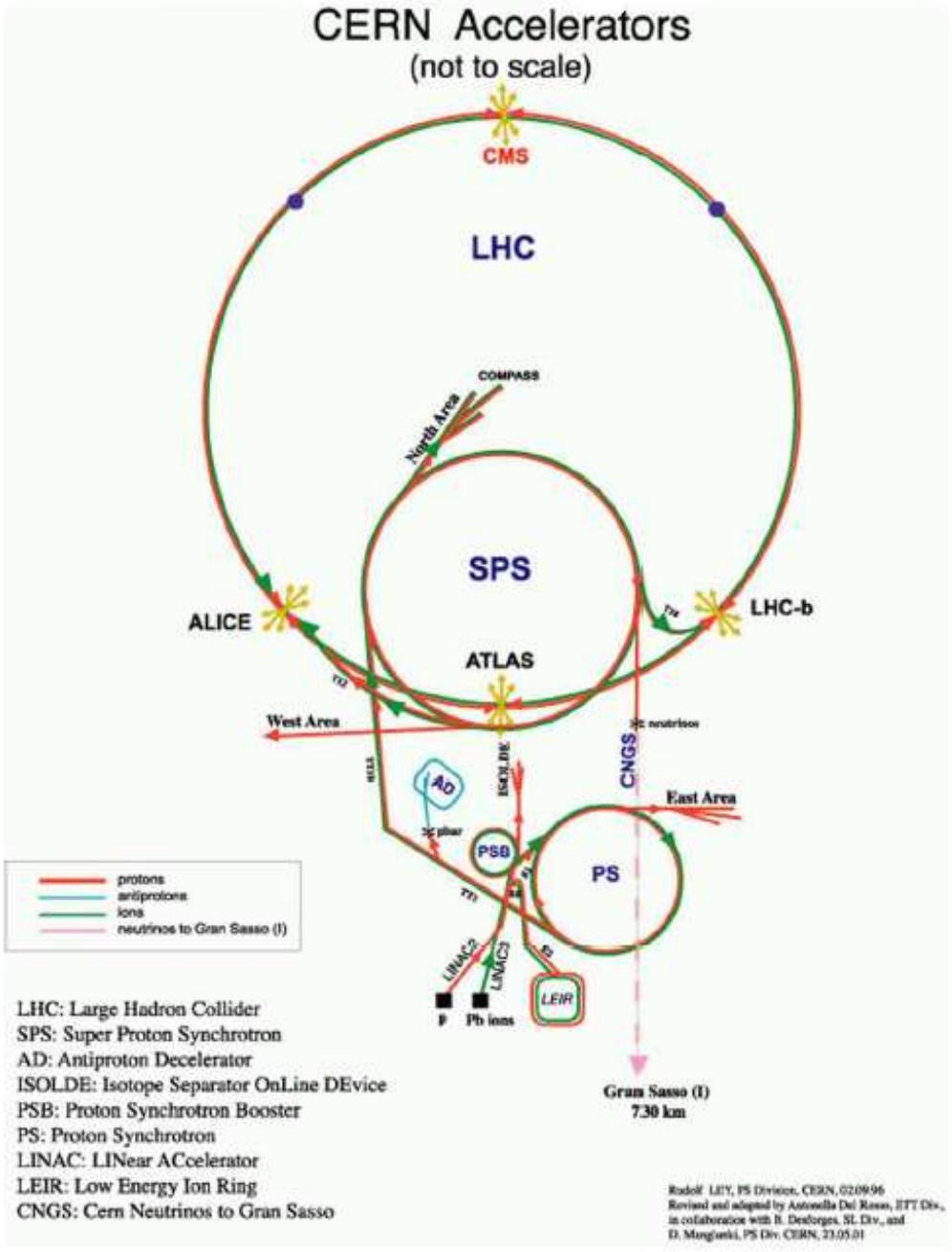

Figure 3.1: Accelerator facilities at the LHC [48].

where L is the specific luminosity described above and σ is the cross-section. High luminosity is needed because many interesting physics processes at the LHC energy are thought to have very small cross sections, e.g. 1 pb or less. The high luminosity also mandated the use of radiation-hard materials in detector construction and causes a significant source of noise known as pileup. The small bunch separation requires fast readout electronics to avoid sampling events from several different bunch-crossings simultaneously. When events from more than one bunch-crossing are measured together they are said to have "piled-up" in the detector. In addition to a possible hard-scatter event of interest, on average, 23 minimum bias events (events from the soft interactions with low transverse momentum and multiplicity, etc..) will be produced per bunch-crossing at LHC design luminosity. These minimum bias events will produce more than 3,000 charged particles in the detector for each bunch-crossing [47].

3.1.1 Why hadrons, not leptons or anti-hadrons?

An accelerator can only accelerate a certain kind of particles: firstly they need to be charged (as the beams are manipulated by electromagnetic devices that can only influence charged particles), and secondly, except in special cases, they should not decay. This limits the types of particles that can practically be accelerated to electrons, protons, and ions, plus their antiparticles. The LHC will accelerate two beams of particles of the same kind, either protons or lead ions, which are hadrons. Charged particles with very high speed, emit an electromagnetic radiation called synchrotron radiation when they are traveling in a circular path. The total energy loss per unit time is given by:

$$\frac{dW}{dt} = \frac{2c}{3} e^2 \beta^4 \left[\frac{E}{mc^2}\right]^4 \left(\frac{1}{r^2}\right) \tag{3.4}$$

where $\left[\frac{E}{(mc^2)}\right]^4 = \gamma^4$, m is the mass of the particle, r is the bending radius and $\beta = \frac{v}{c}$. From equation 3.4, we see that the energy loss for protons (around 2,000 times more massive than electrons) is much smaller than for light particles such

as electrons. Therefore, in circular accelerators, to obtain the highest-energy collisions it is more effective to accelerate massive particles. Also protons are easier to produce than anti-protons.

Protons are spin-$\frac{1}{2}$ fermions and composed of three valence quarks [45]. The two up quarks and one down quark are held together by the strong force mediated by gluons. At any given moment the proton might actually contain an extra $u\bar{u}$, or $d\bar{d}$, or $s\bar{s}$ or even several such pairs. In principle, it could even have a heavy quark pair $c\bar{c}$, $b\bar{b}$, $t\bar{t}$ but this is far less likely, because of the large mass term in the denominator of the quark propagator. These pairs of quarks are known as "sea quarks". The valence quarks, sea quarks and gluons are the constituents of the proton and known as "partons". Therefore, each parton carries only a fraction of total proton momentum in a collision. The partons carrying the highest momentum are responsible for hard-scatter events, whereas other partons will be responsible for minimum bias events. In the forward regions of detectors (small angles from the beam axis) minimum bias events occur and dominate the total LHC cross-section.

3.2 Detector

Particle detectors are instruments designed for the detection and measurement of sub-atomic particles such as those emitted by radioactive materials, produced by particle accelerators or observed in cosmic rays. The particles include electrons, protons, neutrons, alpha particles, gamma rays and numerous other mesons and baryons. Sensitivities, responses, resolutions and efficiencies are the main features of a modern particle detector. Detectors are built in different ways according to the type of collision they analyze, e.g. cone shaped or rectangular for fixed[1] target experiments, spherical or more commonly cylindrical for colliding[2] beam experiments. Figure 3.2 shows the schematic design of a typical modern high energy particle detector. The reason that detectors

[1]The particles produced are generally flying in the forward direction.
[2]The particles produced have a uniform distribution of momenta.

are divided into many components is that each component tests for a special set of particle properties.

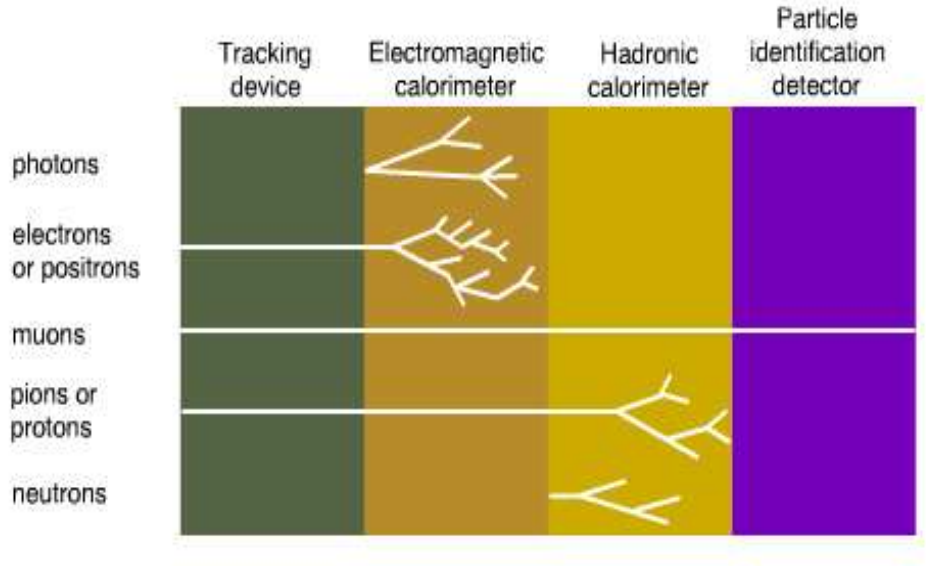

Figure 3.2: Schematic design of a typical modern high energy particle detector [46].

All modern high energy particle detectors contain a tracking detector in its innermost layer and a muon chamber is in the outermost layer. The calorimeters (both electromagnetic and hadronic) are always in the middle of the detector. Figure 3.2 shows:

- Charged particles like electrons, positrons or pions are detected both in the tracking chamber and calorimeter (electromagnetic and hadronic).
- Neutral particles, like neutrons and photons, are not detectable in the tracking chamber; they are only evident when they interact with the detector. Photons are detected by the energy deposit in the electromagnetic calorimeter, while neutrons are detected by the energy they deposit in the hadron calorimeter.
- Muons penetrate all the inner (tracking chamber) and middle (calorimeter) sections of detector and can be detected in muon chambers.

- Each particle type has its own "signature" in the detector.

3.2.1 ATLAS detector

ATLAS is a multi-purpose particle detector and one of four experiments for the LHC that will explore the fundamental nature of matter and the basic forces that shape our universe. With its length of 45 m and height of 22 m, ATLAS is one of the largest and most elaborate particle physics experiments. Its main parts are the inner detector, for measuring the momentum of each charged particle, the calorimeter, for measuring the particle's energy, the muon spectrometer, for identifying and measuring muons, and the magnet system, for bending charged particles for momentum measurement. All those components together have a weight of 7,000 tons. More details about ATLAS can be found elsewhere [40, 48]. An overview of the ATLAS detector indicating different sub-detectors is shown in figure 3.3.

3.2.2 Coordinate system

The ATLAS coordinate system is a right handed system with the X-axis pointing towards the centre of the LHC ring. The beam axis defines the Z-axis, while the Y-axis points upwards. The azimuthal angle ϕ is defined in the XY-plane, with $\phi = 0$ being the positive X-axis. The polar angle θ is defined with respect to the beam pipe, with $\theta = 0$ being the positive Z-axis. This polar angle is related to the pseudo-rapidity by the following formula:

$$\eta \equiv -\ln\left(\tan\frac{\theta}{2}\right), \tag{3.5}$$

which is used for highly relativistic particles, instead of the polar angle. In the limit where the particle is traveling close to the speed of light, or in the approximation that the mass of the particle is nearly zero, pseudo-rapidity is equal to the rapidity:

$$y = \frac{1}{2}\log\frac{E + p_z}{E - p_z}. \tag{3.6}$$

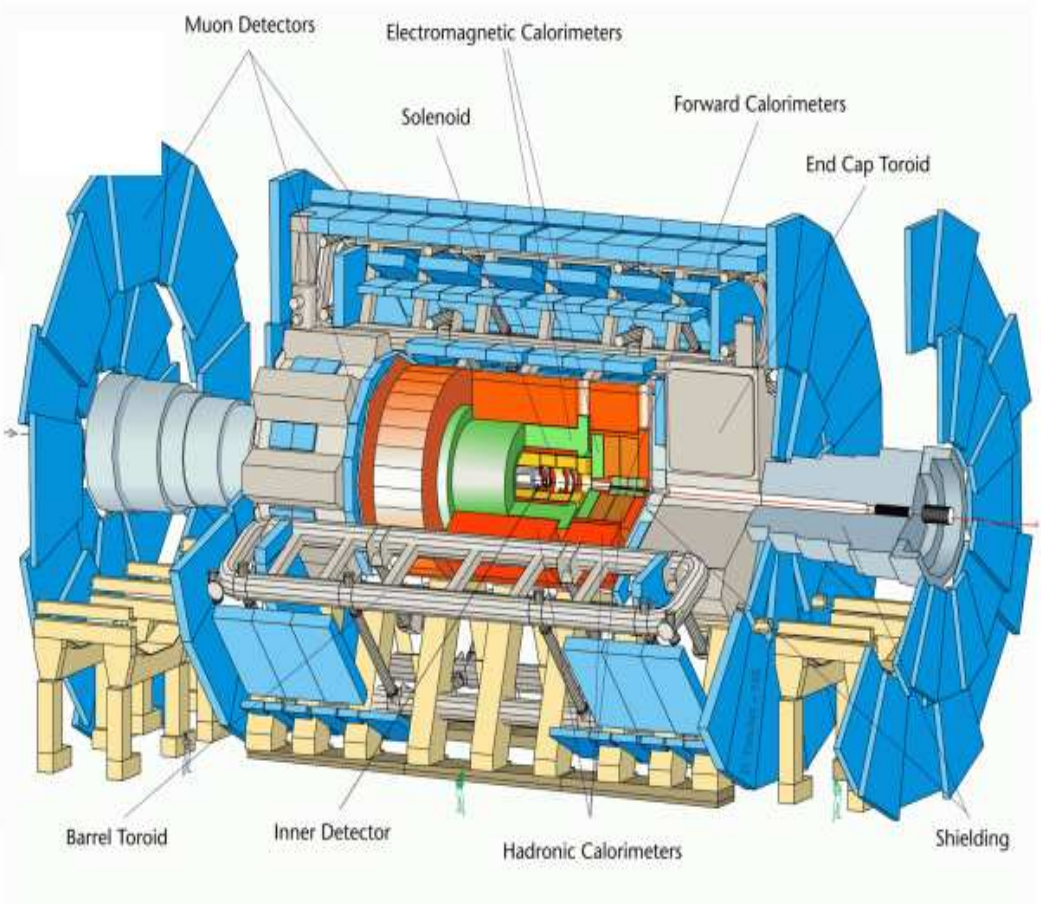

Figure 3.3: Overview of ATLAS detctor.

Since the p_z component (momentum along the beam axis) of the interacting partons is not known and therefore, we cannot use the rapidity as a variable. The particles which are traveling close to the beam pipe ($\theta = 0$) will correspond to high values of pseudo-rapidity ($\eta = \pm\infty$), whereas particles emitted vertical to the beam pipe ($\theta = \frac{\pi}{2}$) will correspond to zero pseudo-rapidity ($\eta = 0$).

3.2.3 The inner detector

The inner detectors, also known as tracking chambers, are the innermost layers of a particle detector, which measure the paths of electrically charged particles through the trails (ionization, excitation, etc.) they leave behind.

These inner regions are filled with highly segmented sensing devices of various kinds. Most modern tracking devices do not make the tracks of particles directly visible. Instead, they produce tiny electrical signals that can be recorded as computer data. A computer program then reconstructs the patterns of tracks recorded by the detector. An example is the curvature of a particle's track (made in the presence of a magnetic field), from which the momentum of a particle may be calculated. This is useful for identifying the particle. Better momentum resolution means better particle mass resolution or better measurements of particles.

The ATLAS inner detector [49] is the closest to the interaction point and installed in a solenoid magnet (superconducting NbTi/Cu), which provides a magnetic field of 2 T. Often it is convenient to use p_T (transverse momentum) instead of $\vec{p}$, since p_T is the component of $\vec{p}$, which is projected on to the transverse plane of the beam axis. Transverse momentum is particularly useful since the longitudinal momentum of the initial partons is not known. The ATLAS inner detector shown in figure 3.4, consists of the following three different sub-detectors:

- a pixel detector with very high granularity will measure the decay vertices accurately;
- a silicon strip detector (SCT, 'SemiConducting Tracker') surrounding the pixel detector, is responsible for precisely measuring the particle momentum; and
- A straw tracker (TRT, 'Transition Radiation Tracker') that surrounds the other two subsystems, with main purpose to measure the position of particle tracks and measure the amount of transition radiation they produce.

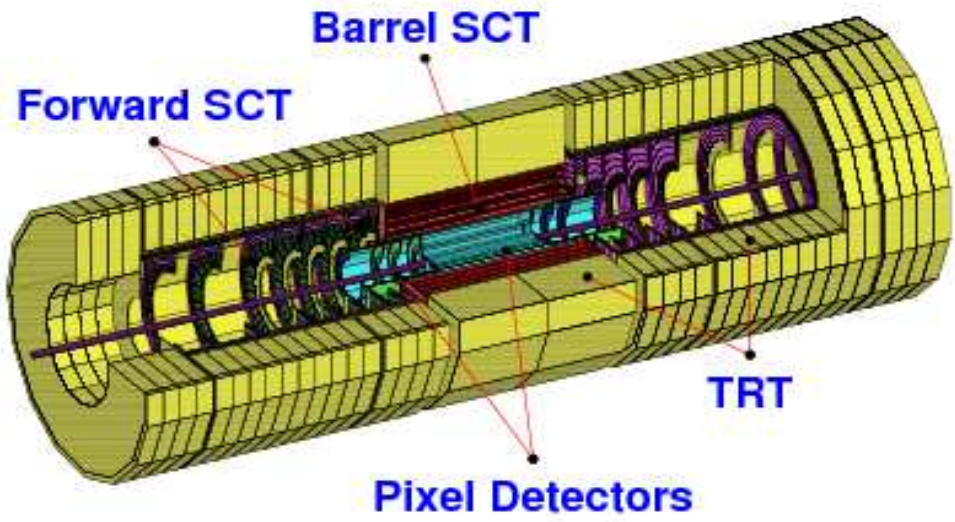

Figure 3.4: Three dimensional view of the ATLAS inner detector. The geometrical acceptance of the ATLAS inner detector, covers the pseudo-rapidity range from -2.5 to $+2.5$.

Pixel detector (PD)

The ATLAS Pixel[3] Detector [50] is the innermost layer of the ATLAS tracking system and will contribute significantly to the critical tracking information for pattern recognition near the collision point and largely determines the ability of the inner detector to find secondary vertices (b-tagging for example). It is composed of modular units, arranged in three barrels concentric with the beam line and centred on the interaction point, and three disks on either side for the forward region. The inner most layer (so-called B layer) is removable and can be replaced to maintain the highest performance throughout the experiment's lifetime. The position of the pixel detector near the interaction point requires excellent radiation hardness, mechanical and thermal robustness and good long-term stability, all combined with a low material budget.

[3]Pixels are small rectangular two-dimensional detector elements.

The distances of the three barrel layers to the beamline are 5.05, 8.85 and 12.25 cm respectively. The disks are perpendicular to the beam pipe and have Z positions between 11 and 20 cm. There are about 1,508 identical barrel modules and about 720 identical disk modules in the system. Each pixel element has dimensions of about 50 μm $\times$ 300 μm, and has its own readout chip and buffering unit for storing the data, while awaiting the decision from the trigger[4] chain. The whole system contains 140 $\times$ 10^6 readout channels, which provide measurements with a resolution of about 12 μm in the r-ϕ plane and 66 to 77 μm in Z for barrel and endcap part. Figure 3.5 shows the three-dimensional view of ATLAS pixel detector.

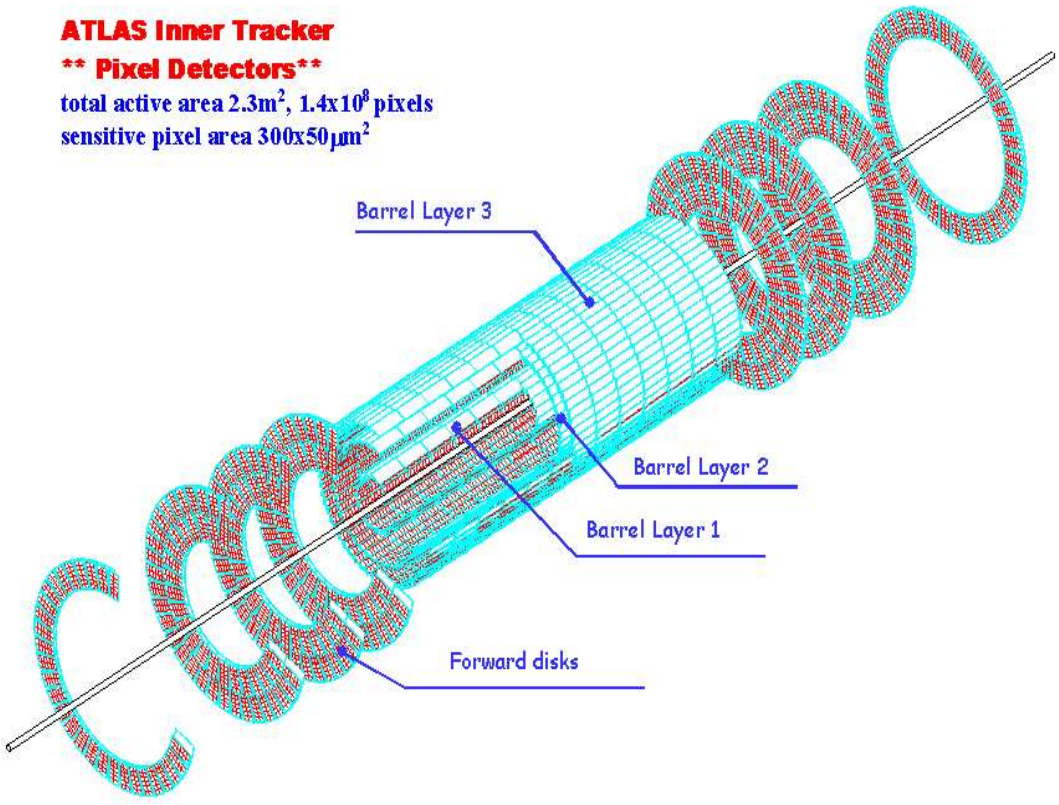

Figure 3.5: 3-D view of ATLAS pixel detector.

[4]Hardware or software based device for the (online-) selection of specific event classes from large datasets.

Semiconductor tracker (SCT)

Semiconductor detectors made of wafers with very small rectangular two-dimensional array are widely used in particle physics experiments. They are fast, accurate and efficient for detecting the passage of charged particles and measuring their position and momentum.

The Semiconductor Tracker (SCT) surrounding the pixel detector is based upon silicon microstrip detector technology. Like the pixel detector, the SCT consists of a barrel detector and two symmetric end-cap detectors. The sensors are segmented in strips. Each silicon detector has an area of 6.36×6.40 cm^2, consisting of 768 readout strips of 80 μm pitch between them. Two such detectors are wire-bonded together to form 12.8 cm long strips. Two such detector pairs are then glued together back-to-back with a small relative angle[5], to form a module as shown in the figure 3.6. The detector is arranged into four barrels and nine end-cap wheels. The barrels have radii of 30, 37, 44 and 51 cm with the radii of each end-cap wheel being varied to ensure coverage in the range $|\eta| < 2.5$ is maintained. In total, the detector contains 61 m^2 of silicon and 6.2×10^6 readout channels. The designed spatial resolution is 16 μm in the r-ϕ plane and 580 μm for the second position coordinate. Two different tracks are detected as one only if they are separated by less than about 200 μm. More details about the SCT can be found elsewhere [51, 52].

Trannsition radiation tracker (TRT)

The Transition Radiation Tracker (TRT), placed in between the silicon tracker and the solenoid magnet is the outermost subdetector in the ATLAS inner detector. It has both barrel and end-cap parts as shown in figure 3.7. The barrel TRT consists of three cylindrical rings, each containing 32 identical and independent modules. Each of the two end-cap TRT parts consists of three sets of identical and independent wheels. The main detector element of

[5]The two layers of the module are rotated by a 40 mrad stereo angle with respect to each other.

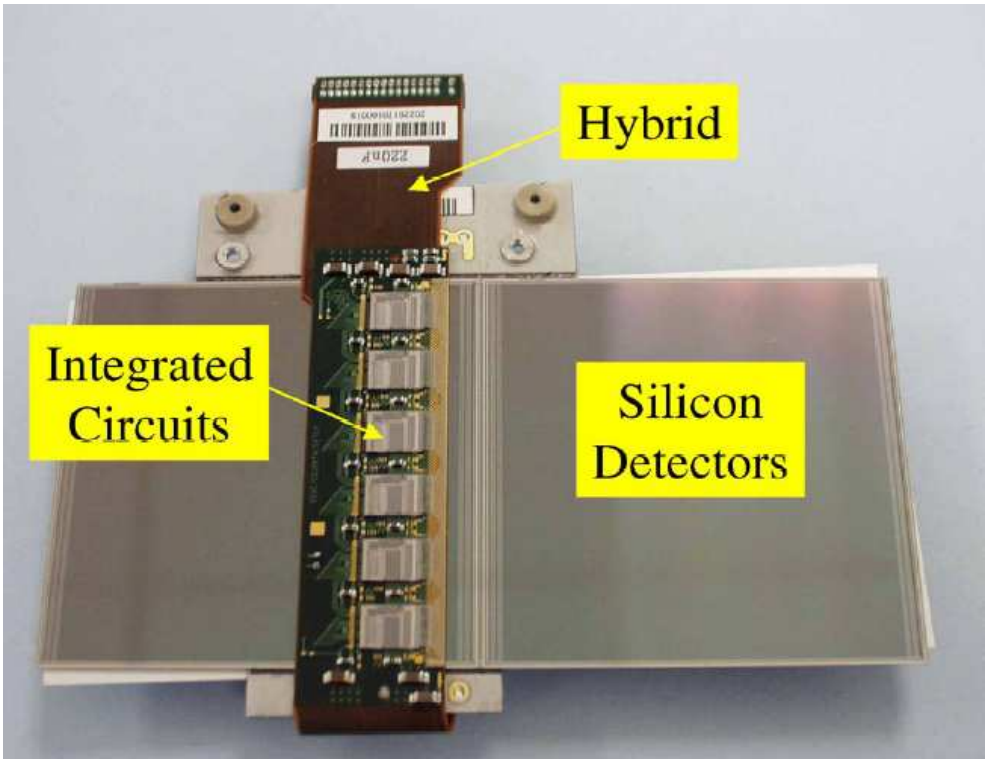

Figure 3.6: An SCT barrel module.

a TRT is a straw detector of 4 mm in diameter, which acts as a drift tube for measuring the position of a track that passes through it and an ionization chamber for recording the amplitude of the signal [53]. The straw is filled with a gas mixture ($Xe:CO_2:CF_4 = 70:20:10$). In the centre of the straw there is a gold-plated W-Re wire of 30 μm diameter, which measures the drift time of the ionizing particles through the gas. There are about 43,000 axial straws arranged in three cylindrical layers[6]. Each straw is divided into two at the centre and read out at both ends. The end-cap part consists of about 320,000 radial straws arranged in 18 wheels (each of the two end-cap consists three sets of wheels and both has three layers mentioned above) on each side, with the readout at the outer radius. A track hits on average 36 straws and the

[6]Type 1 contains $\approx$ 329 axial straws $\times$ 19 layers at inner radius, type 2 contains $\approx$ 520 axial straws $\times$ 24 layers at middle portion and type 3 contains $\approx$ 793 straws $\times$ 30 layers at outer radius, respectively.

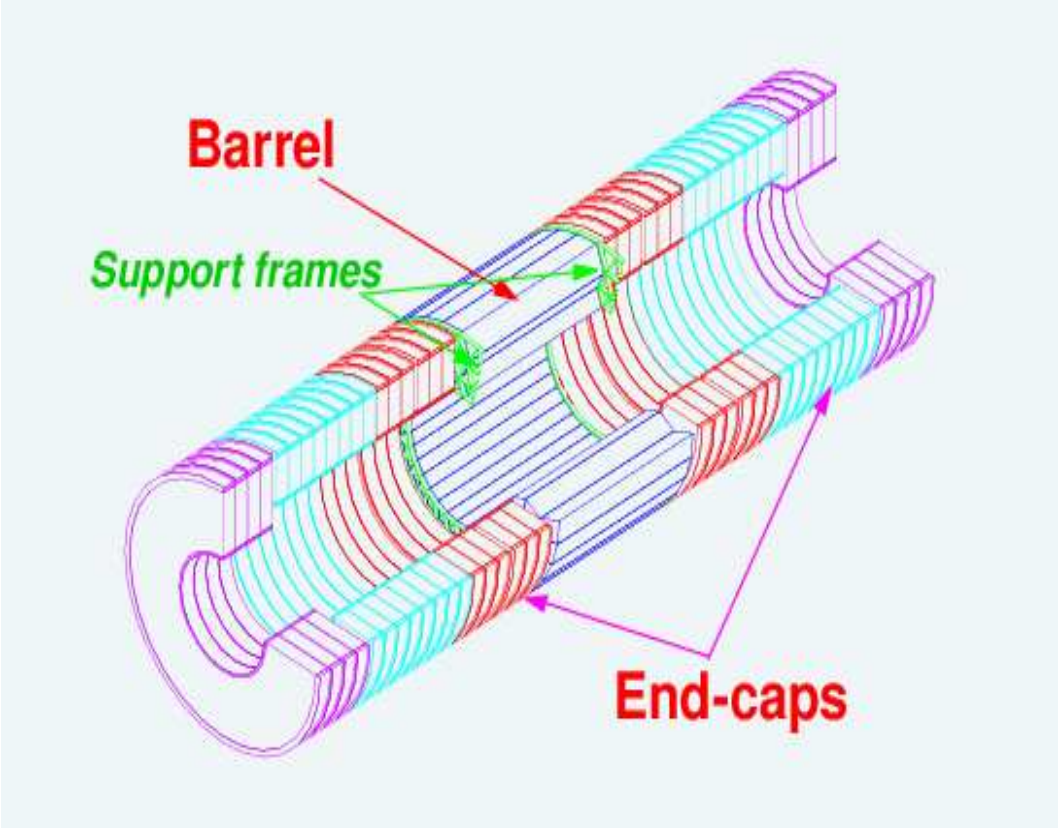

Figure 3.7: View of ATLAS transition radiation tracker.

designed resolution in the position of the hit, for both parts, is 170 μm.

3.2.4 Calorimeter

A calorimeter is a unique device in particle detectors that is used to measure the energy of charged and neutral particles. In principle, the calorimeter should absorb all of the energy of an incident particle. Since the original particle no longer exists after the measurement, the energy measurement by a calorimeter is a destructive process. Calorimeters in a particle detector always exists behind charged particle tracking chambers, which are non-destructive measuring devices.

Calorimeters play a central role in the ATLAS experiment. In particular, calorimeters will be the leading detectors in many measurements for the recon-

struction of physics channels of prime interest. Due to momentum thresholds, we can not reliably measure the charge of the particle after a certain limit using tracking chambers. Additionally, momentum measurements using the magnetic field only works for charged particles, but there are other interesting particles, which are not charged, e.g. photons, η^0s and neutrons, etc.. In these cases one can use the calorimeter. The calorimeters at hadron colliders can offer a lot of functionality. It measures the energy and position of electrons and photons (mostly in electromagnetic part of calorimeter), and it also measures the energy and direction of jets. The calorimeters calculate the missing transverse momentum/energy of the event and identifying particles, e.g. separation of electrons and photons from hadrons and jets, and of τ hadronic decays from jets, event selection at the trigger level, etc. [54].

The ATLAS calorimetry system is subdivided into an inner Electromagnetic Calorimeter (EC) [55] for electromagnetically interacting particles (electrons, positrons, photons, etc.) and an outer Hadronic Calorimeter (HC) for hadrons (pions, kaons, etc.). Both are sampling calorimeters, i.e. they absorb energy in a high-density metal and periodically sample the shape of the resulting particle shower (energy, momentum, etc.). Figure 3.8 shows a cut-away view of ATLAS calorimetry system.

Sampling calorimeter

There are mainly two types of calorimeters, e.g. homogeneous and heterogeneous (also called sampling). In homogeneous calorimeters the functions of passive particle absorption, active signal generation and readout are combined in a single material. Such materials are almost exclusively used for electromagnetic calorimeters, e.g. NaI, CsI, PbO, SiO_2, etc.. But the heterogeneous or sampling calorimeters are composed of alternating layers of absorbers (passive materials) and active materials. This allows an optimal choice of absorber materials and a certain freedom in signal treatment. Only the fraction of the shower energy absorbed in the active material is measured. Hadron calorime-

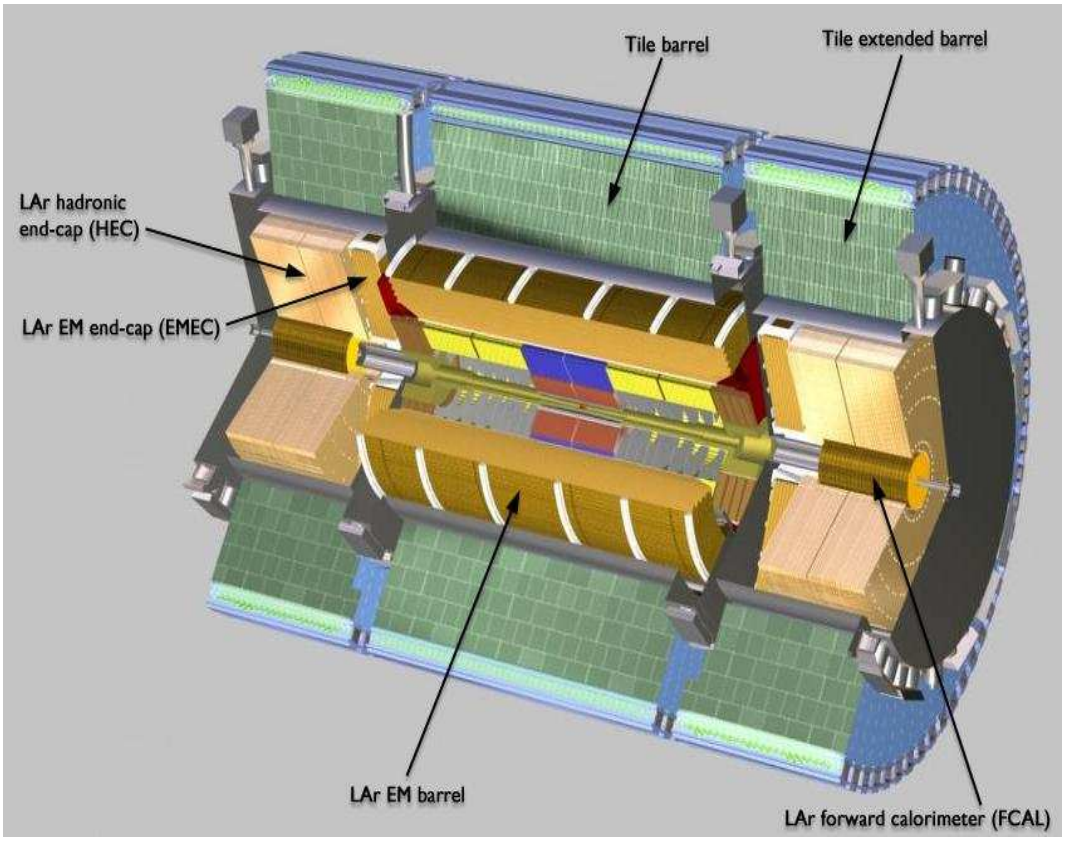

Figure 3.8: Cut-away view of the ATLAS calorimetry.

ters, needing considerable depth and width to create and absorb the shower, are necessarily of the sampling calorimeter type. Sampling calorimeters have the following important advantages:

- They can be made very compact using dense absorber plates, which are useful when the calorimeter is used as a detector subsystem.
- Fine segmentation which is crucial for particle identification and spatial reconstruction.

3.2.5 Electromagnetic calorimeter

The electromagnetic portion of the calorimeter is the closest part to the initial high-energy collision point. The ATLAS electromagnetic detector is

a sampling calorimeter with liquid argon as active material and lead (short radiation length, easy to machine, cheap and radiation hard) absorbers in an accordion geometry. Absorbers, also known as passive materials, cause an incoming particle to initiate a shower and the particles created in this shower are detected in the active material. The total signal in the active material is related directly to the energy of the incoming particle. The lead plates are folded into an accordion shape in both the barrel and end-cap sections [56], which allows calorimeter readout with minimal dead space (hermetic design[7]).

Electromagnetic shower

A shower is a cascade of secondary particles resulting from a high-energy particle interacting with dense matter, e.g. lead. Electromagnetic showers are produced by e, γ etc. via the electromagnetic force. An electromagnetic shower begins when the above mentioned particles enters into a material. When an electron of energy > 10 MeV is incident on matter (lead for example), its primary mechanism of energy loss or to initiate particle cascades through the photon emission is via the bremsstrahlung[8] process. On the other hand, a high energy photon interacting with matter converts into an electron and positron pairs. The resulting electrons and positrons may produce another photon via bremsstrahlung. These in turn convert into further e^+e^- pairs and so on. The result is a cascade or shower of photons, electrons and positrons as shown in figure 3.9. This continues until the energy of the pair-produced electrons and positrons drops below the critical energy[9]. Below the critical energy electrons lose their energy via ionization and photons lose their energy by Compton and Rayleigh scattering. Electromagnetic showers are characterized longitudinally by the radiation length X_0 [57] and by narrow transverse profiles. The radia-

[7]It covers nearly all of the 4π steradians of solid angle around the interaction point.

[8]Bremsstrahlung radiation is the radiation due to the deceleration of a charged particle, such as an electron, when deflected by another charged particle, such as an atomic nucleus.

[9]The critical energy is the energy at which the energy lose via ionization is equal to the energy lose via bremsstrahlung.

tion length X_0 is defined as the distance that an electron travels in a materials such that its energy is reduced by 1/e:

$$X_0 = \frac{716.4A}{Z(Z+1)\ln\left(\frac{287}{\sqrt{Z}}\right)}, \tag{3.7}$$

where A is the atomic mass and Z is the atomic charge of the material. The

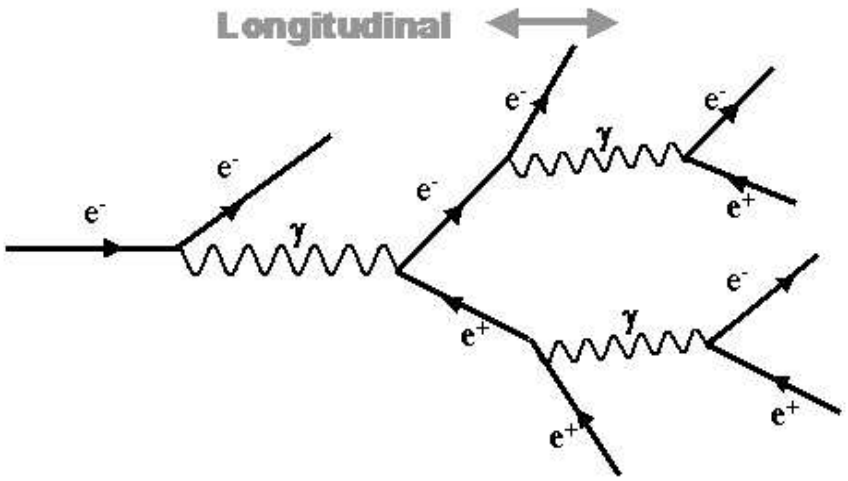

Figure 3.9: Schematic view of an electromagnetic shower propagating longitudinally.

total length of all tracks in a shower is directly proportional to the incident particle energy. The photon conversion length l_γ, the average distance a high energy photon will traverse before converting to an e^+e^- pair, is related to the radiation length by the equation

$$l_\gamma = \frac{9}{7}X_0. \tag{3.8}$$

The lateral spread of an EM shower arises mainly from the multiple scattering of non-radiating electrons and is characterized by the Moliere radius, which is defined as

$$R_m = \frac{21}{M}eV\epsilon_c X_0, \tag{3.9}$$

where ϵ_c is the critical energy.

Why liquid argon and how it works ?

Liquid argon has the following charateristics as an active material:

- liquid argon is very dense (1.4 g/cm^3),
- it has an ionization potential of 23.6 eV that allows the production of a great number of ion pairs,
- it has relatively high electron mobility and does not capture electrons,
- it is easy to obtain, purify and relatively cheap (compare to liquid krypton or liquid xenon),
- it is radiation hard, which is important in the LHC environment.

The Argon is ionized by the charged particles produced in the absorption process of the primary particles. An electric field is applied and the drifting electrons induce a current on the electrode structure. The total induced current is proportional to the energy of the incoming particle. The current is amplified and digitized afterwards. A schematic view of a Liquid Argon (LAr) ionization chamber is shown in figure 3.10.

The ATLAS electromagnetic liquid Argon calorimeter is divided into a barrel part $|\eta| < 1.475$ and two end-caps $1.375 < |\eta| < 3.2$ [58]. It is a lead-liquid Argon sampling calorimeter, highly granular and using accordion-shaped kapton electrodes (see figure 3.11). In the pseudo-rapidity range $|\eta| < 1.8$ it is preceded by a presampler detector, installed immediately behind the cryostat cold wall, and used to correct for the energy lost in the material (inner detector, cryostats, coils, etc.) in front of the calorimeter. A summary of the sampling granularity and coverage can be seen in table 3.2. The first sampling is $6X_0$, which is also known as the "pre-shower detector". It enhances particle identification and provides a high precision η measurement. The second layer, main shower layer of $16X_0$ in thickness, determines the particle energy. The back layer varies from $2X_0$ to $12X_0$ and is normally used for very high energetic

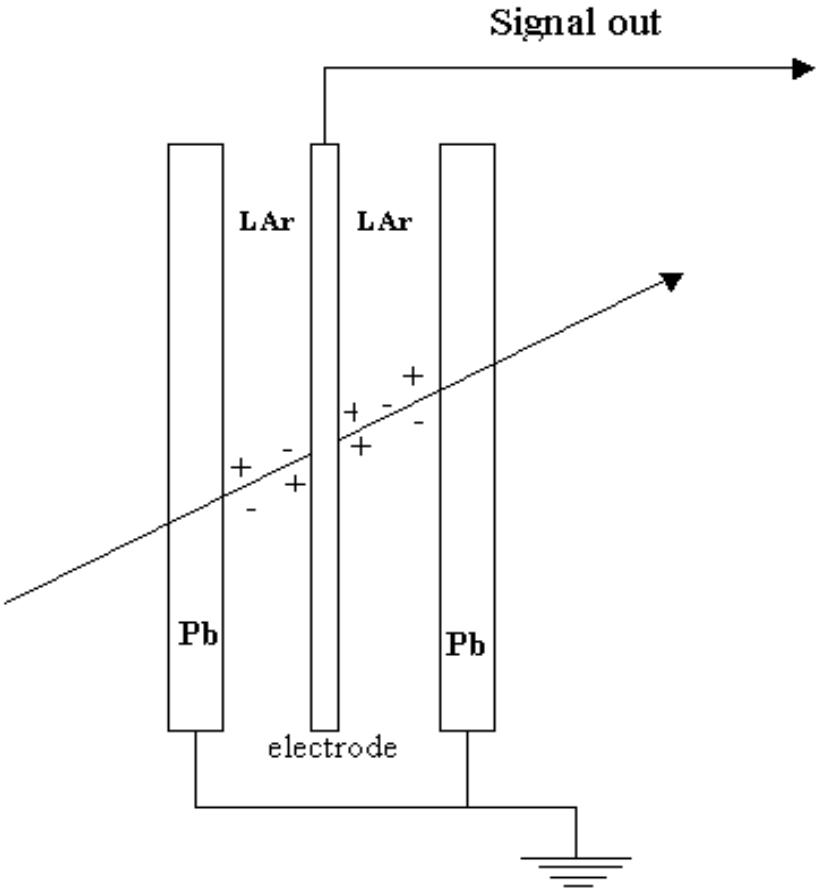

Figure 3.10: Schematic view of a liquid Argon ionization chamber.

particles or "jets". Overall the electromagnetic calorimeter has a thickness of at least $24X_0$ in the barrel and $26X_0$ in the end-cap region [54].

3.2.6 Hadronic calorimeter

The hadronic calorimeter is always positioned behind the electromagnetic one, since the hadrons are so much more massive than electrons or electromagnetic particles and interact with nuclei through the strong interaction. Most practical calorimeters are combined electromagnetic and hadronic detectors. Because the nuclear interaction length is so much longer than the radiation

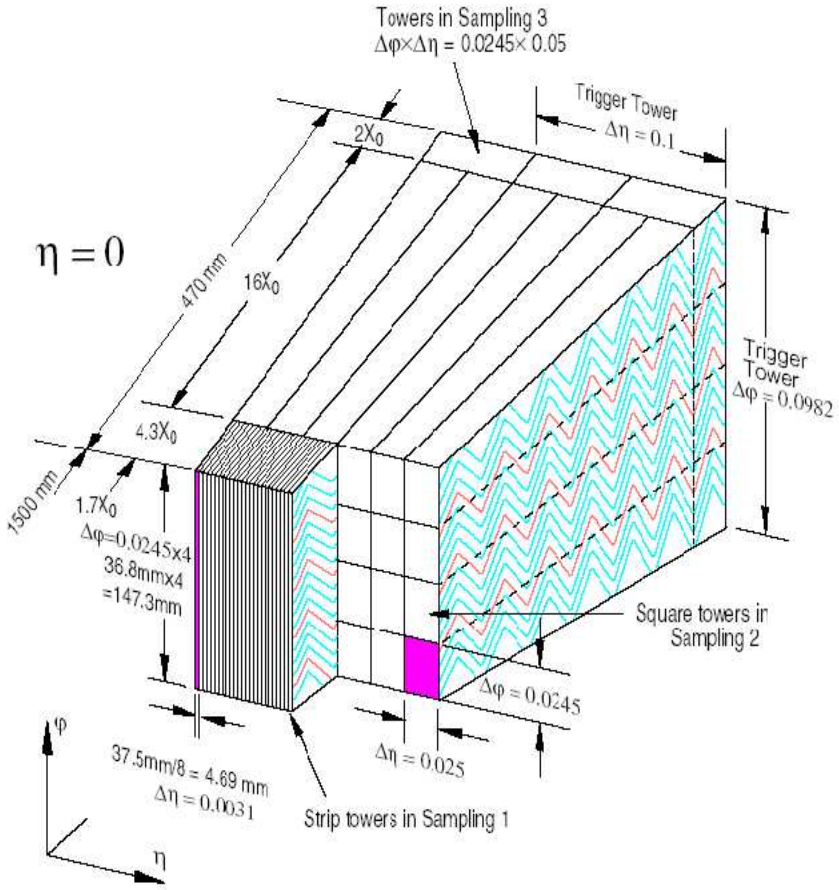

Figure 3.11: ATLAS electromagnetic calorimeter showing the sampling and accordion structure [56].

length, most hadrons pass through the electromagnetic front compartment and interact in the hadronic part and make hadronic shower there.

The ATLAS hadronic calorimeter covers the range $|\eta| < 4.9$ and is made from three different technologies, depending on the varying requirements and the radiation environment across the detector. The hadronic barrel calorimeter also known as the hadronic tile calorimeter has the central barrel and two identical extended barrel sections, which covers $|\eta| <1.7$. The LAr Hadronic End-cap Calorimeter (HEC) and the LAr Forward Calorimeter (FCAL) use liquid argon as an active material due to the high radiation environment. The HEC consists of two independent wheels covering a range $1.5 < |\eta| < 3.2$ and

Table 3.2: Rapidity coverage, granularity and longitudinal segmentation of the ATLAS electromagnetic calorimeter [59].

EM CALORIMETER	**Barrel**	**End-cap**	
Coverage	$\|\eta\| < 1.475$	$1.375 < \|\eta\| < 3.2$	
Longitudinal segmentation	3 samplings	3 samplings	$1.5 < \|\eta\| < 2.5$
		2 samplings	$1.375 < \|\eta\| < 1.5$
			$2.5 < \|\eta\| < 3.2$
Granularity ($\triangle\eta \times \triangle\phi$)			
Sampling 1	0.003×0.1	0.025×0.1	$1.375 < \|\eta\| < 1.5$
		0.003×0.1	$1.5 < \|\eta\| < 1.8$
		0.004×0.1	$1.8 < \|\eta\| < 2.0$
		0.006×0.1	$2.0 < \|\eta\| < 2.5$
		0.1×0.1	$2.5 < \|\eta\| < 3.2$
Sampling 2	0.025×0.025	0.025×0.025	$1.375 < \|\eta\| < 2.5$
		0.1×0.1	$2.5 < \|\eta\| < 3.2$
Sampling 3	0.05×0.025	0.05×0.025	$1.5 < \|\eta\| < 2.5$
PRESAMPLER	**Barrel**	**End-cap**	
Coverage	$\|\eta\| < 1.52$	$1.5 < \|\eta\| < 1.8$	
Longitudinal segmentation	1 sampling	1 sampling	
Granularity ($\triangle\eta \times \triangle\phi$)	0.025×0.1	0.025×0.1	

uses copper absorber plates. The FCAL is made from three sections covering the range $3.1 < |\eta| < 4.9$, with the first section using copper absorber and the other two using tungsten. The main purpose of the hadronic calorimeter is to identify jets and measure their energies and directions, to measure the total missing transverse energy and to enhance the particle identification of the EM calorimeter by measuring quantities such as leakage, isolation, etc.. The rapidity coverage and the corresponding granularities can be found in the Table 3.3.

Hadronic shower

A hadronic shower is produced by a high-energy hadron such as a nucleon, pion, etc., interacting with matter. Since, the fields of an atom extend over regions approximately 10,000 times larger in radius (and thus 10^8 times larger

Table 3.3: Rapidity coverage, granularity and longitudinal segmentation of the ATLAS hadronic calorimeter [59].

HADRONIC TILE	**Barrel**	**Extended barrel**	
Coverage	$\|\eta\| < 1.0$	$0.8 < \|\eta\| < 1.7$	
Longitudinal segmentation	3 samplings	3 samplings	
Granularity ($\triangle\eta \times \triangle\phi$)			
Sampling 1 and 2	0.1×0.1	0.1×0.1	
Sampling 3	0.2×0.1	0.2×0.1	
HADRONIC LAr		**End-cap**	
Coverage		$1.5 < \|\eta\| < 3.2$	
Longitudinal segmentation		3 samplings	
Granularity ($\triangle\eta \times \triangle\phi$)		0.1×0.1	$1.5 < \|\eta\| < 2.5$
		0.2×0.2	$2.5 < \|\eta\| < 3.2$
Forward Calorimeter		**End-cap**	
Coverage		$3.1 < \|\eta\| < 4.9$	
Longitudinal segmentation		3 samplings	
Granularity ($\triangle\eta \times \triangle\phi$)		0.2×0.2	

in area) than the nucleus of the atom, electromagnetic showers typically begin a shorter distance into the calorimeter than hadron showers. A hadronic shower can be parametrised by a nuclear interaction length[10], similar to the radiation length for electromagnetic showers. The hadronic calorimeters have a total thickness of 11 interaction lengths (λ) at $|\eta| = 0$. A schematic view of a hadronic shower is shown in figure 3.12.

Due to the relatively frequent generation of π^0s, there is also an electromagnetic component present in hadronic showers since the π^0 decays almost exclusively to two photons. The purely hadronic part of the hadronic shower is also difficult to model because there are many nuclear processes involved in the shower and the total cross-section is coming from the sum of all processes [61], i.e. many different final states are possible in high energy hadronic interactions. About 30% of the incident energy may be lost due to nuclear excitation

[10]The mean free path is the process or the probability that a particle will interact after traversing a distance x in a material: 1 - $e^{-\frac{x}{\lambda}}$.

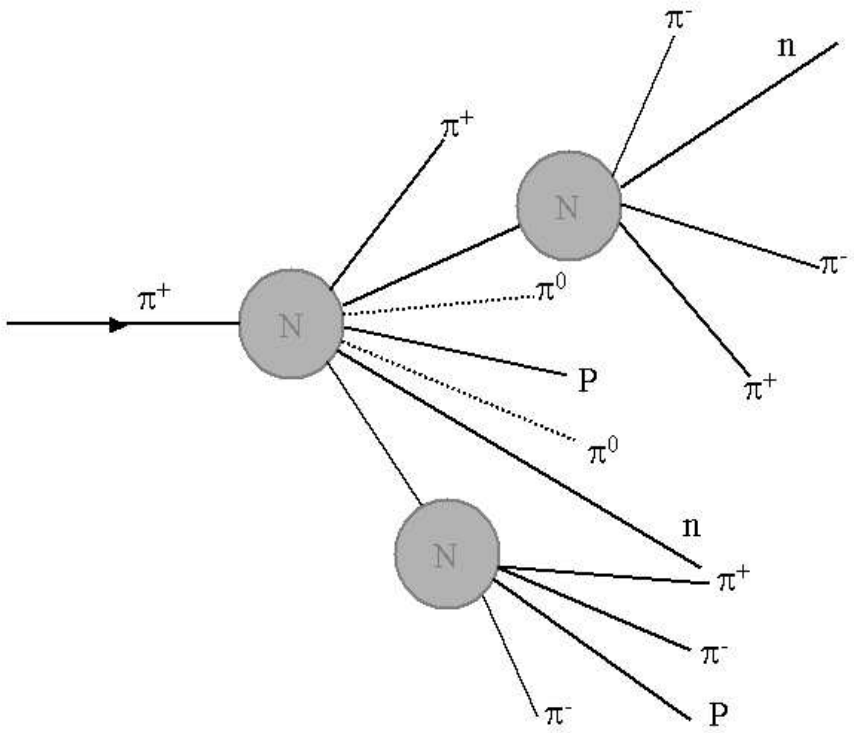

Figure 3.12: A schematic view of a hadronic shower, which is redrawn from [60].

and break-up, spallation or "evaporation" of slow neutrons and protons, and the production of muons and neutrinos which escape from the calorimeter.

Energy resolution

The precision with which the energy of a particle can be measured in a calorimeter is known as its energy resolution. The determination of the energy resolution of a calorimeter depends on the actual energy deposited in the calorimeter (sampling fluctuation), leakage of energy out of the calorimeter, noise from electronics, ion or light collection, etc.. The dominant term in the energy resolution is due to sampling fluctuations, which are poisson in nature, i.e.

$$\frac{\sigma_E}{E} = \frac{a}{\sqrt{E}}, \tag{3.10}$$

where a is a constant and $\frac{1}{\sqrt{E}}$ is coming from the statistical factor (poisson distribution where $\sigma = \sqrt{\mu}$ and μ = NP, N = number of trials and P = probability of success). Therefore the resolution of a calorimeter improves with the particle energy by a factor of $\frac{1}{\sqrt{E}}$. The total energy resolution of a sampling calorimeter is given by the following equation [62]:

$$\frac{\sigma_E}{E} = \frac{a}{\sqrt{E}} \oplus \frac{b}{E} \oplus c, \tag{3.11}$$

where a, b and c are constants, E is energy in GeV and $\oplus$ represents addition in quadrature. The first term is the sampling term coming from the sampling fluctuations described above. The second term is the noise term which is associated with the electronic noise and the noise from the pile-up events, and the third term is referred to as the constant term, which is basically coming from mechanical imperfections, incomplete shower containment and non-compensation. The design goal of the ATLAS calorimeters energy resolutions are as follows: for the electromagnetic calorimeter,

$$\frac{\sigma(E)}{E} = \frac{10\%}{\sqrt{E}} \oplus \frac{0.3\text{GeV}}{E} \oplus 0.7\%, \tag{3.12}$$

for the hadronic calorimeter ($|\eta| < 3.0$),

$$\frac{\sigma(E)}{E} = \frac{50\%}{\sqrt{E}} \oplus 3\% \tag{3.13}$$

and for the hadronic calorimeter ($3.0 < |\eta| < 4.9$),

$$\frac{\sigma(E)}{E} = \frac{100\%}{\sqrt{E}} \oplus 10\%. \tag{3.14}$$

3.2.7 ATLAS muon system

Muons are also charged particles but they are about 200 times heavier than electrons, which makes the behaviour of high-energy muons as they pass

through matter quite different from that of electrons. The force from the electric field is not large enough to cause the muon to change direction significantly and it goes right through the field region without radiating photons to produce pairs or showers.

Muons can penetrate through the calorimeters and reach the outermost part of ATLAS, known as the muon spectrometer. This spectrometer surrounds the calorimeters and measures the trajectories of muons to determine their direction, signof electric charge and momentum. This happens inside a volume of magnetic field produced by superconducting toroid magnets. The muon chambers are made of thousands of metal tubes, each equiped with a central wire and filled with gas. The sensors/tubes are similar to the straws described for the inner detector, but with larger tube diameters. As a muon passes through these tubes, it leaves a trail of electrically charged ions and electrons which drift to the walls and centre of the tube. By measuring the time it takes for these charges to drift from the starting point to the electrodes, it is possible to determine the position of the muon as it passes through.

High-momentum final-state muons are amongst the most promising and robust signatures of physics at the LHC [63]. To measure them, the ATLAS Collaboration has decided to build a high-resolution muon spectrometer as shown in the figure 3.13, with stand-alone triggering and momentum measurement capability over a wide range of transverse momentum, pseudorapidity and azimuthal angle. For the precision measurements of muon tracks in the principle bending direction of the magnetic field, Monitored Drift Tube chambers are used except in the high-flux inner regions of the end-cap, where Cathode Strip Chambers are used. There are separate sets of chambers employed for triggering. In the barrel region there are three stations of Resistive Plate Chambers and in the end-cap three stations of Thin Gap Chambers expressly for the purpose of triggering [60]. A complete description of the ATLAS muon spectrometer can be found elsewhere [63].

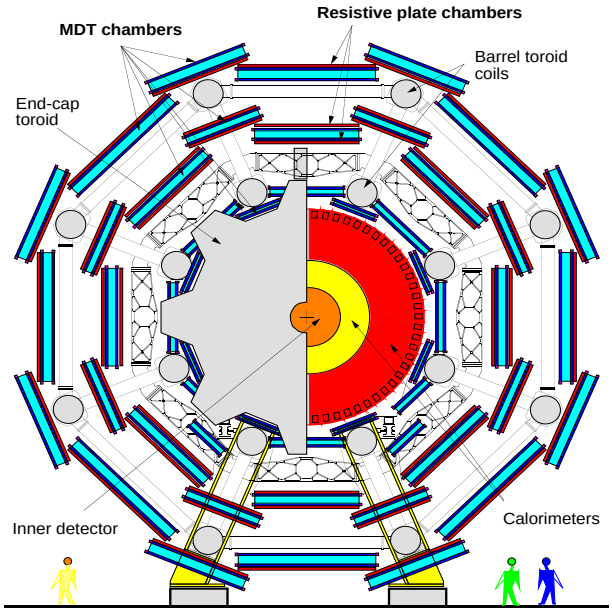

Figure 3.13: Transverse view of the muon spectrometer.

3.2.8 ATLAS trigger system

Much of the ATLAS physics program at high luminosity must be carried out using very inclusive triggers, at least at the earlier selection stages. These include inclusive selections of events containing high-p_T muons, photons, electrons, taus, hadrons and jets, as well as events with very large missing transverse energy.

The ATLAS trigger and data-acquisition system is based on three levels of online event selection, shown in figure 3.14. Each trigger level refines the decisions made at the previous level and, where necessary, applies additional selection criteria. Starting from an initial bunch-crossing rate of 40 MHz (interaction rate is about 10^9 Hz at a luminosity of 10^{34} cm^{-2}s^{-1}), the rate of selected events must be reduced to about 100 Hz for permanent storage. While this requires an overall rejection factor of 10^7 against minimum-bias processes, excellent efficiency must be retained for the possible rare new physics, such as Higgs boson decays. At LVL1 (custom built electronics level), special-purpose

processors act on reduced-granularity data from a subset of the detectors. LVL2 (software based level) uses full-granularity, full-precision data from the detectors, examines only regions of the detector identified by the LVL1 trigger as containing interesting information. At the third trigger level, the event filter, the full event data are used together with some calibration and alignment information to make the final selection of events to be recorded for offline analysis. More details regarding the ATLAS trigger system can be found elsewhere [64, 65].

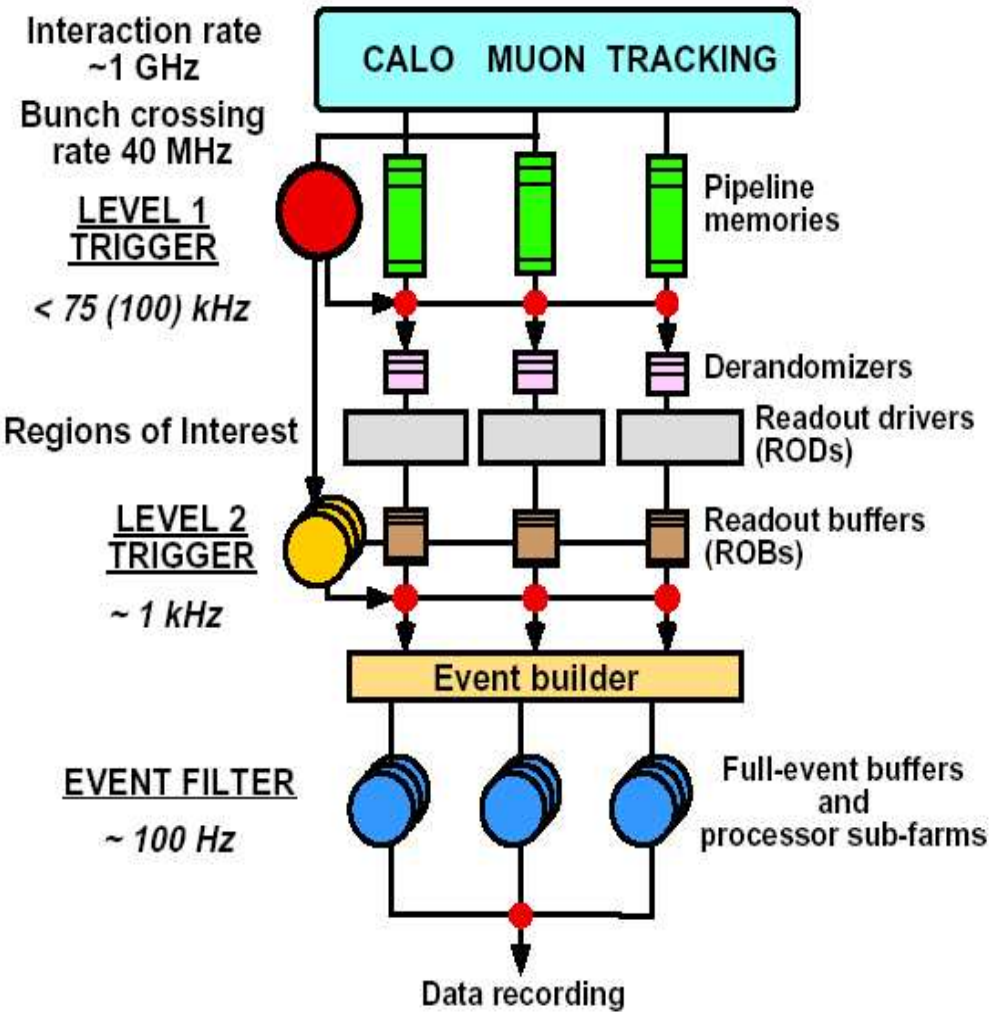

Figure 3.14: Block diagram of the trigger/DAQ system.

3.2.9 ATLAS magnet system

A magnetic field is an essential requirement for bending the collision products and to allow momentum measurements in a collider experiment. For this purpose ATLAS is equipped with a hybrid system of four large superconducting magnets: a Central Solenoid providing a 2 T axial magnetic field used by the central trackers, and a Barrel Toroid and two End-Cap Toroids, which make the tangential magnetic field of about 1 T at the muon detectors. A schematic view of the ATLAS super-conducting magnet system can be seen in figure 3.15 and more details about the magnet system of the ATLAS experiment are available elsewhere [66, 67].

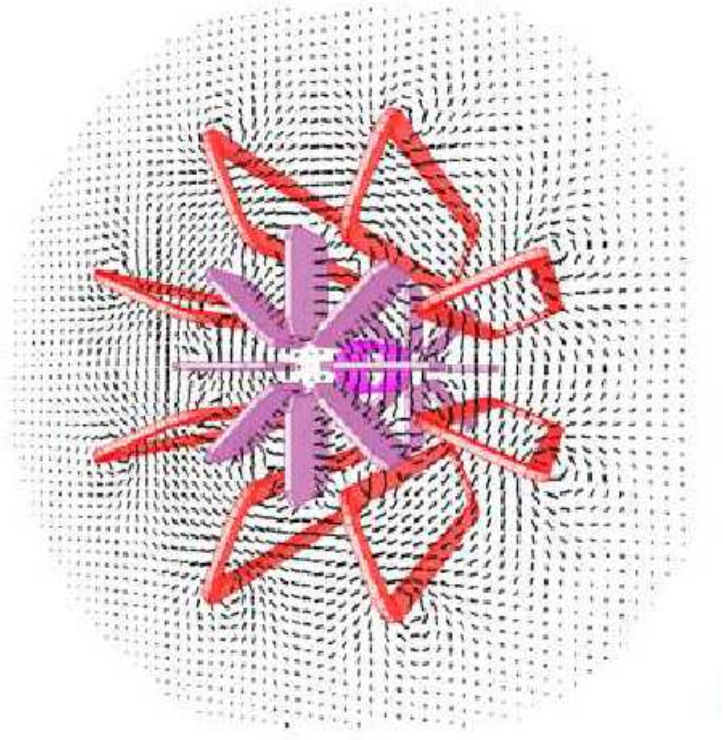

Figure 3.15: A schematic view of ATLAS magnet arrangement.

Chapter 4

Computing and Software

4.1 Introduction

The LHC computing project, called the LHC computing grid, developed at CERN provides the necessary processing power and data storage for the projected 15×10^{15} bytes of annual data from the LHC. The idea behind grid computing is to avoid processing the data locally by distributing the processing over a powerful network of computers and share the processing time between many computer clusters in different countries. In order to process millions of events, the ATLAS detector has a sophisticated

- trigger system [68], which selects interesting events out of millions of others,
- data acquisition system [69], which channels the data from the detector to the storage and
- offline computing system [70], which is responsible for reconstructing millions of events recorded per year.

The ATLAS computing model uses the grid paradigm and a high degree of decentralization and sharing of computing resources. The high level of computing resources required means that off-site facilities will be vital to the operation of the ATLAS experiment. The ATLAS computer model hierarchy

is based on a tier system, e.g. the Tier-0 located at CERN is responsible for archiving and distributing of primary RAW data received from the Event Filter. The RAW data archived at CERN are then copied (along with the primary processed data) to the Tier-1 facilities around the world. These facilities archive the RAW data, provide reprocessing capacity and allow scheduled analysis of the processed data by physics analysis groups. Derived datasets produced by the physics groups are copied to the Tier-2 facilities for further analysis.

Different types of data formats are used in ATLAS. Table 4.1 shows the assumed data sizes for various formats and the corresponding processing times. Different data formats are also explained in the following paragraphs.

Table 4.1: Assumed data sizes for various data formats, the corresponding processing times and related operational parameters [70].

Item	Value	Unit
Raw data size	1.6	MB
ESD size	0.5	MB
AOD size	100	kB
TAG size	1	kB
Simulated data size	2.0	MB
Simulated ESD size	0.5	MB
Times/Reconstruction	15	kSI2k-sec
Times/Simulation	100	kSI2k-sec
Times/Analysis	0.5	kSI2k-sec
Event rate after EF	200	Hz
Event statistics	10^7	events/day
Event statistics (from 2008 onward)	2×10^9	events/year

The Event Summary Data (ESD) contains the detailed output of the detector reconstruction and is produced from the raw data. It will contain sufficient information to allow particle identification, track re-fitting, jet calibration, etc., thus allowing for the rapid tuning of reconstruction algorithms and calibrations. The size of the ESD is intermediate in between RAW (described above)

and AOD (described below). The ESD has an object-oriented representation, and is stored in POOL ROOT files. ESD objects are normally stored in so-called "Containers".

The Analysis Object Data (AOD) is a summary of the reconstructed events, and contains sufficient information for common physics analysis. The AOD can be produced from the ESD and thus makes it unnecessary in general to navigate back and process the raw data, adding significant time benefits. The AOD is a reduced event representation in comparison with the ESD. The AOD also has an object-oriented representation, and is stored in POOL ROOT files (can be directly read into the official ATLAS offline software Athena), in which objects are also stored in containers. The AOD format is used in this thesis, which is processed using the ATLAS software framework, Athena.

4.2 Athena framework

The main goal of the ATLAS offline software is to process the events delivered by the ATLAS trigger and data acquisition system. The Athena framework [72] is an enhanced version of the Gaudi framework [73] developed for the LHCb experiment [74]. It is an object oriented C++ and python based framework that is currently being developed by the ATLAS collaboration. The Athena framework is now a common ATLAS-LHCb project and is in use by several other experiments, e.g. GLAST (renamed as Fermi Gamma-ray Space Telescope), HARP, etc.. The architectural model of the Athena framework is shown in figure 4.1. The main responsibilities of the Athena framework is to define an interface for each component, load shared libraries, loop over events, I/O mechanisms and job configurations, etc.. The application manager, one of the main components in the Athena framework, is responsible for managing and coordinating the activities of all other components within the application by creating the services, top level algorithms and steering the event loop. Services include JobOptionSvc, MessageSvc, EventDataSvc, Detector-

DataSvc, etc.. Algorithm in figure 4.1 is the user application building block, which is controlled by the framework. The user algorithms produce results as output for the corresponding inputs in a sequence initialize() → execute() → beginRun() → endRun() → finalize().

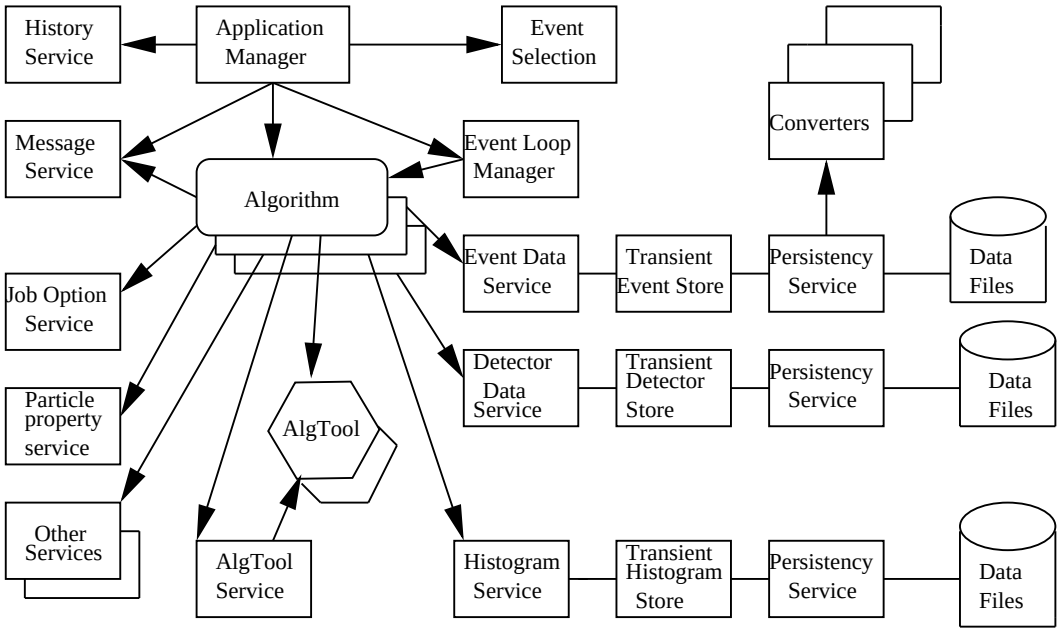

Figure 4.1: Athena component model. Redrawn from [70].

The Athena framework provides basic services and works as a skeleton into which developers can plug their code. The plugged code can be used to generate simulated events, and to reconstruct both simulated and real events. The steps to study simulated events are event generation, detector simulation, detector response, reconstruction, physics analysis and event display as shown in figure 4.2.

Event generation is the first step in the Athena framework where one can produce the desired events via specific event generator(s) e.g. the MC@NLO generator can be used to produce top quark pairs. There are other event generators, e.g. HERWIG, JIMMY, ALPGEN, PYTHIA, AcerMC, etc.. In these cases one can specify the physics process(es), provide the kinematics of particles and produce output in the POOL persistent framework.

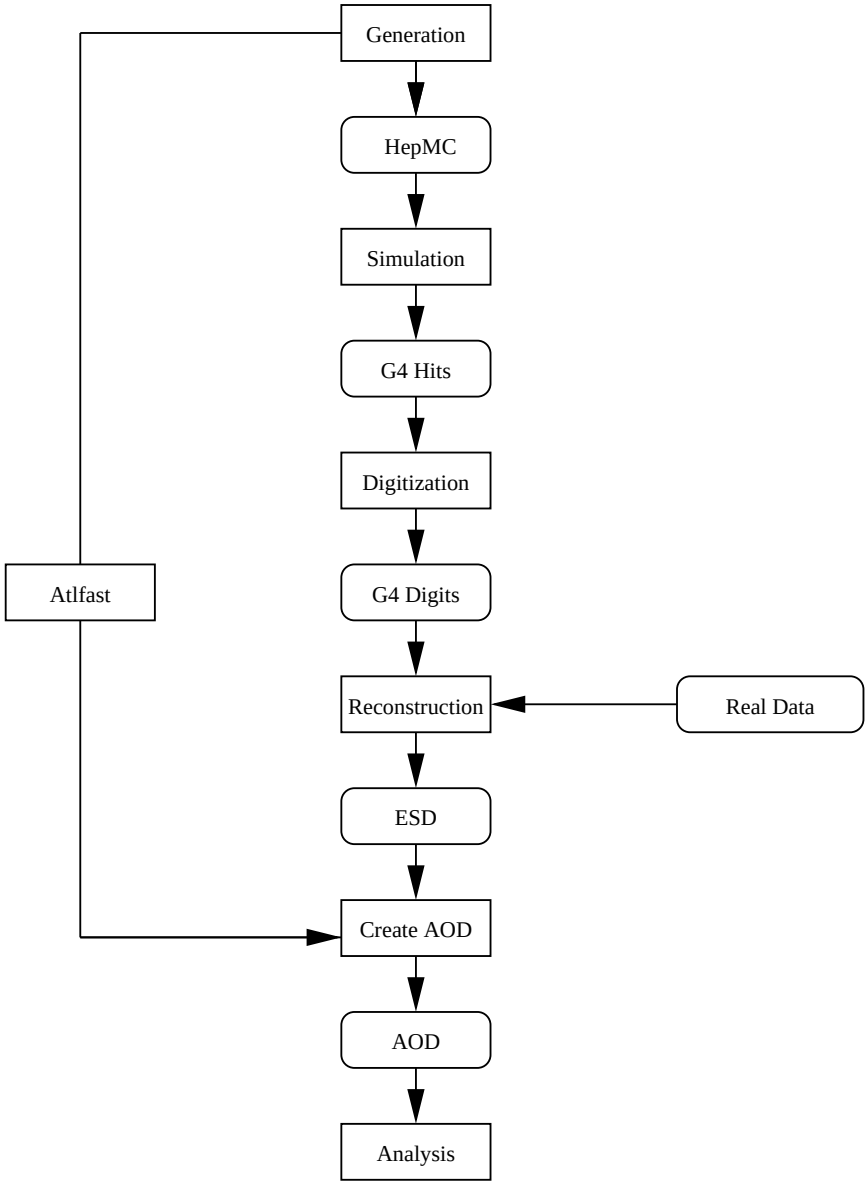

Figure 4.2: Schematic representation of data-processing stages in the Athena framework.

Simulation is the process whereby generated events are passed through a GEANT4 simulation of the ATLAS detector to produce GEANT4 hits, i.e. a record of where each particle traversed the detector and how much energy was deposited. The G4HITS produced by the GEANT4 simulation are the response of the detector to produce digits, such as times and voltages, as produced in the raw data from the real detector. Reconstruction from Raw Data Objects (RDOs) is an important step for further physics analysis. Particle tracks, energy deposits and other kinematic information are reconstructed from RDOs and can be saved as ESD and/or AOD.

4.3 Physics analysis

The ATLAS software framework is continually updated to allow developers to insert new code and fix bugs. Periodically all the software is released and given a release number. Users can create their own analysis algorithm by checking out the corresponding packages. Each package contains different directories, e.g. the LArCellRec package contains:

- all the header files, which includes the class definition of objects,
- source code in which the user can implement their classes and routines to produce results,
- a configuration Management Tool that manages the relationship between the packages, compiles and builds the packages, sets up runtime environment, etc.,
- job options, data files, etc.,
- a text file containing change history.

Chapter 5

Analysis and Results

5.1 Jet energy scale

Many physics measurements depend on accurate knowledge of jet energies. The jets are the resulting form of the fragmentation of quarks and gluons in the hard scattering process. A precise knowledge of the absolute jet energy scale (JES) is one of the main issues at hadron colliders. As most of the studied processes will contain one or more jets in the final state, the more accurate the energy of the jet is known (i.e. the less biased this measurement is), the more precisely fundamental parameters of the SM can be measured. Indeed, the measurement of the top quark mass is a direct application of the above statement. A precise knowledge of this observable allows a consistency check of the SM and increases constraints on SM parameters (e.g. the mass of the Higgs boson). The *in situ* method we are describing in this thesis aims at calibrating the light jet energy scale at the 1% level [75].

The measurement of the top quark mass with a precision of 1 GeV/c^2 will be one of the early and main goals of the LHC experiments [76]. The top quark mass is currently known to 1.9 GeV/c^2 from the combined study of CDF and D0 Run-II and Run-I [37,77] at the Tevatron. The miscalibration of jet energies is one of the main sources of systematic error in the measurement of the top quark mass. Indeed, a 1% error on the jet energy translates into a 0.9 GeV/c^2 error on the top quark mass: 0.2 GeV/c^2 coming from the light JES

and 0.7 GeV/c^2 from the b-quark JES. The goal of measuring the top quark mass with a precision of 1 GeV/c^2 thus puts the limit on the miscalibration at 1% or better [80]. This precision is required of the top quark mass to improve the consistency of the SM and for further new physics searches.

The measurement of the W mass via reconstruction of $W \to jj$ (two light quark jets) relies on a precise knowledge of the energy calibration for two light jets, which can then make a significant contribution to the measured top quark mass via $t \to jjb$ (two light quark jets plus a b-jet). Determining the absolute jet energy scale at the LHC will be a rather complex issue because of its dependence on a variety of uncertainties, e.g. physics, detector and reconstruction algorithm effects. A schematic view of a calorimeter jet from partons is shown in figure 5.1.

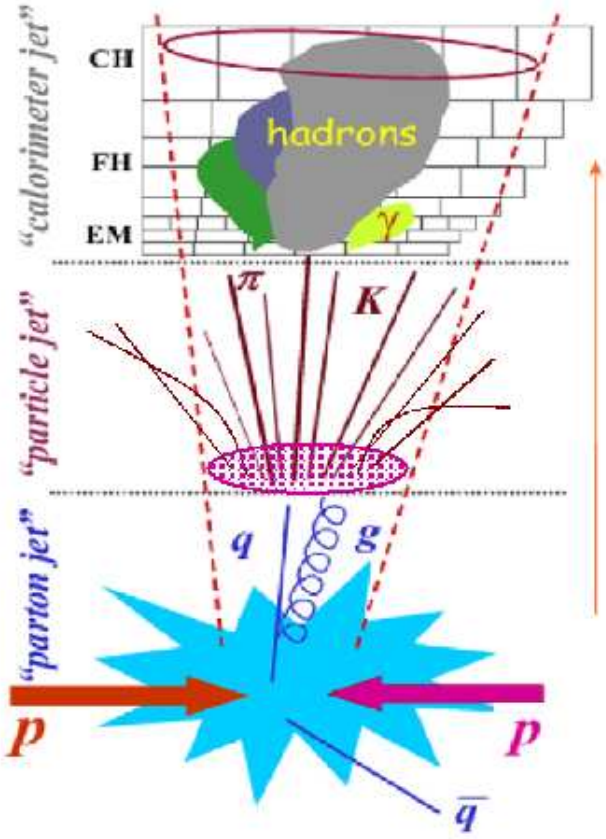

Figure 5.1: Calorimeter jet from a parton interaction [78].

Physics effects leading to uncertainties in the jet energy determination includes initial state radiation (ISR), final state radiation (FSR), hadronization, underlying events, etc.. Gluon radiation from the initial particles before interaction is referred to as ISR, whereas the gluon radiation before hadronization but after the scatter is called FSR (see figure 5.2). Forming colourless hadrons from coloured partons is named hadronization and the energy from the interactions of spectator partons is labeled as an underlying event (UE) (see figure 5.2).

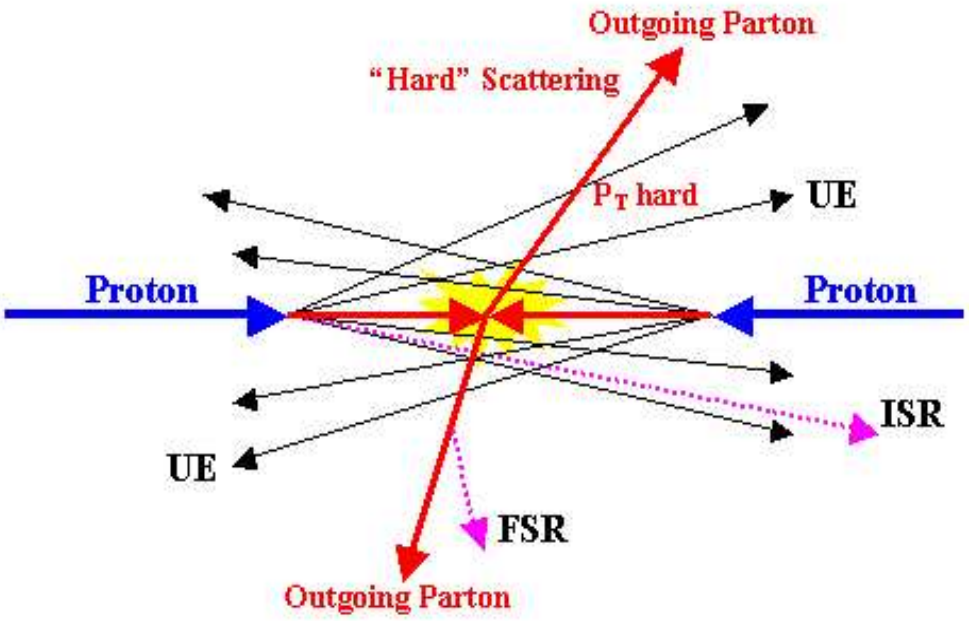

Figure 5.2: A schematic view of a hard scattering event from a proton-proton collision [79].

Being a sampling device, the ATLAS calorimeter response is different for different particles (either electromagnetic or hadronic) entering into it. Due to the geometry, the central and forward calorimeter responses are also different. There are some poorly instrumented regions or "cracks" of the calorimeter due to the gap between the barrel and endcap, where the calorimeter response is

less, e.g. figure 5.3 shows the number of electrons with respect to the pseudo-rapidity.

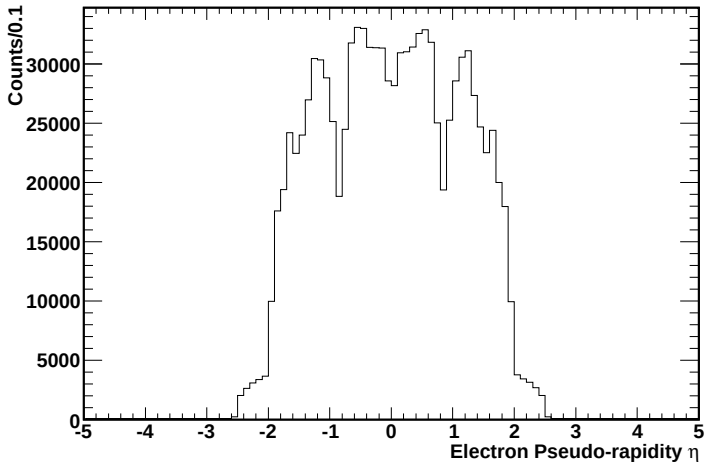

Figure 5.3: Electron pseudo-rapidity distribution without any selection.

Reconstruction algorithms are used to identify jet clusters and calibrate the jet energy produced by the interaction of incoming particles (hadrons) with the detector materials. Different jet finder algorithms are used in ATLAS for reconstruction purposes, e.g. cone and K_T algorithms. More details on jet reconstruction algorithms will be discussed in section 5.4. During the reconstruction, jet overlap may also cause systematic uncertainties in the JES. Out-of-Cone (OOC) corrections correct the particle-level energy for leakage of radiation outside the clustering cone used for the jet definition taking the jet energy back to parent parton energy.

All of the effects discussed above have to be understood and corrected at the level of a fraction of a percent in terms of systematic uncertainties, as required for the precision measurements of the SM parameters. This correction can be done via calibration methods. The *in situ* calibration method is a good way to determine the absolute energy scale of jets. The key idea of this calibration method is to use events recorded during data taking to compute calibration weights of jet energies. Several methods have been developed.

5.1.1 Calibration methods

The E/p calibration method [81,82] works by inter-calibrating the calorimeters with the inner detectors of the ATLAS detector, i.e. the precise measurement of the momentum p of charged hadrons in the inner detector compared to their energy E measured in the calorimeter will provide a comparison between the absolute scales of the two detector systems. The ratio of E/p should be close to unity. Single charged isolated hadrons are required to determine the momentum of tracks in the ATLAS inner detector in this method. For example, τ decays to a single charged isolated hadron in $\mathrm{Z} \rightarrow \tau\tau$ events. We can not use this method in this thesis because we are interested in jets.

The p_T balance method is based on p_T balance between a jet and another particle produced back-to-back with it [83], where the other particle can be an electron, a muon or a photon. For example, in the production of the Z + jet process, where the Z decays to an electron or muon pair and is produced back-to-back with a jet. The lepton pairs can be used to accurately reconstruct the Z four momenta. This method is especially useful for b-jet energy calibration. We will not use this method in this thesis since we are interested in the light jet energy scale.

The resonance decay method uses a resonance decaying into a jet pair. For example, we can calibrate jet energies using the W resonance, which decays into two light jets, e.g. [3, 84, 85]. Calibration weights can be computed by requiring that the reconstructed di-jet invariant mass has to be equal to the W mass from the particle data group (PDG) [86]. We will use this method in this thesis.

5.2 Data samples

Since the ATLAS experiment has just started and real data are not yet available, we used Monte Carlo simulated data samples in this thesis. The Monte Carlo samples that have been considered for this thesis, are listed in

table 5.1 and described in sections 5.2.1, 5.2.2 and 5.2.3. All the number of events have been normalized using weights to the luminosity of 100 pb^{-1}, which is producted to be obtained the early stage (10^{32} $cm^{-2}s^{-1}$) of ATLAS running. We found some data files missing and/or corrupted and therefore the number of events used in this analysis are not exactly the same (see table 5.3). Both the samples of $t\bar{t}$ signal and SM background events were generated and simulated within the ATLAS Athena framework. A detailed GEANT4 simulation of the detector was used. In this thesis, we used the ATLAS Computing System Commissioning (CSC) data. The simulated events were then processed with version 12.0.6 of the ATLAS detector simulation and reconstruction code. AODs were used for further analysis. More details about the ATLAS data structures and software were described in chapter 4.

5.2.1 Simulation of $t\bar{t}$ signal events

Top-quark pair production (CSC data set 5200) has been simulated using the next-to-leading order (NLO) generator MC@NLO 3.1 [88] with a fixed top quark mass of 175 GeV/c^2. The hard process of $t\bar{t}$ production is calculated at the NLO, which means the diagrams that produce one additional gluon in the final state are included at the matrix element level. The parton density functions CTEQ6M [89] are used. The produced matrix elements are processed by HERWIG [90] to simulate fragmentation and hadronization in conjunction with the underlying event generator JIMMY [91]. Data are archived in sample 5200 (single and double leptonic events). There are no cuts applied at the generation level and no pile-up included in this simulation. Event weights have been ignored in this analysis.

5.2.2 Simulation of background from $W + n$ jet events

Background events coming from $W + n$ partons are generated with ALPGEN [92]. ALPGEN is a LO matrix element generator for multi-parton processes in hadronic collisions, which specifically takes care of the overlap be-

Table 5.1: The MC generator, cross-section and number of generated events for each sample, where st means single top [87].

sample ID	**process**	**generator**	**# events**	σ **(pb)**
5200	$t\bar{t} \to bWbW \to$ $bqqb\ell\nu, b\ell\nu b\ell\nu$	MC@NLO	592300	461.0
8240	$W \to e\nu + 2j$	ALPGEN	21950	214.0
8241	$W \to e\nu + 3j$	ALPGEN	11250	123.9
8242	$W \to e\nu + 4j$	ALPGEN	6000	53.6
8243	$W \to e\nu + 5j$	ALPGEN	4950	22.3
8244	$W \to \mu\nu + 2j$	ALPGEN	3250	16.3
8245	$W \to \mu\nu + 3j$	ALPGEN	11300	64.7
8246	$W \to \mu\nu + 4j$	ALPGEN	3200	36.0
8247	$W \to \mu\nu + 5j$	ALPGEN	4500	20.2
8248	$W \to \tau\nu + 2j$	ALPGEN	20600	87.7
8249	$W \to \tau\nu + 3j$	ALPGEN	13000	87.1
8250	$W \to \tau\nu + 4j$	ALPGEN	5000	45.9
8251	$W \to \tau\nu + 4j$	ALPGEN	550	20.8
5500	st (Wt)	AcerMC	48350	26.7
5501	st (s-chan)	AcerMC	48300	3.3
5502	st (t-chan)	AcerMC	43450	81.3
5030	QCD J1 (17 - 35 GeV p_T cut)	HERWIG	7250	2.38×10^9
5011	QCD J2 (35 - 70 GeV p_T cut)	PYTHIA	4750	9.33×10^7
5032	QCD J3 (70 - 140 GeV p_T cut)	HERWIG	50000	5.88×10^6
5013	QCD J4 (140 - 280 GeV p_T cut)	PYTHIA	66750	3.08×10^5
5014	QCD J5 (280 - 560 GeV p_T cut)	PYTHIA	87550	1.25×10^4
5015	QCD J6 (560 - 1120 GeV p_T cut)	PYTHIA	50000	360

tween the multi-parton matrix element and parton shower. ALPGEN performs at LO in QCD and EW interactions, which calculate the exact matrix elements for a large set of parton-level processes. Parton level events are generated providing full information on their colour and flavour structure, enabling the evolution of the partons into fully hadronized final states. Since the W + n partons use a three jet filter with $p_T > 20$ GeV/c cut, an extra jet is needed to pass the filter for W + 2 jets and electrons often fake jets unlike muons which do not. Therefore, the efficiency for the electron plus two parton sample is much higher than the muon sample, though this difference is much smaller for the three jet samples because they contain enough real jets to pass the filter.

5.2.3 Simulation of background from single top events

The three processes of electroweak top production have been simulated using the AcerMC Monte Carlo [93] in conjunction with PYTHIA [94]. The AcerMC event generator is dedicated for the generation of the SM background processes in pp collisions at the LHC. Three samples for Wt (5500), s-channel (5501) and t-channel (5502) have been produced. All three channels were generated with W bosons forced to decay leptonically. In the case of Wt, either the associated W or the W from top decay is forced to decay leptonically and no dilepton events are included.

5.2.4 QCD dijet processes

QCD dijet events do not have the same final state as $t\bar{t}$ events at the parton level, but may still do so on the reconstruction level for a small fraction of the events. Since the QCD dijet cross-section is three orders of magnitude or more larger [95] than that of $t\bar{t}$ production cross-section, it may have a non-negligible background. A study using the QCD dijets samples J1, J2, J3, J4, J5 and J6 has been done. These samples are generated by the HERWIG (J1 and J3) and PYTHIA (J2, J4, J5 and J6) event generators for CSC analysis. To generate

a $t\bar{t}$ like final state missing energy and a hard lepton transverse momentum are considered.

5.3 Event selection

Event reconstruction is the process of interpreting the electronic signals produced by the original particles that passed through the detector to determine their momenta, directions, and the primary vertex of the event. Thus the initial physical process that occurred at the interaction point of the particle accelerator, whose study is the ultimate goal of the experiment, can be determined. Because of the high event rate and the small signal to background (S/B) ratio at the LHC, event selection is a very important and complex issue. If an event is selected, full analysis is launched. In analysis, we often use the distance ΔR between objects, which is defined in $\eta - \phi$ space as $(\Delta R)^2 = (\Delta\eta)^2 + (\Delta\phi)^2$. All cones are defined in $\eta - \phi$ space.

Based on the ATLAS Physics Coordination and the top quark working group recommendation the events are selected in the following ways:

- One lepton (electron or muon) with $p_T > 20$ GeV/c,
- Missing transverse energy $E_T^{miss} > 20$ GeV,
- At least 4 jets with $p_T > 40$ GeV/c each.

A $t\bar{t}$ signal produces few leptons with p_T lower than 20 GeV/c (see figure 5.6). Detail definitions and selections of electrons, muons, missing transverse energy and jets will be discussed in sections 5.3.1, 5.3.2 and 5.3.3, respectively. A precise alignment of the trackers (inner detectors) are needed for an efficient b-tagging, which will be reached only after a few months of ATLAS data taking. Therefore no b-tagging studies are included in this thesis.

5.3.1 Missing transverse energy

Missing transverse energy is defined as $E_T^{miss} = \sqrt{E_x^{miss} + E_y^{miss}}$, where E_x^{miss} and E_y^{miss} are the missing energy components in the x and y directions measured in the calorimeter minus the energy in x and y directions of the reconstructed muons since the high-p_T muons only deposit a small portion of their energy in the calorimeter. The distribution of E_T^{miss} for $t\bar{t}$, single top, W + jets ($W \rightarrow e\nu$) and QCD dijets samples (J5 and J6) is shown in figures 5.4a, 5.4b, 5.4c and 5.4d, respectively. Only J5 and J6 are used for QCD backgrounds.

For the semileptonic topology in $t\bar{t}$ events, the missing transverse energy is required to be greater than 20 GeV in order to reduce the QCD backgrounds. Figure 5.5 shows the final transverse missing energy for the signal and backgrounds with $E_T^{miss} > 20$ GeV. The selection efficiencies are reported in table 5.2 for both signal and backgrounds with the selection cuts.

Table 5.2: Selection efficiencies for the missing transverse energies greater than 20 GeV.

sample ID	**# events**	**# events with** $E_T^{miss} > 20$ GeV	**Efficiencies (%)**
$t\bar{t}$	161883	148065	91 ± 0.46
W + Jets	46317	41586	89 ± 0.79
single top	12155	10850	89 ± 0.26
QCD	364	297	81 ± 0.59

From figures 5.4 and 5.5, we see that the missing transverse energy is not a useful variable to reject W + jets and single top events though it is a very strong discriminant variable for non-W background such as QCD dijets events. The normalization scale factors with respect to the luminosity $L = 100$ pb^{-1} are reported in the table 5.3. The number of events are taken from the missing E_T distributions of all samples (signals and backgrounds) used in this analysis.

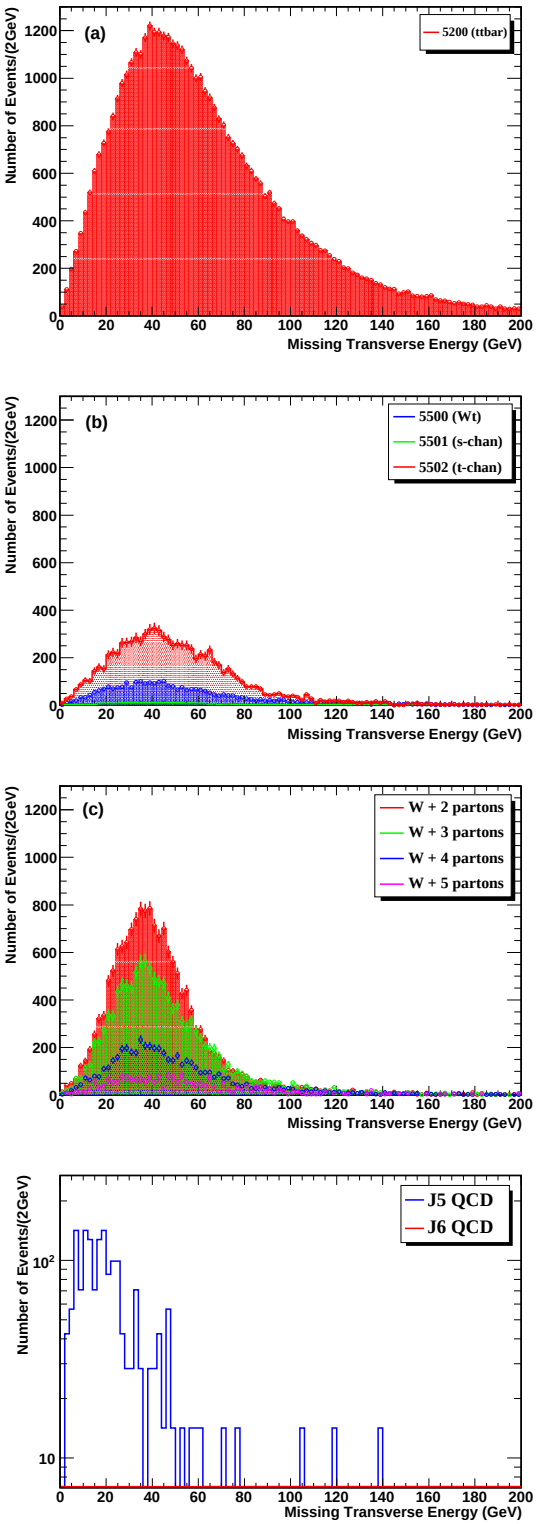

Figure 5.4: Missing transverse energy distribution of a) $t\bar{t}$ b) single top c) W + jets and d) QCD dijet samples.

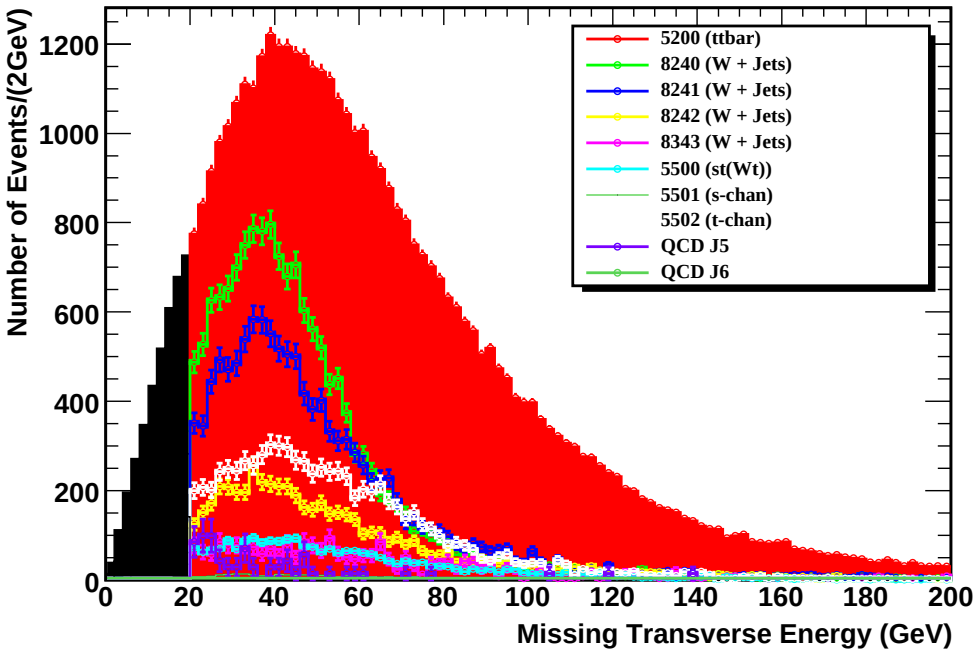

Figure 5.5: Missing transverse energy distribution of $t\bar{t}$, single top, W + jets and QCD dijet samples. Black region is $p_T < 20$ GeV/c.

Table 5.3: Normalized scale factors with respect to the luminosity L = 100 pb^{-1} of all samples.

sample ID	**# events after selection cuts**	**scale factor 100 (pb^{-1})**
5200	161883	0.285
8240	18058	1.19
8241	8043	1.56
8242	3958	1.35
8243	575	3.88
8244	0	NA
8245	5354	1.21
8246	8521	0.422
8247	0	NA
8248	629	13.94
8249	466	18.69
8250	270	17.0
8251	451	4.61
5500	4812	0.555
5501	2007	0.16
5502	5336	1.524
QCD J1	0	NA
QCD J2	2	4.66×10^{9}
QCD J3	89	6.6×10^{6}
QCD J4	92	3.3×10^{5}
QCD J5	121	1.03×10^{4}
QCD J6	60	600

5.3.2 Electron selection

Electrons are extracted from the "ElectronCollection" AOD container and reconstructed in the pseudo-rapidity range $0 \leq |\eta| \leq 2.5$. If an electron is found in the problematic calorimeter crack region $1.37 < |\eta| < 1.52$ (where the barrel and end cap meet), the electron is rejected. There are three different types of quality cuts for electron candidates: a cut based on isEM flag, a cut based on likelihood and a cut based on a neural network algorithm. The isEM flag method is used in this analysis. The isEM flag uses both calorimeter and tracking information in addition to transition radiation tracker (TRT) information whereas in the likelihood method no TRT information is included. The flag is a bit field which marks whether the candidate passed or not some quality checks. Electrons passing that check are called good electrons. Three different isEM flags are available in ATLAS release 12.0.6, e.g.

- tight selection: isEM() == 0 (all cut-based variables are within the required windows),
- medium selection: (isEM() & 0x3FF) == 0 (track matching, $\frac{E}{|p|}$ and TRT requirements are not imposed),
- loose selection: (isEM() & 0x7) == 0 (ClusterFirstSampling and none of the tracking-based requirements are imposed).

Medium selection is implemented to identify electrons. To require an isolated electron, one has to require that the energy deposited in the cone around the electron cluster within the radius $\Delta R = 0.2$, to be less than 6 GeV. Based on the above selections and cuts, the electron p_T distribution for semi-leptonic $t\bar{t}$ events is shown in figure 5.6. The efficiency for $p_T > 20$ GeV/c with respect to $p_T > 10$ GeV/c is 80%.

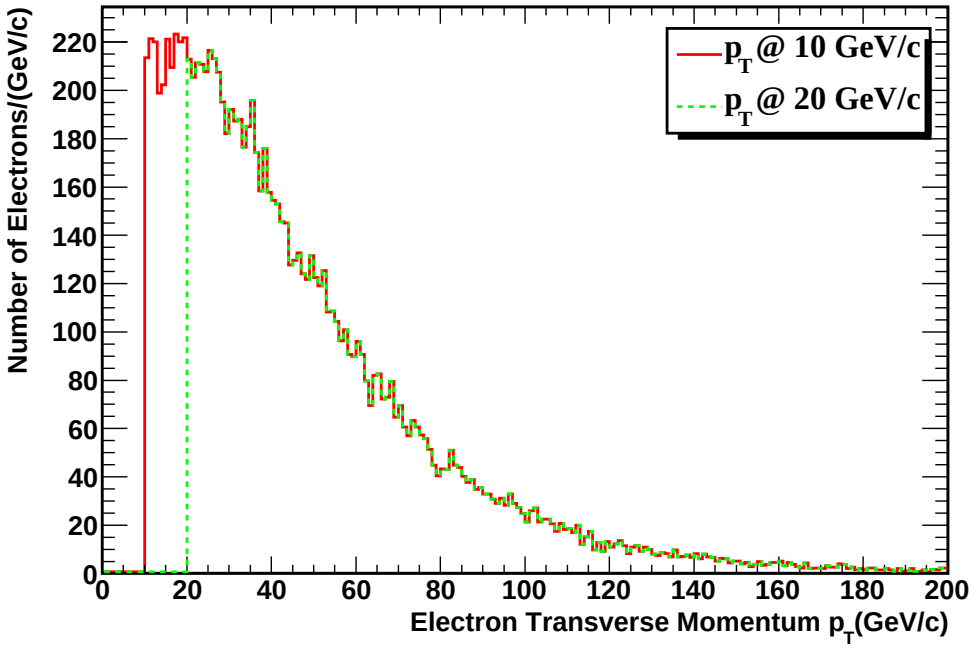

Figure 5.6: Transverse momentum distribution of electrons in $t\bar{t}$ events.

Electron triggers in $t\bar{t}$ events

Since the purpose of this thesis is to study the jet energy scale, and electrons often fake jets, a trigger study has been done for electrons with the above mentioned offline selections. The lowest unprescaled trigger threshold depends on the luminosity and for a luminosity of 10^{33} cm^{-2} s^{-1} the e25i trigger is the unprescaled trigger with the lowest p_T threshold that we used in this analysis. The dependence of a trigger on the actual p_T cut is investigated by means of turn-on curves, which show the fraction of objects passing a certain trigger as a function of the reconstructed p_T of that object. True p_T information can also be used. In order to do this, a matching procedure is applied between trigger candidate objects and the reconstructed objects. The distance between these objects is represented by (ΔR), and a match is assumed for the two objects with the smallest ΔR value, provided that this ΔR is less than a certain value, which is 0.2 [96]. The turn-on curve as a function of the offline p_T cut for the

electron triggers is shown in figure 5.7. This figure tells us which fraction of the events we consider for analysis is accepted by the trigger. Table 5.4 shows the efficiencies of the e25i trigger. After passing the triggers and offline selections, the electron transverse momentum in $t\bar{t}$ events is plotted in figure 5.8. We use this reconstructed electron container for our further analysis.

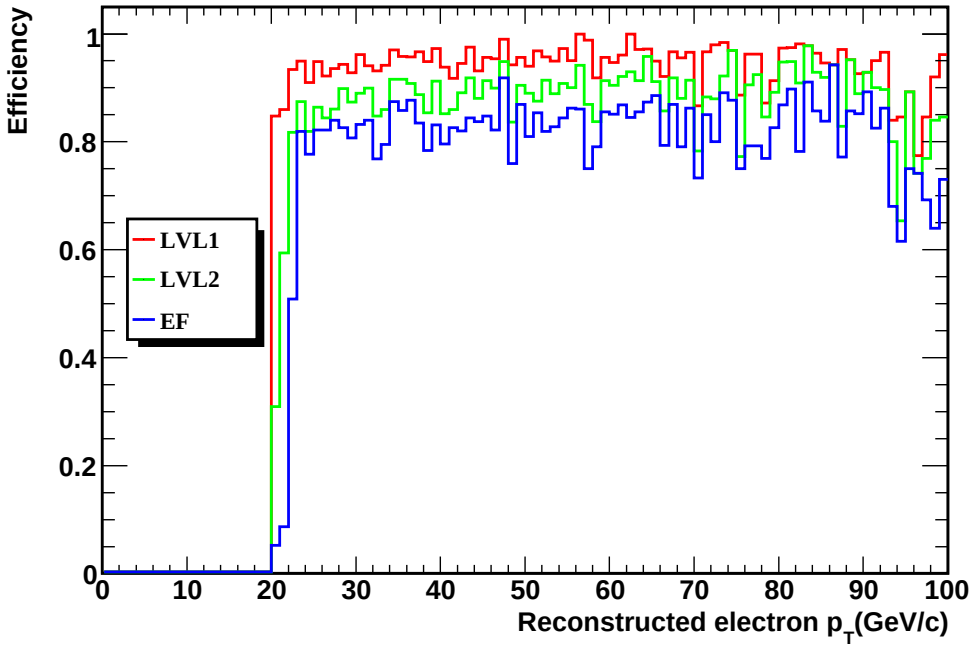

Figure 5.7: Turn-on curve of e25i trigger with respect to the reconstructed electron p_T in $t\bar{t}$ events.

Table 5.4: Trigger (e25i) efficiencies for electrons.

Trigger level	**# events (offline)**	**Efficiencies (%)**
No trigger	8338	-
L1 EM25I	7818	93.7 ± 0.06
L2 e25i	7151	85.7 ± 0.06
EF e25i	6453	77.3 ± 0.09

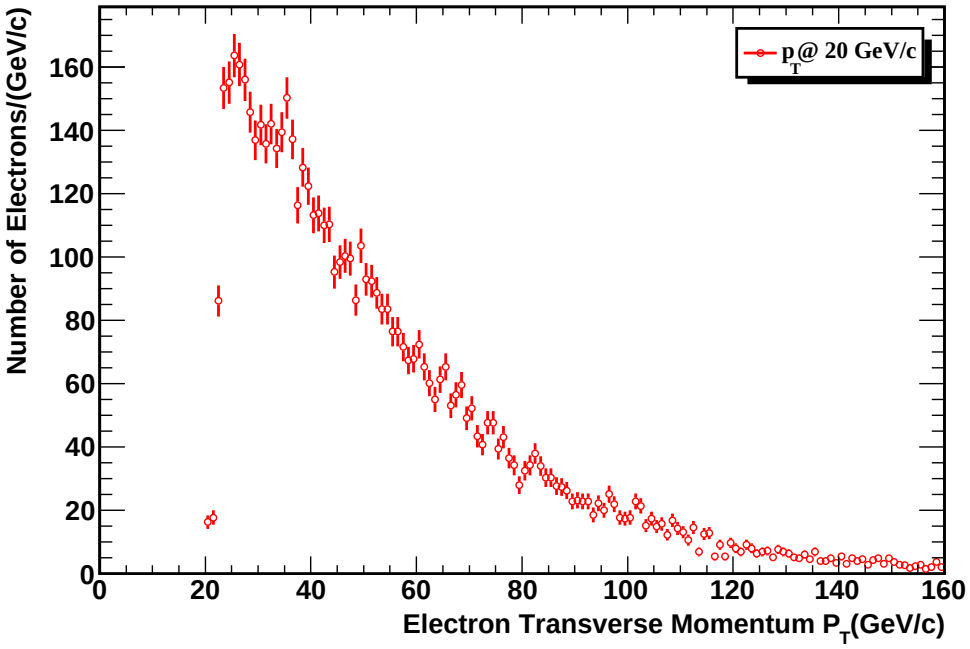

Figure 5.8: Electron transverse momentum distribution after passing the trigger and offline selections.

5.3.3 Muon selection

Muons are extracted from the "StacoMuonCollection" AOD container. STACO (STAtistical COmbination) attempts to statistically merge the two independent measurements derived from the inner detector track with the muon spectrometer track at the interaction point. There are two algorithms to identify muons: a high-p_T and a low-p_T algorithm. For W semileptonic decay, the high-p_T algorithm is required due to the W large mass. Muons are identified by the best match between the muon chambers and the tracker's information (i.e. isCombinedMuon() and isBestMatch() have to be true). Muons are reconstructed in the pseudo-rapidity range $0 \leq |\eta| \leq 2.5$ and have to be isolated based on calorimeter energy. The additional transverse energy E_T in a cone with radius $\Delta R = 0.2$ around the muon is required to be less than 6 GeV. Based on the above selections, muon p_T and muon pseudo-rapidity distributions are shown in figure 5.9 (a), (b), respectively. Since muons do not fake jets like electrons, no muon trigger studies are done in this analysis. The efficiency for $p_T > 20$ GeV/c with respect to $p_T > 10$ GeV/c is around 82% (from figure 5.9(a)).

5.3.4 Jet selection

There must be four jets available in the "MyPreSelectedParticleJets" container since no b-tagging has been done. These jets are light jets and/or b-jets. We first collect all jets by requiring the transverse momentum of 20 GeV/c or higher and the distance between reconstructed and the corresponding Monte Carlo jets with cone radius of 0.4 in $\eta - \phi$ space. The distribution of four leading jets (jets with the largest transverse momentum) are shown in figure 5.10. Jets coinciding with electrons, muons, taus or photons are known as overlapped objects and/or fake jets and are removed if they fall within $\Delta R < 0.2$. Figure 5.11 shows the leading jet distributions after removing fake or overlap jets and by imposing a 40 GeV/c p_T requirement. Jets in $t\bar{t}$ events typically

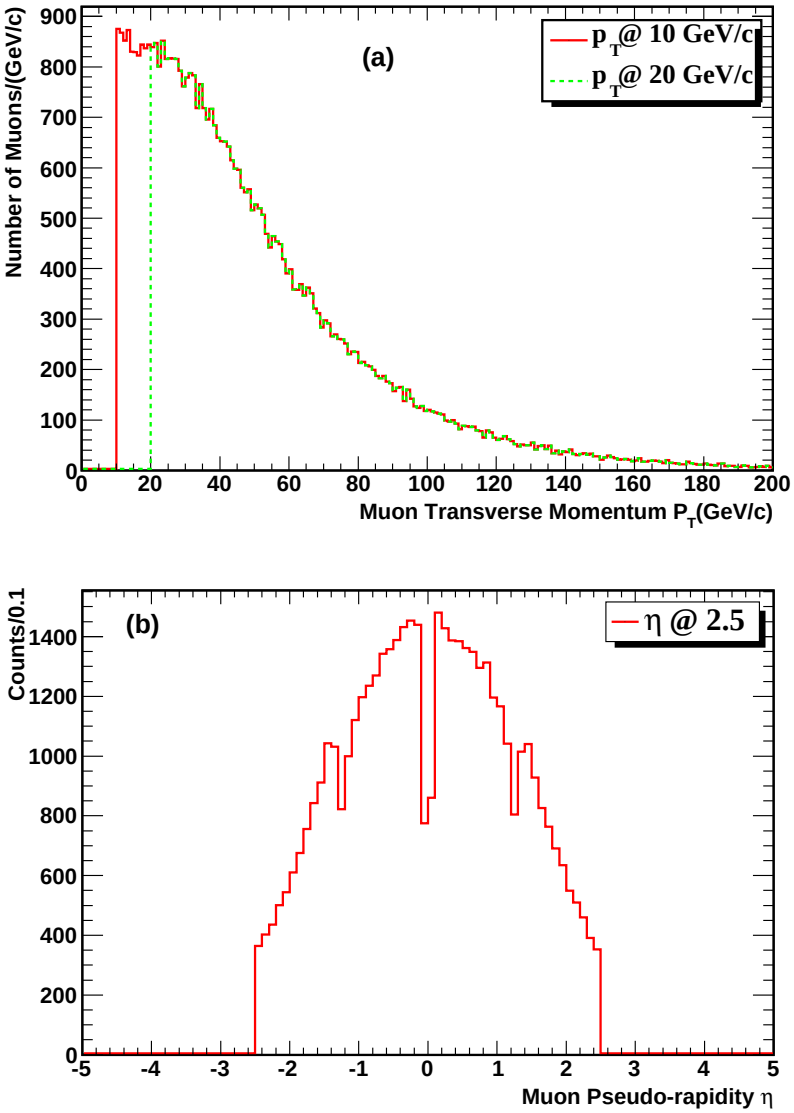

Figure 5.9: Muon a) transverse momentum and b) pseudo-rapidity distributions in $t\bar{t}$ events. Due to the support structures and/or passages for services the number of measurements is less at $|\eta| = 0$ as shown in (b).

have high transverse momentum due to the large top quark mass.

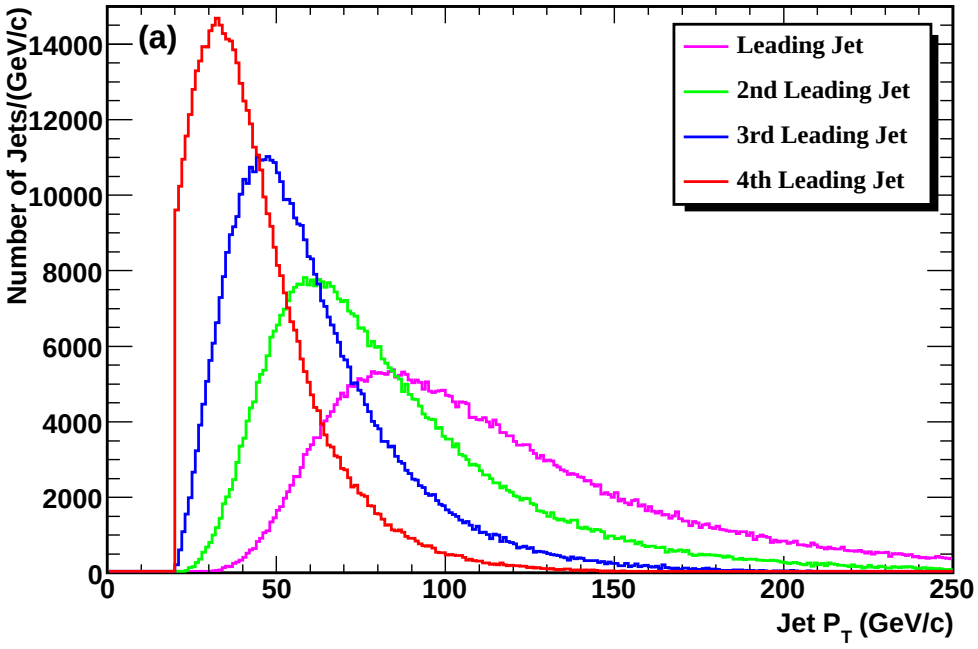

Figure 5.10: Transverse momentum distribution of the four leading jets in $t\bar{t}$ events.

5.4 Jet reconstruction algorithms

We studied several jet algorithms to make a comparison among them and get the best reconstruction. Jets are initiated by quarks and gluons in a hard scattering pp collision. Once jets enter into a detector, the effects of particle showering, detector response, noise, and energy from additional hard scatterings from the same beam crossing will subtly affect the performance of even the most ideal algorithm. It is the goal of the experimental groups to correct for such effects in each jet algorithm. The two main jet definitions in use by the ATLAS experiment are the Cone Jet and K_T Jet based algorithms.

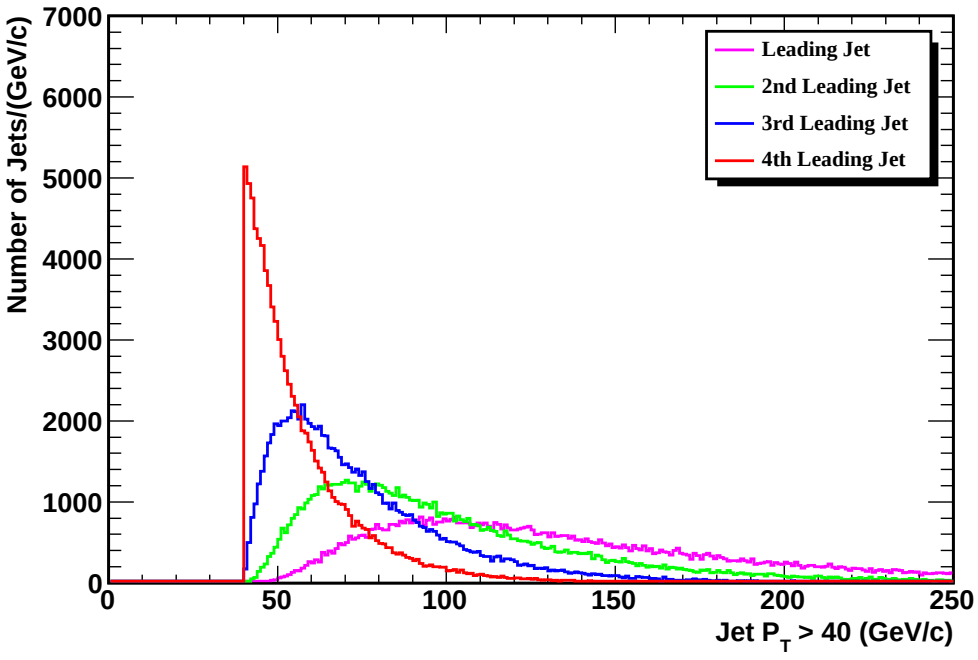

Figure 5.11: Transverse momentum distribution of 4 leading jets with $p_T >$ 40 GeV/c for W mass reconstruction.

Cone algorithm

Cone algorithms form jets by associating together particles whose trajectories lie within a circle of specific radius R in $\eta \times \phi$ space. This 2-dimensional space is natural in pp collisions, where the dynamics are spread out in the longitudinal direction. Starting with a trial geometric centre (or axis) for a cone in $\eta \times \phi$ space, the energy-weighted centroid is calculated including contributions from all particles within the cone. This new point in $\eta \times \phi$ is then used as the centre for a new trial cone and in an iterative procedure, the jets are being reconstructed until a stable configuration is found. Two different implementations exist: the first one, called seeded cone jet finder, uses high E_T objects in the event as a starting point (typically 1 GeV), whereas the second, seed-less implementation, is much slower but theoretically more accurate [80]. In both scenarios, the jets obtained undergo a split-merge procedure, to define non-overlapping exclusive jets. The particles are specified by massless 4-vectors $p^{i\mu}$ $= (|\vec{p}^{\,i}|, \vec{p}^{\,i})$ with angles (ϕ^i, θ^i) given by the direction from the interaction point with unit vector $\hat{p}^i = \frac{\vec{p}^{\,i}}{|\vec{p}^{\,i}|}$. The scalar E_T for each particle is $E_T^i = E^i \sin(\theta^i)$. For a specified geometric centre for the cone (η^C, ϕ^C), the particles i within the cone satisfy

$$i \subset C : \sqrt{(\eta^i - \eta^C)^2 + (\phi^i - \phi^C)^2} \leq R. \tag{5.1}$$

A seedless algorithm is infrared insensitive (to soft radiation in an event). It searches the entire detector and finds all stable cones, even if these cones do not have a seed tower at their centre.

K_T algorithm

The second class of jet algorithms consists of the K_T algorithm [97], which uses the knowledge that final state particles in a shower are largely collinear, i.e. have small transverse momentum between their constituent particles. Such jets do not necessarily have a cone-shape with a fixed radius. Instead, the algorithm clusters "nearest" protojets together, depending on their relative

transverse momentum. A flowchart of the K_T algorithm is shown in figure 5.12. Starting with a list of preclusters and an empty list of jets, the steps of the algorithm are as follows:

1. For each precluster i in the list, define

$$d_i = p_{T,i}^2. \tag{5.2}$$

For each pair (i, j) of preclusters $(i \neq j)$, define

$$\begin{aligned} d_{ij} &= min(p_{Ti}^2, p_{Tj}^2)\Delta R_{ij}^2/D^2 \\ &= min(p_{Ti}^2, p_{Tj}^2)\frac{(\eta_i - \eta_j)^2 + (\phi_i - \phi_j)^2}{D^2}, \end{aligned} \tag{5.3}$$

where $D \approx 1$ is a parameter of the jet algorithm. For $D = 1$ and $\Delta R_{ij} \ll 1$, d_{ij} is the minimal relative transverse momentum $k_\perp$ (squared) of one vector with respect to the other.

2. Find the minimum of all the d_i and d_{ij} and label it d_{min}.

3. If d_{min} is a d_{ij}, remove preclusters i and j from the list and replace them with a new merged precluster $(E_{ij}, \vec{p}_{ij})$ given by

$$E_{ij} = E_i + E_j, \tag{5.4}$$

$$p_{ij} = \vec{p}_i + \vec{p}_j. \tag{5.5}$$

4. If d_{min} is a d_i, the corresponding precluster i is not mergable. Remove it from the list of preclusters and add it to the list of jets.

5. If any preclusters remain, go to step 1.

The basic input objects for both cone and K_T jet algorithms are either calorimeter towers (defined as a group of cells in a fixed ($\Delta\eta$, $\Delta\phi$) grid), or topological clusters, defined as a group of cells formed around a seed cell. The jets obtained are then calibrated to the hadronic scale using different weighting schemes such as the H1-style[1], whose major drawback is that the set of corrections is specific for each type of jet finder and each value of its parameters [80].

[1]Weights are applied that depend on energy density in calorimeter cell.

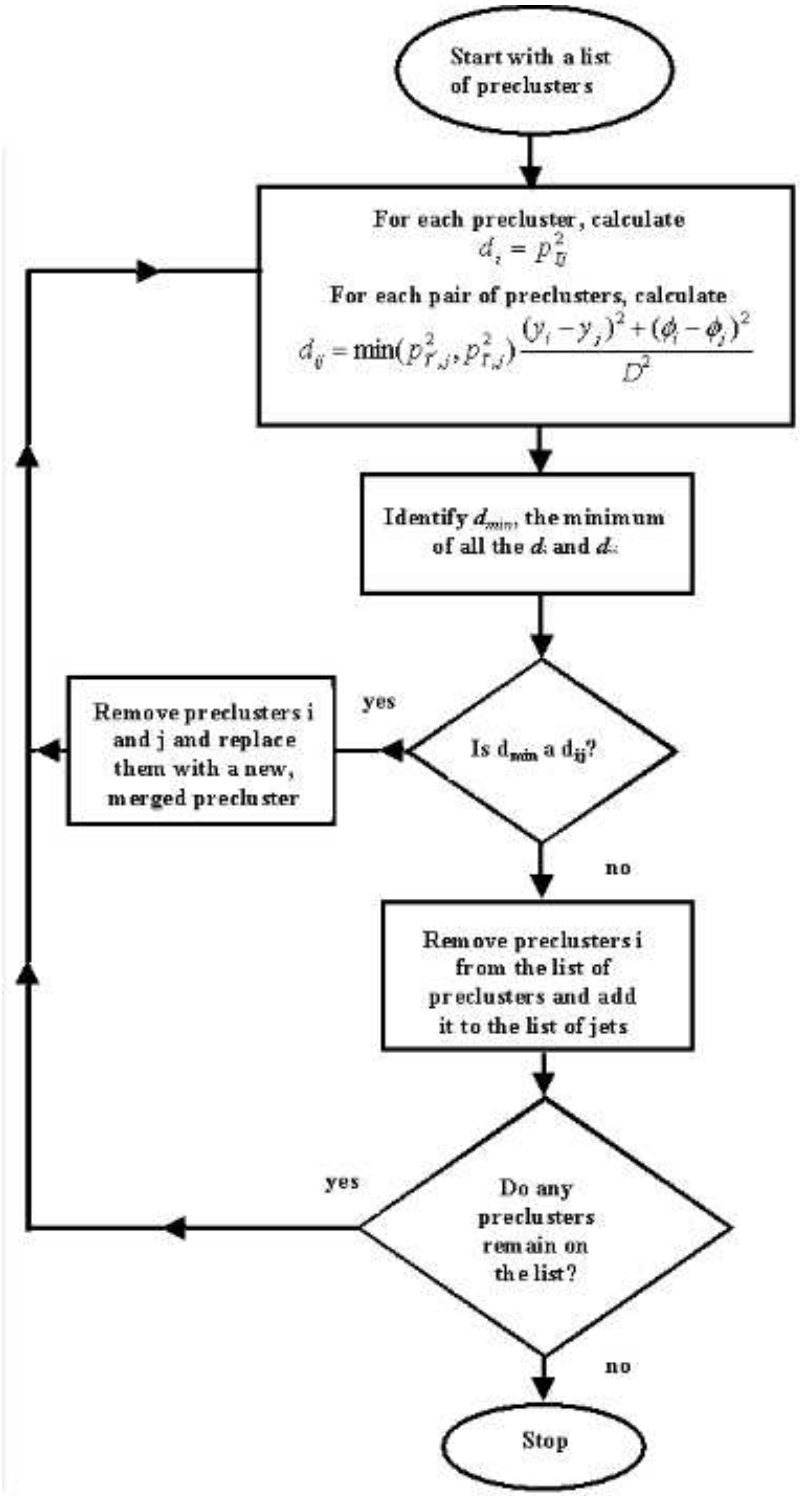

Figure 5.12: Flow chart of the K_T jet algorithm [98].

Figures 5.13 and 5.14 show the distributions of the energy difference between the matched quark and jet, divided by the quark energy for different energy ranges. Our purpose is to find the best algorithm, which are defined to be the best jet energy resolution. We used both cone and K_T algorithms with different sizes. We see that the bigger jets (according to the cone size or d spacing values) lead, especially in low energies, to a worst resolution and longer tails due to the overestimation of jet energies, while overlapping with underlying events in those regions. Each individual distribution is fitted with a gaussian function to obtain the energy resolution values from the standard deviation (σ) of the fits. These σ's are then plotted with respect to the quark

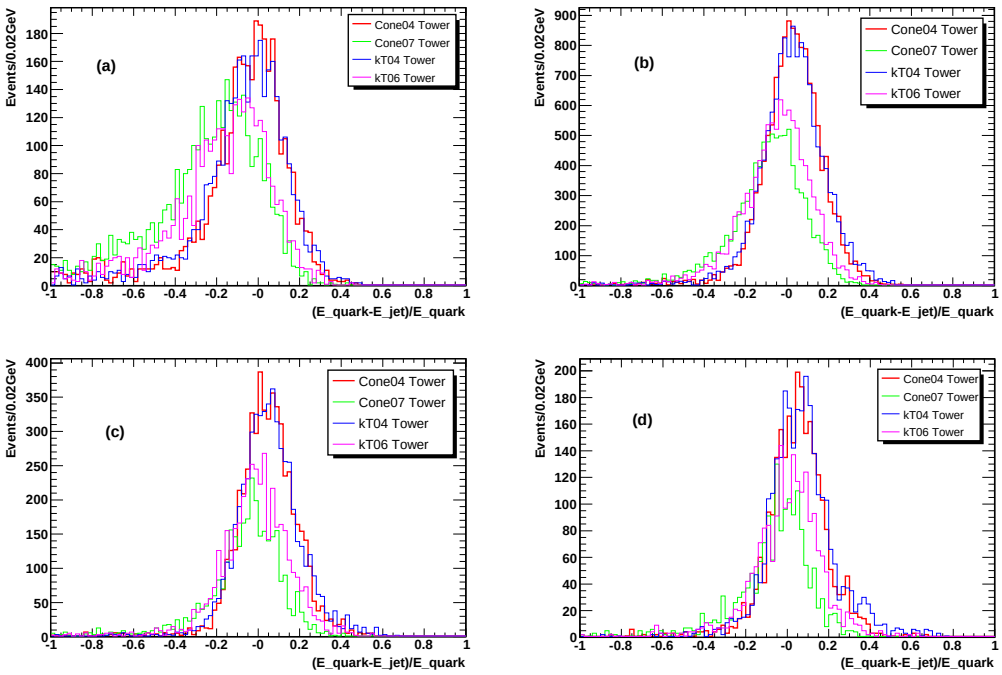

Figure 5.13: Distribution of $(E_{quark} - E_{jet})/E_{quark}$ for the light jets from the W decay for (a) 15 - 50 GeV (b) 50 - 100 GeV (c) 100 - 150 GeV and (d) 150 - 200 GeV energy ranges.

energies in figure 5.15, where the red solid lines are for a cone with $R = 0.4$, pink lines are for a cone with $R = 0.7$, blue lines are for K_T with $R = 0.4$ and green lines are for K_T with $R = 0.6$. All of these four algorithms are for

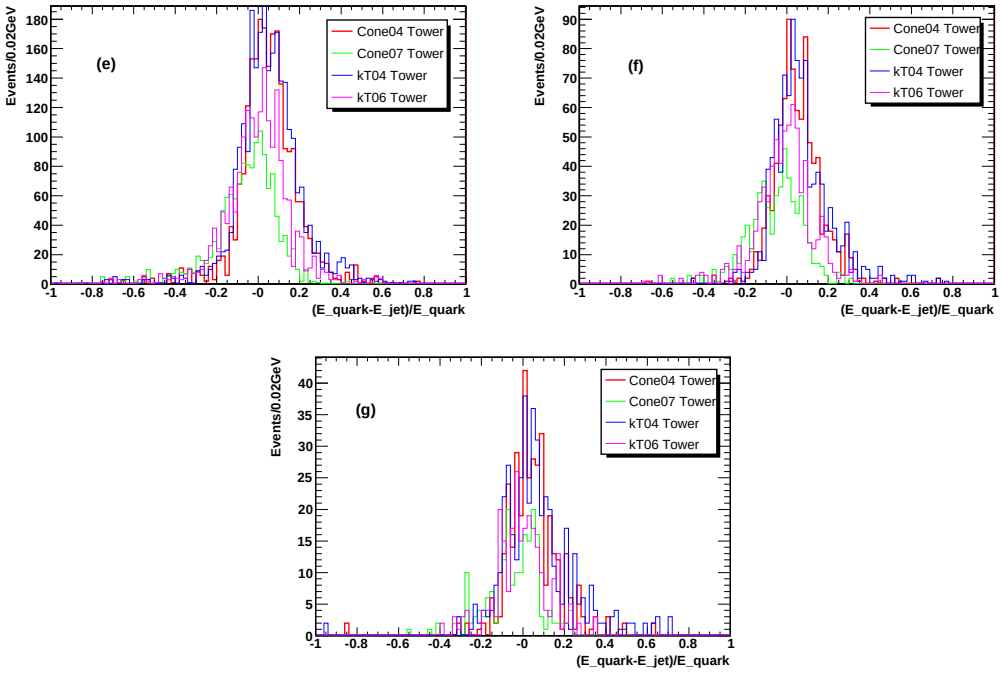

Figure 5.14: Distribution of $(E_{quark} - E_{jet})/E_{quark}$ for the light jets from the W decay for (e) 200 - 300 GeV (f) 300 - 400 GeV and (g) 400 - 500 GeV energy ranges.

the calorimeter tower clustering. The topological clusters are also studied and plotted in figure 5.15, where green solid triangles are for a cone topological cluster with $R = 0.4$ and so on. We conclude here that:

- When jets are made from towers, small sizes are preferable, especially for the cone algorithm.
- The algorithms using topological clusters seem to behave very well.

Based on these studies we will use cone with $R = 0.4$ tower algorithm for mass reconstruction and calibration.

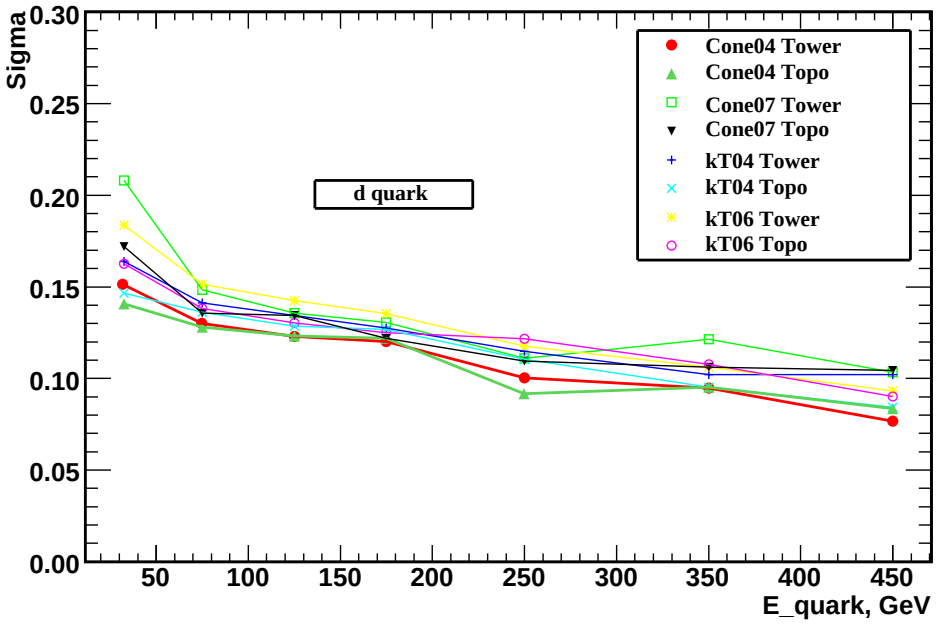

Figure 5.15: Energy resolution for light jets as a function of the quark energy for various jet algorithms. No errors are included in this picture.

5.5 Mass reconstruction

Now we reconstruct the top and W mass from the four leading jets described above. In the absence of b-tagging, there is an additional ambiguity

in choosing the correct three-jet combination among the reconstructed jets. Therefore we define our top quark candidate as the three jet combination with the highest transverse momentum (four momentum vector sum) out of four jets. Every three jet combination that originates from a top decay also contains a two jet combination that originate from a W boson decay. And therefore we define our W boson candidate as the two jet combination with the closest mass to W mass out of three jets in the assumed top candidate. The invariant mass is a quantity that is the same for all frames of references, which is calculated for the W from the following formula:

$$M_{j1j2} = \sqrt{2E_{j1}E_{j2}(1 - cos\theta_{j1j2})}, \tag{5.6}$$

where $cos\theta_{j1j2} = \frac{\vec{p}_{j1}\cdot\vec{p}_{j2}}{|\vec{p}_{j1}||\vec{p}_{j2}|}$, E_{j1} and E_{j2} are the energies of jet1 and jet2 respectively and $\vec{p}_{j1}$ and $\vec{p}_{j2}$ are the momenta of the corresponding jets. We use the known value of the W boson mass (80.4 GeV/c^2) as reference to get the correct jet combination whose mass is closest to that value. The remaining third jet is assumed to be the b-quark. The distribution for the reconstructed top and W mass based on the above mentioned permutations and cone algorithm with $R = 0.4$ (Tower) are shown in figures 5.16 and 5.17. In both cases the blue distributions are from the sum of W + jets, green distributions are from the sum of single-top and pink distributions are from the sum of QCD dijets backgrounds. Clearly, the W + jets and single top backgrounds are smaller than the combinatorial backgrounds from signal events (wrong combination of jets etc.). Since the cone algorithm with radius $R = 0.4$ is the best choice for the energy resolution we plot them separately including physical backgrounds from W + jets and single top events. Figures 5.18 and 5.19 show the W mass and the reconstructed top distributions for different cone and K_T algorithms without physical (i.e. W + jets, single top, etc.) backgrounds.

To obtain mass values from the invariant mass distributions of figure 5.16 and 5.17, the sum of a gaussian and 6th order Chebychev polynomial is fit to the distributions. The polynomial mostly describes the background from

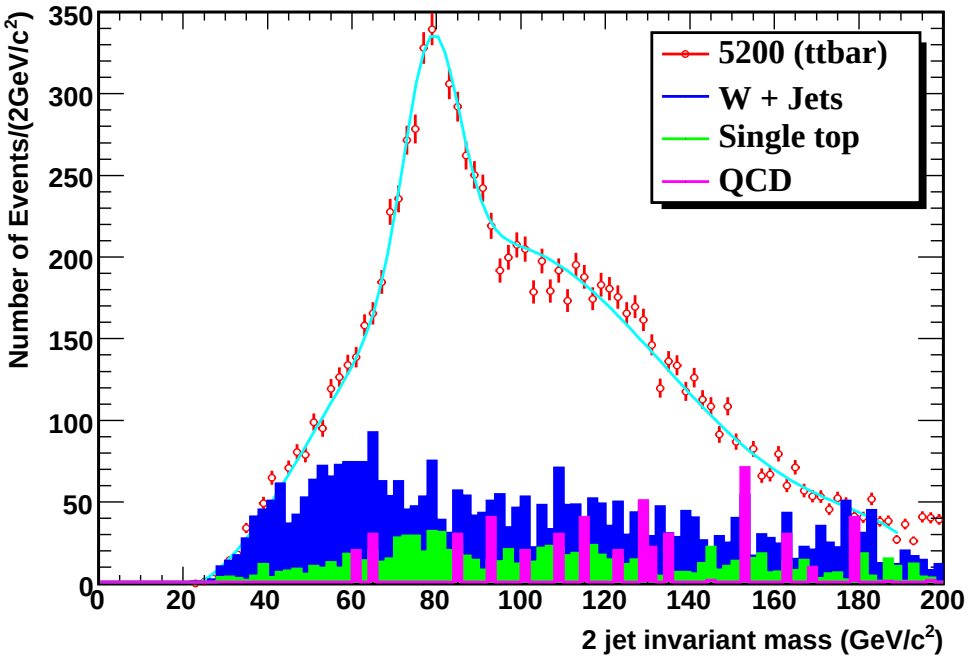

Figure 5.16: Two jet invariant mass distribution.

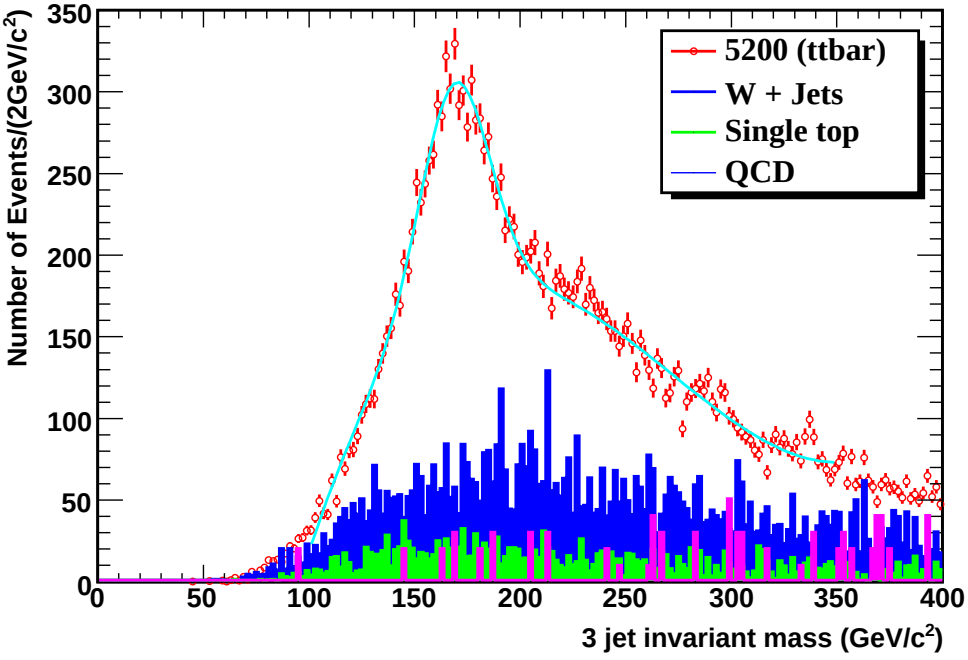

Figure 5.17: Three jet invariant mass distribution with 2 jets constrained to the W mass.

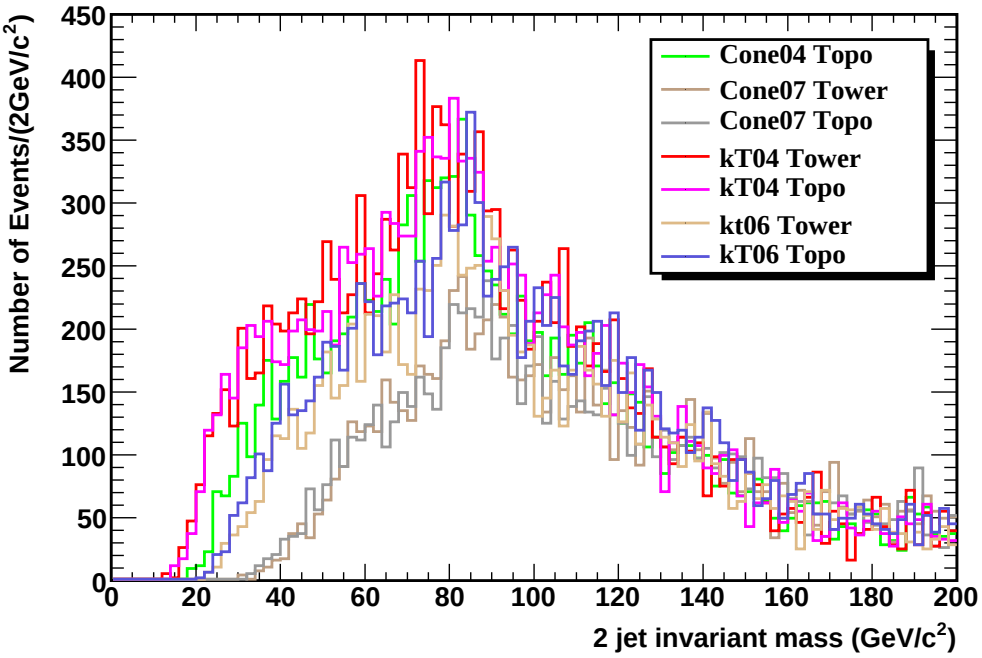

Figure 5.18: Two jet invariant mass distributions for different cone and K_T algorithms.

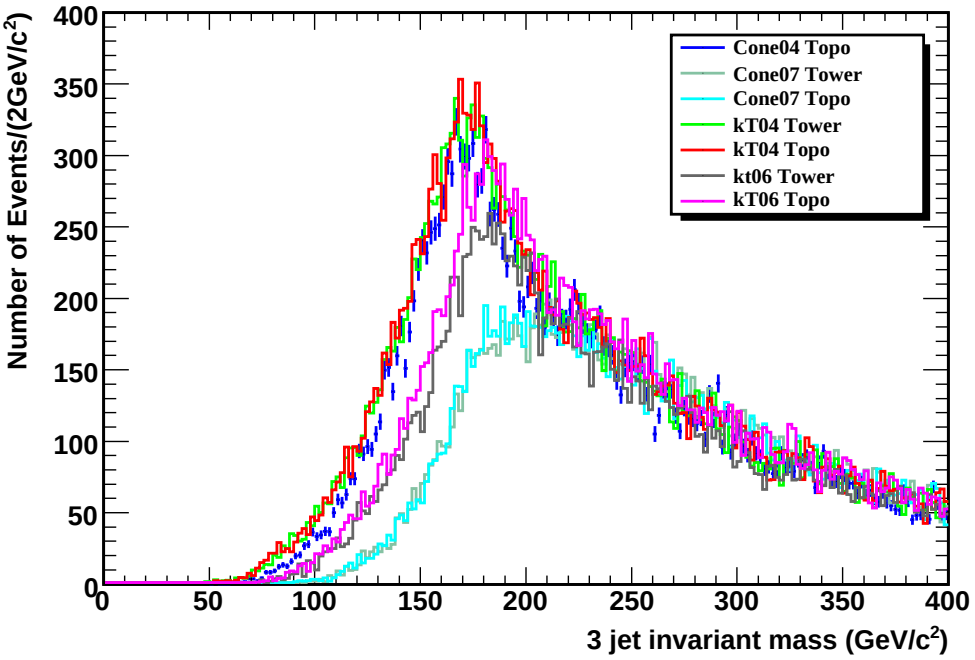

Figure 5.19: Three jet invariant mass distributions for different cone and K_T algorithms.

wrong jet combinations and from background events, whereas the mean value of the gaussian and its error are interpreted as the mass and its statistical error, whereas the standard deviation (width) of the gaussian fit is referred to as the mass resolution respectively. Table 5.5 shows the fitted values.

Table 5.5: Fitted results for the top quark and W mass distributions using different jet algorithms.

Definition(s)	W mass distribution	Top mass distribution
Cone04 Tower :		
Mean mass (GeV/c^2)	78.86 ± 0.23	169.09 ± 0.39
Mass resolution (GeV/c^2)	6.47 ± 0.26	16.27 ± 0.49
Cone04 Topo :		
Mean mass (GeV/c^2)	79.59 ± 0.62	169.8 ± 0.4
Mass resolution (GeV/c^2)	6.68 ± 0.7	15.96 ± 0.49
K_T04 Tower :		
Mean mass (GeV/c^2)	79.22 ± 0.81	171.1 ± 0.5
Mass resolution (GeV/c^2)	8.42 ± 0.75	17.56 ± 0.58
K_T04 Topo :		
Mean mass (GeV/c^2)	80.03 ± 0.65	170.9 ± 0.4
Mass resolution (GeV/c^2)	7.46 ± 0.873	17.86 ± 0.54
cone07 Tower :		
Mean mass (GeV/c^2)	70.37 ± 2.22	197.7 ± 0.5
Mass resolution (GeV/c^2)	59.29 ± 2.04	40.99 ± 0.63
cone07 Topo :		
Mean mass (GeV/c^2)	84.04 ± 0.94	197.4 ± 0.5
Mass resolution (GeV/c^2)	25.8 ± 1.6	37.52 ± 0.6
K_T06 Tower :		
Mean mass (GeV/c^2)	70.09 ± 2.31	185.4 ± 0.5
Mass resolution (GeV/c^2)	40.59 ± 3.29	21.98 ± 0.84
K_T06 Topo :		
Mean mass (GeV/c^2)	67.16 ± 3.93	184.2 ± 0.4
Mass resolution (GeV/c^2)	52.93 ± 6.76	21.15 ± 0.7

From table 5.5 one can see that the mass resolution of the W for a cone with radius $R = 0.4$ is the lowest, though using topological clusters with the same cone size is promising. But still this mass resolution is very far from the

known value (width of the W boson 2.124 GeV/c^2 [99]). This is mainly due to the large uncertainties in the light jet energy. Figures 5.20 and 5.21 show the transverse momentum and pseudo-rapidity distributions for the light jets coming from the all W decay in $t\bar{t}$ events. The events, passing the selection cuts are known to be the good light jets and are considered for the resolution studies by fitting the distribution of the difference between light jet energy and the corresponding MC jet energy using a gaussian function in various jet energy bins. An example of the energy difference in the jet energy bin 40-50 GeV is shown in figure 5.22. How the jet energy resolution depends on jet energy is shown in figure 5.23.

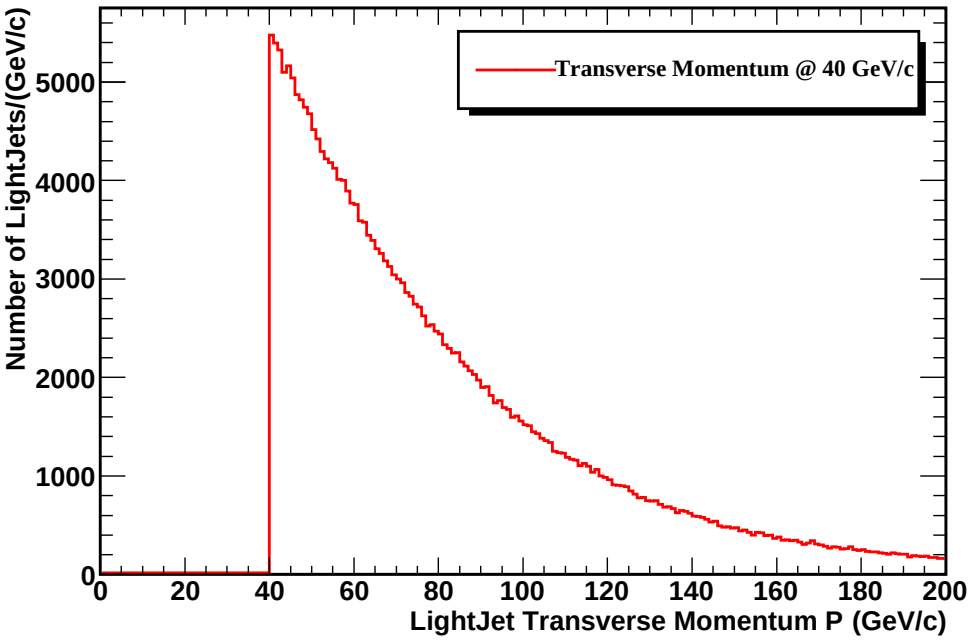

Figure 5.20: Transverse momentum distribution of the light jets.

The poorly reconstructed mass resolution can be further improved by recalibrating the jet energy through a χ^2 minimization [100] given by equation 5.7. MINUIT2 [101], a function minimization and error analysis package has been

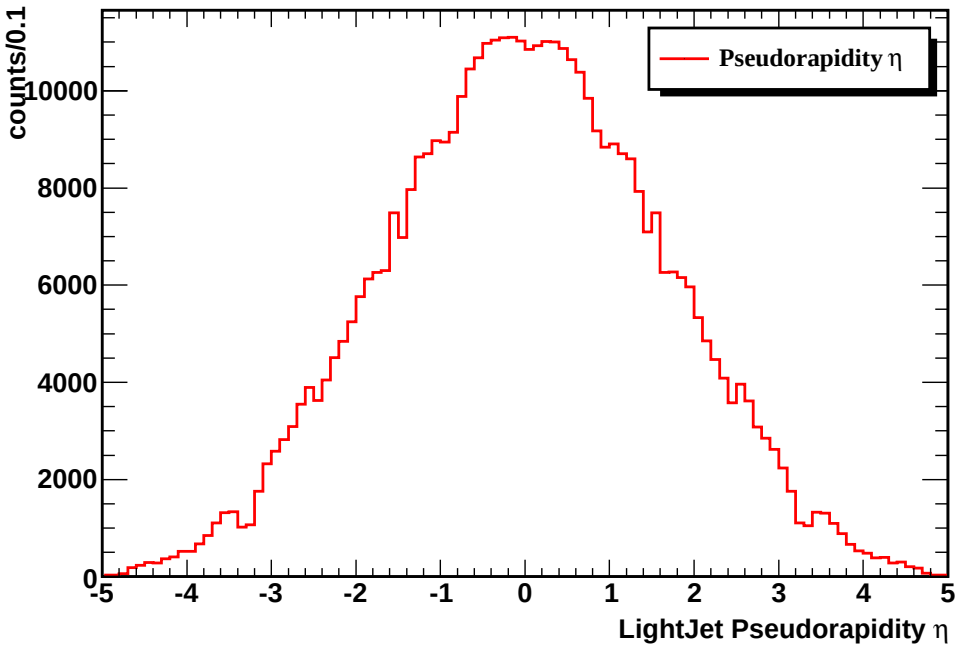

Figure 5.21: Pseudo-rapidity distribution of the light jets.

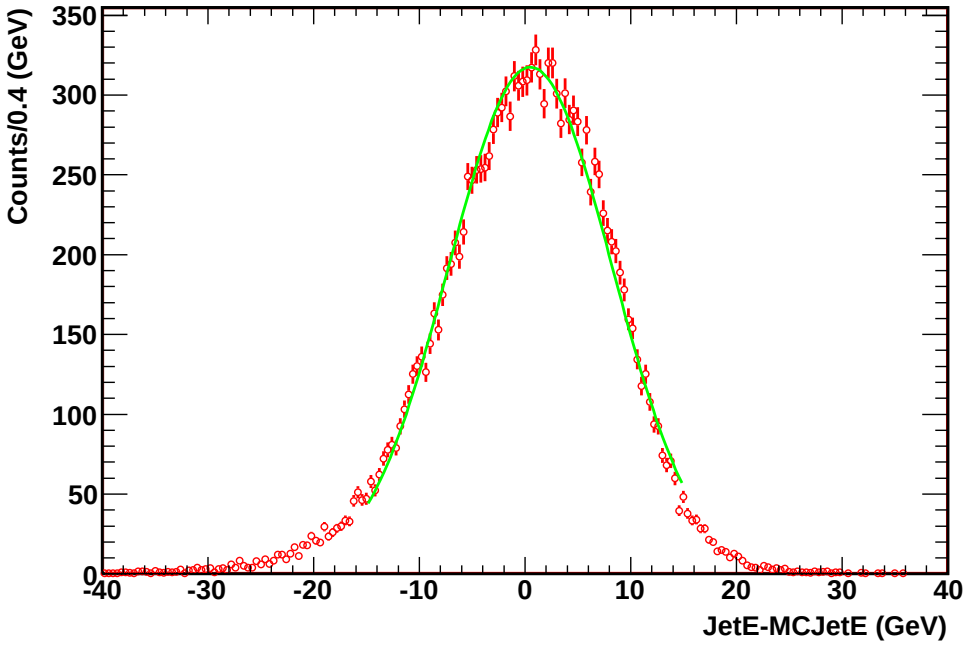

Figure 5.22: Reconstructed light jet energy minus the corresponding Monte Carlo jet energy fit to a Gaussian function in the jet energy bin 40-50 GeV.

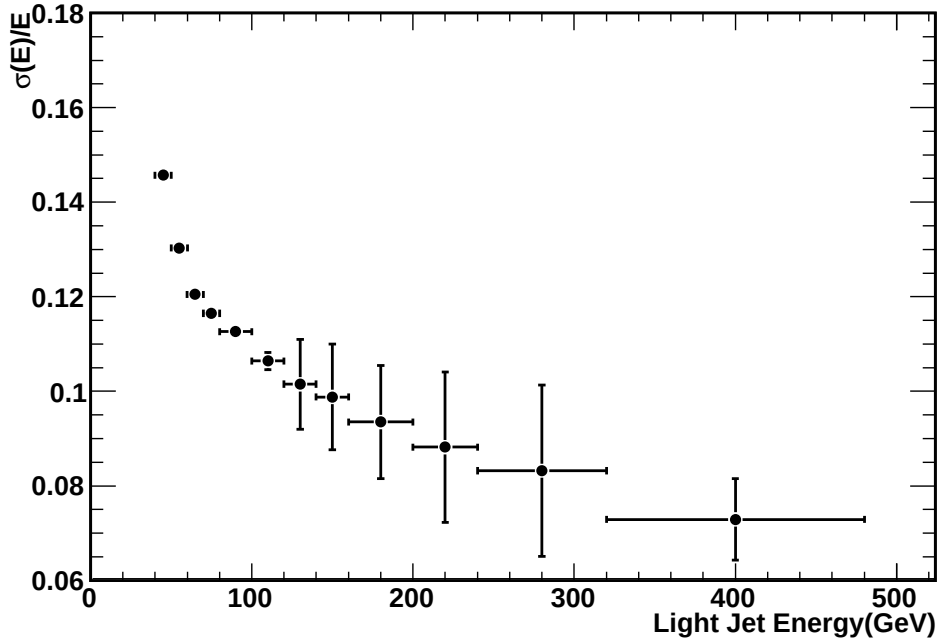

Figure 5.23: Energy resolution versus light jet energy.

used.

$$\chi^2 = \frac{(M^{rec.}_{j1j2} - M^{PDG}_W)^2}{\Gamma^2_W} + \frac{(E_{j1}(1-\alpha_{j1}))^2}{\sigma^2_{j1}} + \frac{(E_{j2}(1-\alpha_{j2}))^2}{\sigma^2_{j2}}. \qquad (5.7)$$

The χ^2 is the sum of three terms: the first (and leading) one corresponds to the constraint of the jet pair invariant mass $M^{rec.}_{j1j2}$ to the PDG W mass M^{PDG}_W; the others correspond to the jet energy correction factors α_1, α_2 to be determined by MINUIT2 and σ_i's, are the resolution on the light jet energy determined as explained above (figure 5.22). The light jet pair j1, j2 corresponding to the minimum χ^2 is kept as the hadronic W candidate. This minimization procedure also leads to the corresponding energy correction factors α_{j1} and α_{j2}, whose distributions are shown in the figure 5.24. Once α_{j1} and α_{j2} are obtained, we are than able to get the new jet energies and the invariant mass of the W by the following formulas:

$$M^{new}_{j1j2} \equiv \sqrt{2E_{j1}\alpha_{j1}E_{j2}\alpha_{j2}(1 - cos\theta^{new}_{j1j2})},$$

$$M_{j1j2}^{new} \equiv \sqrt{\alpha_1 \alpha_2} M_{j1j2}. \tag{5.8}$$

The $\sqrt{\alpha_1 \alpha_2}$ distribution versus reconstructed jet energy is plotted in figure 5.25. The new W invariant mass after calibration is shown in figure 5.26. We consider only the hadronic W candidates which belong to a mass window of $\pm 3\sigma_{j1j2}$ (σ_{j1j2} is the resolution before calibration). The mean value and the standard deviation (width) of the gaussian fit are 80.67 $\pm$ 0.02 GeV/c^2 and 1.70 $\pm$ 0.03 GeV/c^2, which are greatly improved when compared to the results before calibration (table 5.5). We now impose this W mass constraint to the top quark mass reconstruction and get the new top mass distribution, which is plotted in the figure 5.27. The new top quark mass improves to 171 $\pm$ 0.4 GeV/c^2 from 169.09 $\pm$ 0.39 GeV/c^2 and this mass distribution can be further tuned up by calibrating the b-jet energy scale, which was beyond the scope of this thesis.

Figures 5.28 and 5.29 are the distributions of the energy ratio between the energy difference of the reconstructed jet and the corresponding quark over the quark energy before and after calibration.

Since the calibration is not constant with the energy and pseudo-rapidity, and since the two jets from the W decay have in general a different energy, the rescaling method has to be adapted to determine the calibration. Instead of building one jj mass distribution, the first step is to split the studied jet variable in N bins, and to build all associated jj invariant mass distributions. For all energy bins, the ratio of quark energy and the corresponding reconstructed jet energies were calculated before and after calibration and plotted with respect to the reconstructed jet energy in figure 5.30. The calibrated jet energy tends to be closer to the quark energy, the difference is around 1-3% after calibration.

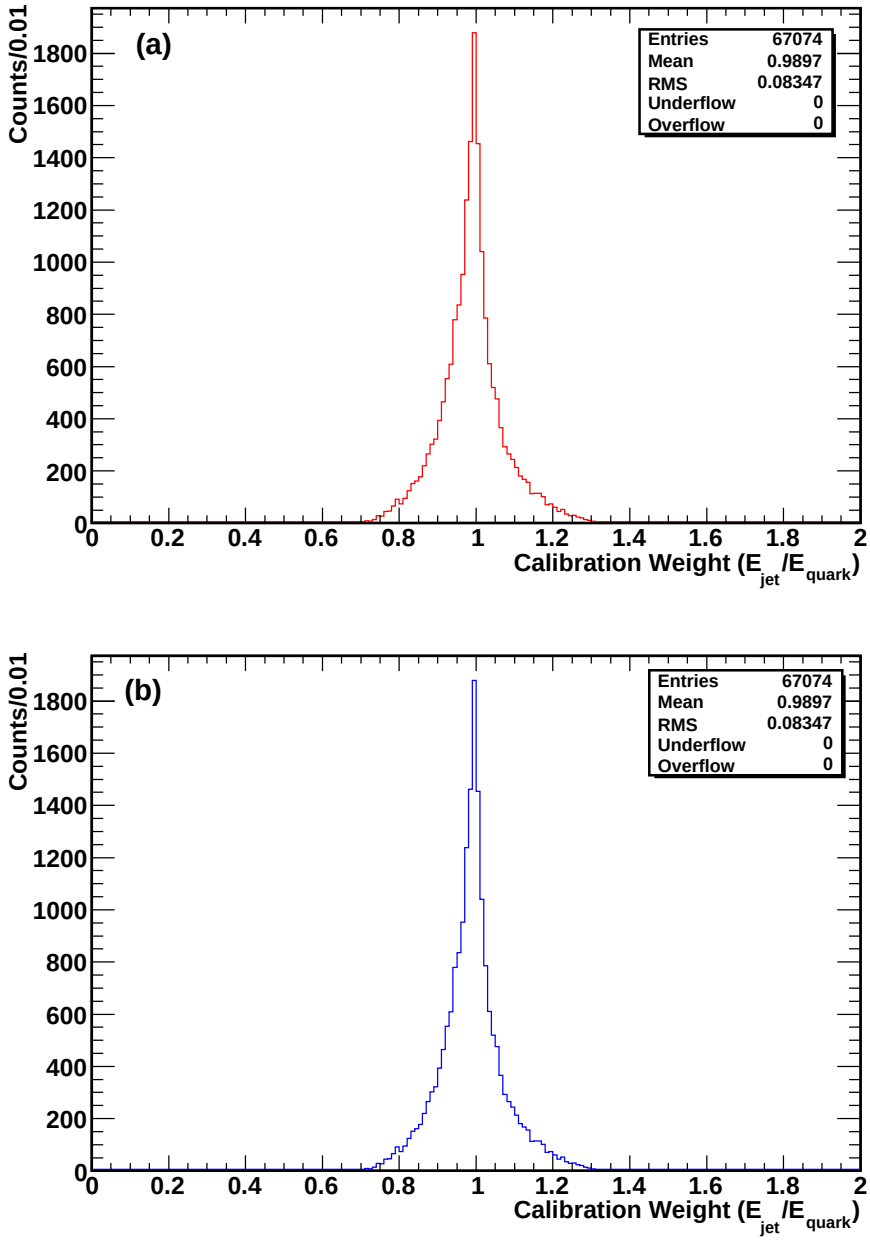

Figure 5.24: Distributions of a) α_{j1} and b) α_{j2} from χ^2 minimization.

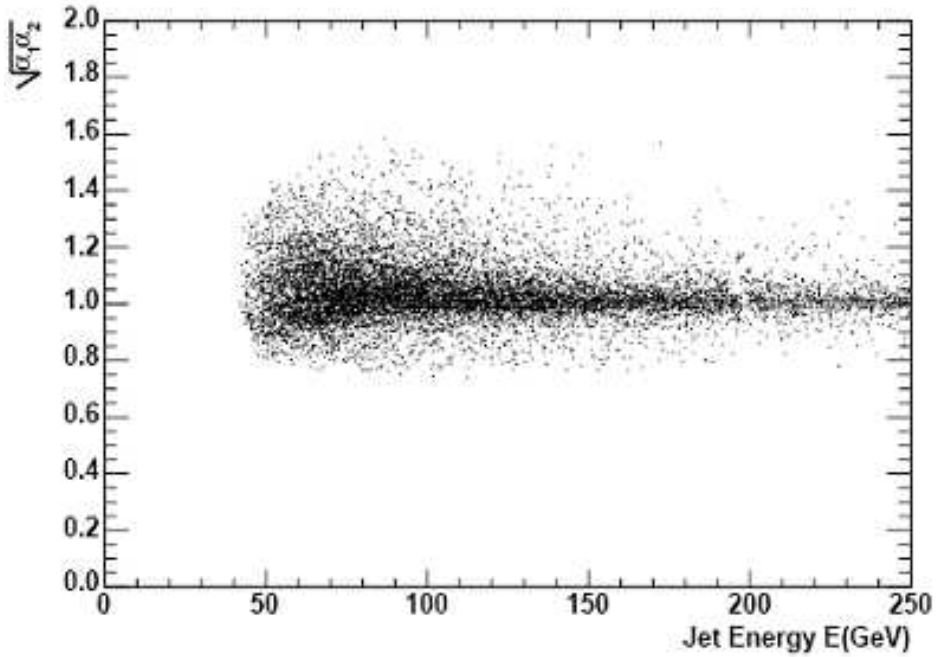

Figure 5.25: $\sqrt{\alpha_1\alpha_2}$ distribution versus mean reconstructed jet energy.

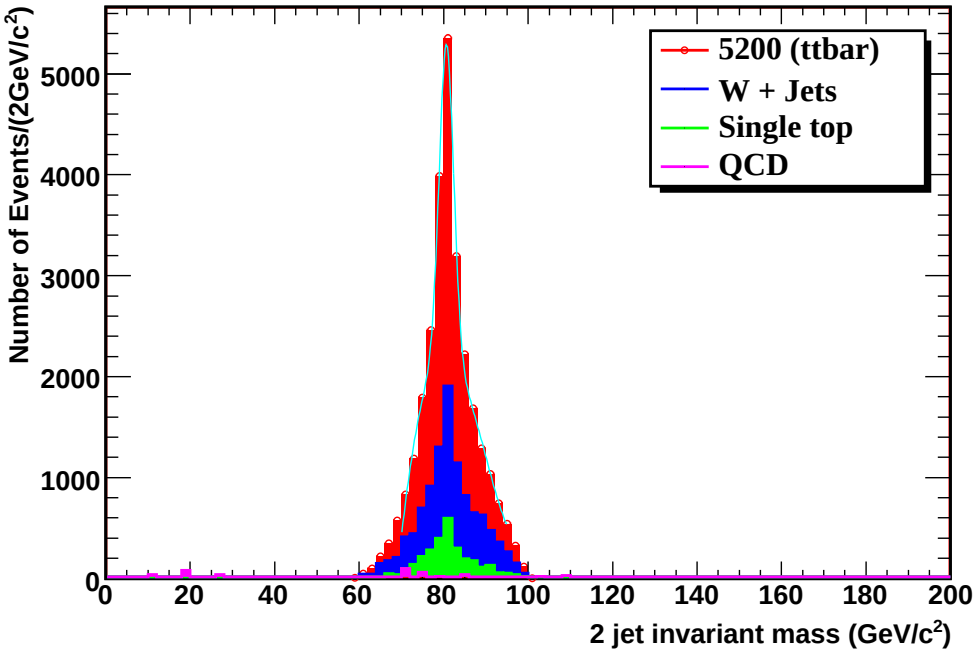

Figure 5.26: Two jet invariant mass after constraint to the W mass.

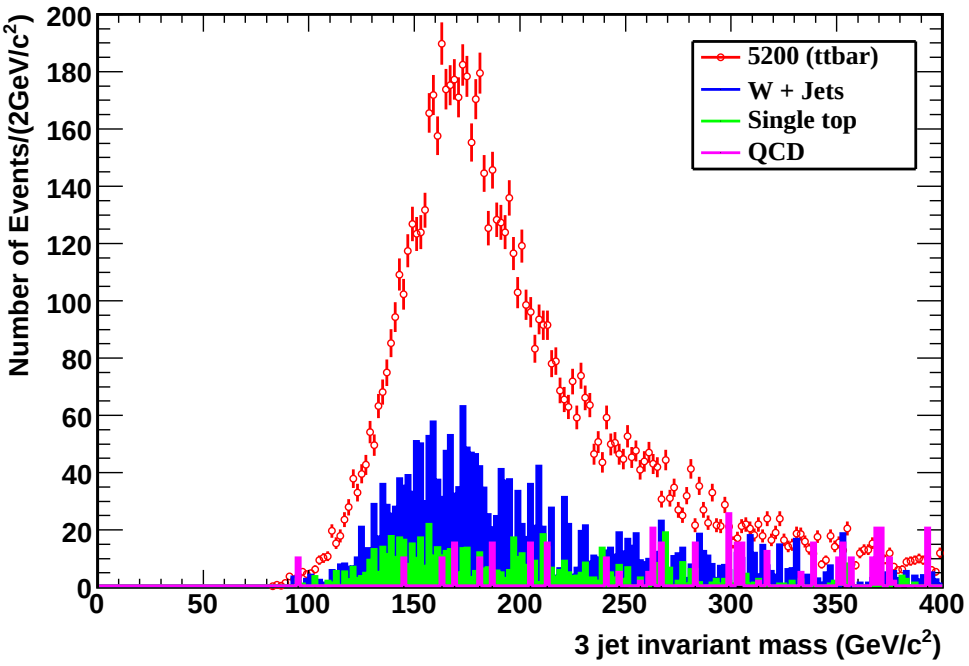

Figure 5.27: Three jet mass distribution after constraining two jets to the W mass.

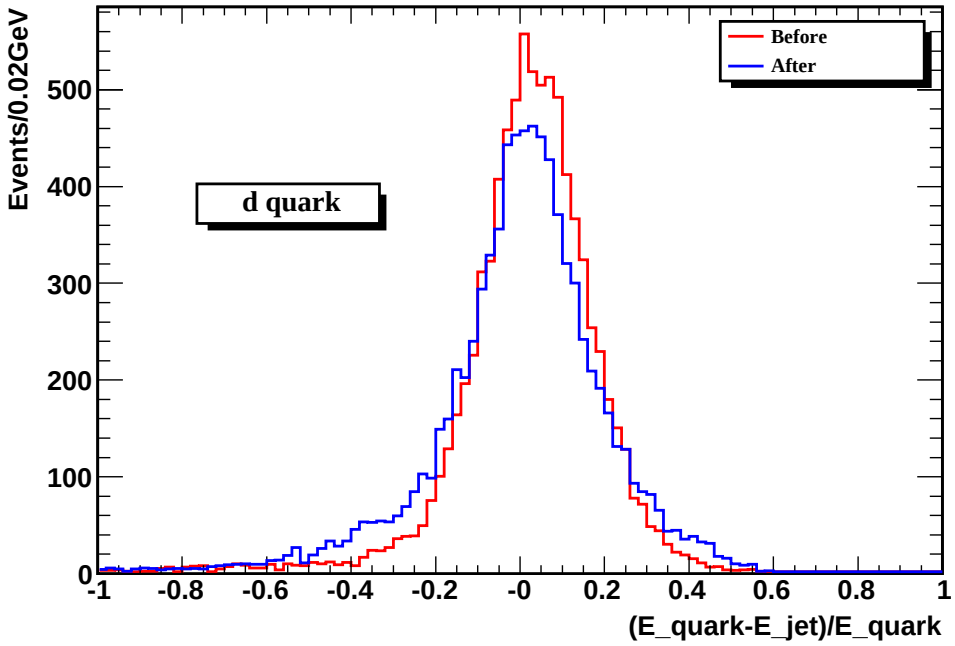

Figure 5.28: Energy ratio of d quark between the matched jet energy and quark energy over quark energy before and after calibration.

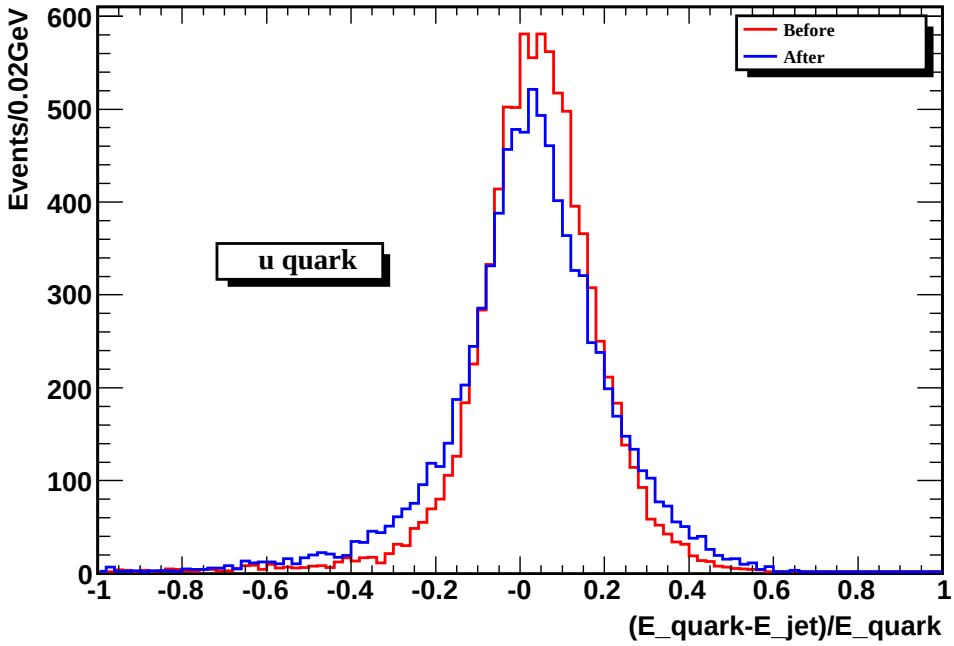

Figure 5.29: Energy ratio of u quark between the matched jet energy and quark energy over quark energy before and after calibration.

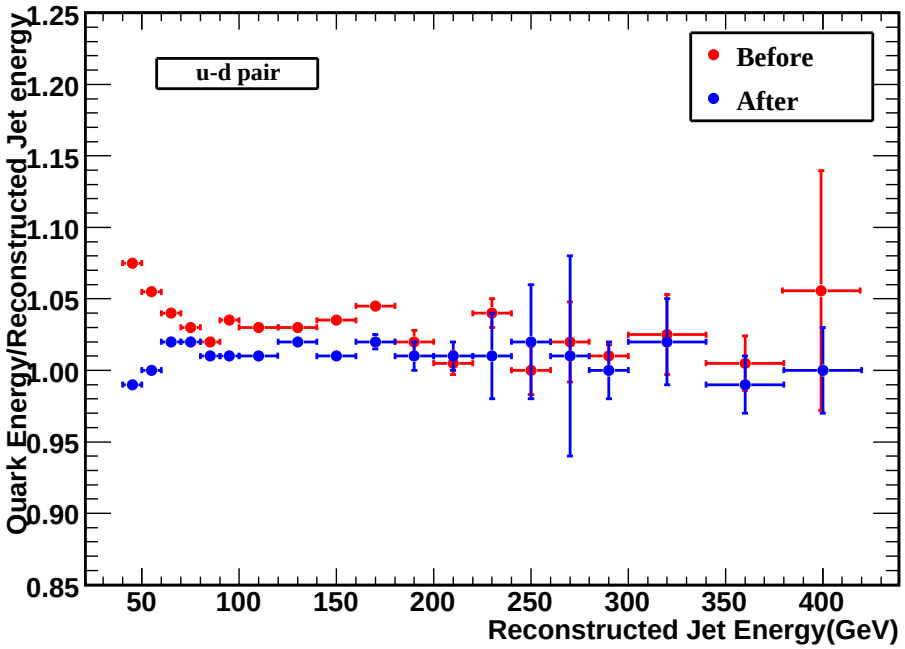

Figure 5.30: Ratio of the quark energy to the reconstructed jet energy from W decay before and after jet energy calibration versus reconstructed jet energy.

5.6 Summary

In order to obtain the jet energy scale, resonance decay calibration method has been studied. Calibration weights are acquired by using event by event process. Several jet finding algorithms are studied and reported in section 5.4. Based on the energy resolution values, the cone tower algorithm with cone size $R = 0.4$ is used for reconstructing jets. The W and top quark mass based on this algorithm are reported in section 5.5. The poor mass resolution is improved by χ^2 minimization. The values of calibration weights and mass resolutions (before and after χ^2 minimization) are also reported in section 5.5. The W and top quark mass are newly reconstructed by using this calibration factors and finally the jet energy scale is achieved. These results (new W and top quark mass and the jet energy scale) are reported in the conclusion chapter.

For the jet enrgy scale (e.g. figure 5.30), only the signal events are considered and the backgrounds have been ignored. In real data in which backgrounds will be presented, the calibration factors may be different. Only J5 and J6 samples are used for QCD backgrounds. Since the cross-section for QCD with $p_T < 280$ GeV is large, there could be significant background in this studies. We have ignored this background.

Chapter 6

Conclusion

The measurement of the top quark properties will be one of the early and important issues at the ATLAS experiment. Due to the large amount of produced events (10^7/year at an integrated luminosity of 10 fb^{-1}) early top quark signals will play an important role in calibrating the light jet energy scale, commissioning the detectors and enabling b-tagging. Beyond the SM, new particles (heavier than the top quark) may decay into top quarks and therefore it is important to understand the top quark properties as precisely as possible. The precise measurement of the hadronic top quark properties (e.g. mass, width) are based on the absolute jet energy scale of light jets and bottom jets.

The properties of light jets, their energy calibration *in situ* and energy scale have been studied and reported in this thesis using $t\bar{t}$ events. The hadronic reconstruction of the top quark ($t \to jjb$) and W boson (from two light jets in top quark candidate) have been considered, which are then used for an *in situ* light jet energy scale measurement. No pile-up is considered in this analysis.

In order to get the best possible mass resolution of reconstructed hadronically decaying Ws, several jet reconstruction algorithms are studied. We find that the "Cone4TowerParticleJets" with cone size $R = 0.4$ is the best choice for reconstructing light jets in $t\bar{t}$ events. The "TopoParticleJets" with small size is also promising. After a comparison of various jet algorithms, we consider the rescaling method of *in situ* jet calibration using the W boson mass

peak in $\pm 3\sigma_{j1j2}$. The χ^2 minimization has been done in order to get the calibration coefficients α's in the same mass window, which is 0.9897. The mean mass and its energy resolution (width) of the W after calibration are 80.67 $\pm$ 0.02 GeV/c^2 and 1.70 $\pm$ 0.03 GeV/c^2, which were 78.86 $\pm$ 0.23 GeV/c^2 and 6.47 $\pm$ 0.26 GeV/c^2 before calibration respectively. The new top quark mass improves to 171 $\pm$ 0.4 GeV/c^2 from 169.09 $\pm$ 0.39 GeV/c^2. Finally, we measured the jet energy scale before and after calibration for different energy bins and obtained 1 - 3% for 100 pb^{-1} luminosity, which improves the top quark mean mass.

Bibliography

[1] http://livefromcern.web.cern.ch.

[2] D. Pallin, "Top Physics at the LHC", Proceedings of Science, International Workshop on Top Quark Physics, Coimbra, Portugal, January 12-15, 2006.

[3] J. Lu, D. M. Gingrich and H. Ahmed, "Investigation of light jet energy calibration and top quark mass measurement using $t\bar{t}$ events with ATLAS", ATL-COM-PHYS-2005-047.

[4] H. Ahmed, "Light Jet Energy Scale Using Semileptonic Top Quark Decay in ttbar Events", an oral presentation at North South Americas (NSA) top meeting, a phone conference, August 27 2008. http://indico.cern.ch/conferenceDisplay.py?confId=40087

[5] H. Ahmed, D. M. Gingrich and J. Lu, "In-situ Jet Energy Calibration", an oral presentation at ATLAS Physics Workshop of Americas, SFU, Barnaby, BC, Canada, June 17 2008. http://indico.cern.ch/conferenceOtherViews.py?confId=29783

[6] H. Ahmed, D. M. Gingrich and J. Lu, "Light Jet Energy Scale in ttbar Events", an oral presentation at ATLAS Canada Physics Workshop, Jesper, April 26 2008. http://indico.cern.ch/conferenceOtherViews.py?confId=15084

[7] H. Ahmed, D. M. Gingrich and J. Lu, "Study of Jet Energy Scale Using ttbar Events", an oral presentation at ATLAS Canada Physics Workshop, University de Montreal, December 18 2007. http://indico.cern.ch/conferenceOtherViews.py?confId=20640

[8] H. Ahmed, D. M. Gingrich and J. Lu, "Update Study of Jet Energy Calibration Using W Decay in ttbar Events", an oral presentation at ATLAS Canada Physics Workshop, University of Regina, August 14 2007. http://indico.cern.ch/conferenceDisplay.py?confId=18191

[9] H. Ahmed, D. M. Gingrich and J. Lu, "Study of in-situ Calibration Using Semileptonic decay of W in ttbar Events", an oral presentation at ATLAS Canada Physics Workshop, University of Victoria, December 12 2006. http://indico.cern.ch/conferenceDisplay.py?confId=5245

[10] M7 "Friends of the Data", http://indico.cern.ch/conferenceDisplay.py?confId=34066.

[11] S. L. Glashow, "Partial-symmetries of weak interactions", Nuclear Physics, Volume 22:579-588,1961.

[12] S. Weinberg, "A Model of Leptons", Phys.Rev.Lett.19:1264-1266,1967.

[13] A. Salam, "Elementary Particle Theory (Nobel Symp. No. 8)", ed. N. Svartholm, Stockholm, 1968.

[14] W. N. Cottingham and D. A. Greenwood, "An Introduction to the Standard Model of Particle Physics", Cambridge University Press, 1998.

[15] F. Halzen and A. D. Martin, "Quarks and Leptons", John Wiley and Sons, 1984.

[16] D. Griffiths, "Introduction to Elementary Particles", Wiley-VCH, 2004.

[17] G. Kane, "Modern Elementary Particle Physics", Perseus publishing, 1993.

[18] J. Mnich, "Precision Measurements at the LHC", Nuclear Physics B (Proc. Suppl.) 160 2-11, 2006.

[19] ALEPH, DELPHI, L3 and OPAL Collaborations, "Search for the Standard Model Higgs Boson at LEP", Phys. Lett. B565 61 2003.

[20] M. Quiros, "Constraints on the Higgs boson properties from the effective potential", hep-ph/9703412.

[21] Web page: http://acfahep.kek.jp/acfareport/node30.html#fig:smhbr

[22] M. Kobayashi and T. Maskawa, "CP - Violation in the Renormalizable Theory of Weak Intectation", Prog. Theor. Phys. 49, pp 652-657, Frebuary 1973.

[23] F. Abe et al., CDF Collaboration, "Evidence for Top Quark Production in $\bar{p}p$ Collisions at $\sqrt{s} = 1.8$ TeV", Phys. Rev. Lett. 73, 225 1994; hep-ex/9405005; Phys. Rev. D50 2966 1994.

[24] F. Abe et al., CDF Collaboration, "Observation of Top Quark Production in $\bar{p}p$ Collisions", Phys. Rev. Lett. 74, 2626 1995; hep-ex/9503002; S. Abachi et al., D0 Collaboration, "Observation of the Top Quark", Phys. Rev. Lett. 74, 2632 1995; hep-ex/9503003.

[25] C. T. Hill and E. H. Simmons, "Strong Dynamics and Electroweak Symmetry Breaking", hep-ph/0203079.

[26] I. Borjanovic et al., "Investigation of top mass measurements with the ATLAS detector at LHC", hep-ex/0403021.

[27] V. Kostyukhin, "Top quark reconstruction in ATLAS", Proceedings of Science, International Workshop on Top Quark Physics, Coimbra, Portugal, January 12-15, 2006.

[28] N. Kidonakis and R. Vogt, "Next-to-next-to-leading order soft-gluon corrections in top quark hadroproduction", hep-ph/0308222 v1, 2003.

[29] R. Bonciani, S. Catani, M.L. Mangano, and P. Nason, "NLL resummation of the heavy-quark hadroproduction cross-section", hep-ph/9801375, 1998.

[30] T. Stelzer, Z. Sullivan and S. Willenbrock, "Single-Top-Quark Production via W-Gluon Fusion at Next-to-Leading Order", Physical Revoew D56:5919-5927,1997.

[31] J. Campbell and F. Tramontano, "NLO corrections to Wt production and decay", hep-ph/0506289, 2005.

[32] M. Smith and S. Willenbrock, "QCD and Yukawa corrections to single topproduction via $q\bar{q} \to t\bar{b}$", Physical Review D, Volume 54, page 6696,1996.

[33] Particle Data Group, "Review of Particle Physics", European Physical Journal C3: 1-794, 1998.

[34] S. Eidelman et al., "Meson Summary Tables", Phys. Lett. B 592, 1 2004.

[35] ATLAS Collaboration, "ATLAS Detector and Physics Performance Technical Design Report", CERN/LHCC 99-14/15 1999.

[36] S. Keller and J. Womersley, "Measurement of the W boson mass at the LHC", Eur. Phys. J. C 5, 249-253 1998.

[37] C. Amsler et al., "Particle Data Group", Physics Letters B667 1 2008; http://pdg.lbl.gov.

[38] J. Cammin,"Precision measurement of the top quark mass in lepton+jets channels", Proceedings of Science, International Workshop on Top Quark Physics, Coimbra, Portugal, January 12-15, 2006.

[39] P. Lefebvre and T. Pettersson, "The Large Hadron Collider: Conceptual design", CERN-AC-95-05-LHC, (1995).

[40] ATLAS Collaboration, "ATLAS Technical Proposal for a General-Purpose pp experiment at the Large Hadron Collider at CERN", CERN/LHCC/94-43,LHCC/P2, 15 December 1994.

[41] CMS Collaboration,"CMS Technical Proposal", CERN/LHCC 94-43, 1994.

[42] LHCb Collaboration,"LHCb Technical Proposal", CERN/LHCC 98-4, 1998.

[43] ALICE Collaboration,"ALICE Technical Proposal", CERN/LHCC 95-71, 1995.

[44] "ATLAS Detector and Physics Performance Technical Design Report", Volumes I and II CERN/LHCC 99-14 and CERN/LHCC 99-15, May 1999.

[45] K. Adair, "The Great Design: Particles, Fields, and Creation", page 214. New York: Oxford University Press, 1989.

[46] The Particle Adventure, http://www.particleadventure.org

[47] ATLAS collaboration, "ATLAS Technical Proposal for a General-Purpose pp Experiment at the Large Hadron Collider at CERN", CERN/LHCC/94-43, LHCC/P2, 15 December 1994.

[48] G. Schlager, "The Energy Response of the ATLAS Calorimeter System", a Ph.D. thesis, CERN-THESIS-2006-056, December 2006.

[49] ATLAS Inner Detector Collaboration, "ATLAS Inner Detector Technical Design Report", CERN/LHCC/97-16 & 17, 1997.

[50] "Technical Design Report of the ATLAS Pixel Detector", CERN/LHCC/98- 13, 1998.

[51] "The ATLAS Semiconductor Tracking Endcap", A Ph.D. thesis, NIKHEF, 2003.

[52] "The ATLAS inner tracker and the detection of light Super-Symmetric Higgs bosons", A Ph.D. thesis, University of Twente, 2003.

[53] "ATLAS Inner Detector Technical Design Report", Volume II, April 30, 1997.

[54] "ATLAS Liquid Argon Calorimeter Technical Design Report", CERN/LHCC/96-41, December 1996.

[55] ATLAS Large Unit, "Liquid Argon Calorimeter Technical Design Report", CERN/LHCC/96-41, 1996.

[56] E. Aubert et al. (RD3 collaboration), "Performance of a Liquid Argon Electromagnetic Calorimeter with an Accordion Geometry", Nuclear Instrumentations and Methods in Physics Research A309:438, 1991.

[57] U. Amaldi, "Fluctuations in Calorimetry Measurements", Physica Scripta, 23, 409-423, 1981.

[58] ATLAS collaboration, "ATLAS Liquid Argon Calorimeter Technical Design Report", CERN/LHCC/96-41, ATLAS TDR 2, 1998.

[59] ATLAS Colaboration, "ATLAS Calorimeter Performance Technical Design Report", CERN/LHCC, January 1997.

[60] D. C. O'Neil, "Performance of the ALTAS Hadronic End-cap Calorimeter and the Physics of Electroweak Top Quark Production at ATLAS", A Ph.D. thesis, November 1999.

[61] R. Wigmans, "On the Energy Resolution of Uranium and other Hadron Calorimeters", Nuclear Instruments and Methods in Physics Research, A 259, 389-429, 1987.

[62] C. W. Fabjan, "Calorimetry in High Energy Physics", NATO Adv. Study Inst. Ser. B Phys. 128, 281, 1985.

[63] "ATLAS Muon Spectrometer Technical Design Report", CERN/LHCC/97-22,May 1997.

[64] "ATLAS Level-1 Trigger Technical Design Report", CERN/LHCC/98-14, June 1998.

[65] "ATLAS DAQ, EF, LVL2 and DCS Technical Progress Report", CERN/LHCC/98-16, June 1998.

[66] H. Herman, J. ten Kate, on behalf of the ATLAS Collaboration,"The ATLAS Superconducting Magnet System: Status of Construction & Installation", Volume 16, Issue 2, 499-503, IEEE, June 2006.

[67] The ATLAS Collaboration, "Magnet System Technical Design Report", CERN/LHCC/97-18, CERN, 1997.

[68] ATLAS Collaboration, "ATLAS Level-1 Trigger Technical Design Report", ATLAS TDR-12, 1998.

[69] ATLAS Collaboration, "DAQ, EF, LVLE2 and DCS Technical Progress Report", LHCC 98-16,1998.

[70] ATLAS Collaboration, "Computing Technical Design Report", TDR, CERN-LHCC-2005-022, 2005.

[71] http://root.cern.ch/

[72] http://atlas.web.cern.ch/Atlas/GROUPS/SOFTWARE/OO/architecture/General/Documentation/AthenaDeveloperGuide-8.0.0-draft.pdf.

[73] G. Barrand et al., "Gaudi - A Software Architecture and Framework for building HEP Data Processing Applications", International Conference on Computing in High Energy Physics (CHEP), 2000.

[74] http://lhcb.web.cern.ch/lhcb/

[75] S. Binet, "Light jet energy scale in situ calibration using a resonance decay in the $t\bar{t}$ channel with ATLAS", ATL-COM-SOFT-2005-001.

[76] A. I. Etienvre et al., "Top quark mass measurement with ATLAS (CSC-note T9/V0)", ATL-PHYS-PUB-2006-000, Feb 6 2008.

[77] The CDF Collaboration, "Combination of CDF Top Mass Results", CDF note 9214, Feb. 21 2008.

[78] http://atlas.kek.jp/sub/documents/hawaii200610 /Kaneda30Oct2006JetReco.ppt

[79] R. Field, "The Underlying Events in Hard Scattering Processes", Cambridge workshop (CDF), July 20 2002. http://www.phys.ufl.edu/ rfield/cdf/

[80] The ATLAS Collaboration, "Light jets in $t\bar{t}$ events (CSC-note T2)", ATL-PHYS-PUB-2006-000, May 15 2008.

[81] C. Biscarat, "In situ jet energy calibration methods in ATLAS", APS Meeting 2001.

[82] J. Lu and D. M. Gingrich, "Update of calorimeter calibration using E/p of hadrons from τ decay in Z $\rightarrow \tau\tau$ events using 12.0.6 CSC data", update of ATL-COM-PHYS-2006-023.

[83] R. Lefasvre and C. Santo, "In situ determination of the scale and resolution of the jet energy measurements using Z^0 + jet events", ATL-PHYS-2002-026.

[84] S. Binet, "Light jet energy scale in situ calibration using a resonance decay in the $t\bar{t}$ channel with ATLAS", ATL-COM-SOFT-2005-001.

[85] A. I. Etienvre, J. P. Meyer and J. Schwindling, "Top quark mass measurement in the lepton plus jet channel using full simulation", ATL-PHYS-INT-2005-002, ATL-COM-PHYS-2005-020.

[86] http://pdg.lbl.gov/.

[87] The ATLAS Collaboration,"Top Quark Properties", ATLAS CSC note, ATL-PHYS-PUB-2006-000, Dec. 20 2007.

[88] F. A. Berends et al., "Multijet production in W, Z events at $p\bar{p}$ colliders", Phys. Lett. B, Vol 224, p237, 1989.

[89] J. Pumplin et al., "New Generation of Parton Distributions with Uncertainties from Global QCD Analysis", hep-ph/0201195v3, 2002.

[90] G. Corcella et al., "HERWIG 6.5: an event generator for Hadron Emission Reactions With Interfering Gluons", hep-ph/0011363, 2002.

[91] J. M. Butterworth et al., "Multiparton Interactions in Photoproduction at HERA", hep-ph/9601371, 1996.

[92] M. L. Mangano et al., "ALPGEN, a generator for hard multiparton processes in hadronic collisions", hep-ph/0206293 v2, 2003.

[93] B. P. Kersevan and Elzbieta, R.W., "The Monte Carlo Event Generator AcerMC version 2.0 with interfaces to PYTHIA 6.2 and HERWIG 6.5", hep-ph/0405247, 2004.

[94] http://home.thep.lu.se/ torbjorn/Pythia.html

[95] http://jarguin.home.cern.ch/jarguin/dc3requests_sm.html

[96] C. Lange et al., "Triggering top quark events in ATLAS", ATL-PHYS-PUB-2008-xxx, ATLAS CSC note, April 22 2008.

[97] S. Catani, Yu.L. Dokshitzer, and B.R. Webber, "The $K_\perp$ clustering algorithm for jets in deep inelastic scattering and hadron collisions", Phys. Lett. B 285 291,1992.

[98] www.isv.uu.se/thep/courses/QCD

[99] S. Eidelman, et at.,"Review of Particle physics", Physics Letters B 592, 1 2004.

[100] I. Borjanovic, et al., "Investigation of top mass measurements with the ATLAS detector at LHC", hep-ex/0403021.

[101] http://seal.web.cern.ch/seal/MathLibs/Minuit2/html/

Appendix A

W decay in $t\bar{t}$ event

W bosons are massive vector bosons (80.398 $\pm$ 0.025 GeV/c^2) and have a short lifetime (3×10^{-25}s for the full decay width 2.141 $\pm$ 0.041 GeV/c^2). W bosons decay into two fermions, e.g. a W^- can decay into a lepton and anti-neutrino or a quark anti-quark pair. Possible decay modes of the W are shown in table A.1. The W cannot decay to the higher-mass top quark.

Table A.1: Possible decay modes of W into leptons and hadrons.

W	$\rightarrow$	$e\nu_e$
W	$\rightarrow$	$\mu\nu_\mu$
W	$\rightarrow$	$\tau\nu_\tau$
W	$\rightarrow$	ud
W	$\rightarrow$	$u\bar{s}$
W	$\rightarrow$	$u\bar{b}$
W	$\rightarrow$	cd
W	$\rightarrow$	$c\bar{s}$
W	$\rightarrow$	cb

From table A.1, the probability of both W's decaying leptonically is $\frac{3}{9}\times\frac{3}{9}$, the probability of both W's decaying hadronically is $\frac{6}{9}\times\frac{6}{9}$ and the probability of one W decaying leptonically and the other hadronically is $2\times\frac{3}{9}\times\frac{6}{9}$. For a single lepton decay the branching ratio is $\frac{1}{9}\sim 11\%$ whereas for a single hadron decay it is $\frac{6}{9}\sim 67\%$. These are close to the value in the PDG [37].